Operating Converter Interfaced Microgrids

by

Ramachandra Rao Kolluri

Thesis
submitted in partial fulfilment
of the requirements of the degree

Doctor of Philosophy

THE UNIVERSITY OF
MELBOURNE

Department of Electrical and Electronic Engineering

November 2016

Abstract

Microgrids have potential applications for both developing as well as developed countries. In developed countries, microgrid deployment can help in lowering carbon-dioxide emissions and increasing resiliency of the electricity network. In developing countries, microgrids can be used to improve rural electrification levels. The microgrid trend is going to disrupt the traditional energy generation paradigm of monolithic generation. This thesis addresses some challenges that arise with the evolution of microgrids.

Microgrids are small sections of the electrical network that comprise of local generation and load. Microgrids, by definition, must be able to operate in isolation from the main grid. In isolated operation, the co-ordination between sources is very important to achieve stability and ensure operational longevity. Two control hierarchies are popular in microgrid design: 1) master-slave control, and 2) master-less control. These controls are implemented on the sources' power electronic converters.

In master-slave control based microgrids, sizing and operating storage systems in combination with local generation is deemed beneficial for reasons like, facilitating pre-meter consumption and leveraging the time-of-use price arbitrage. In this thesis, a model of radial master slave microgrid network with distributed generation and storage is developed. The model developed can be readily adopted to DC master-slave microgrids as well as AC master-slave microgrids with high power factor. Using this model, a central optimization algorithm is proposed. This algorithm allows users to size, position and operate batteries in an intelligent manner where all the network constraints are satisfied and the network costs (capital + operational) are minimized. On solving the problem as a mixed integer linear program (MILP) we obtain appropriate battery sizing decisions at each house in the network and their intended temporal charging and discharging profiles. We extend our results using Monte-Carlo simulation based analysis to address forecasting errors in generation and demand.

On the other hand, the design and operation of master-less converter-based microgrids depend on various factors. Little explored is the effect of component mismatches and parameters drifts on the stability and power sharing properties of these systems. On this subject, this works also aims to comprehend the stability and steady state behaviour of multi-master converter based microgrid systems under the presence of non-identical components and parameter drifts. It is shown that microgrid wellness is very sensitive to such changes. We propose a set of co-ordination controls based on sparse (inter-node) communications to improve the stability margin and ensuring desired power sharing properties. Stability conditions are developed using Lyapunov's indirect method. The performance of the proposed microgrid design is verified using simulation results.

For master-slave microgrids, the proposed optimization algorithm improves the economics of microgrid storage while ensuring better power quality. For master-less microgrids, robustness of power sharing is made independent of parameter drifts, load and sources changes using the proposed methods. Scalability and source modularity are also well-preserved for the master-less scenario using the distributed control laws introduced.

Declaration

This is to certify that

1. the thesis comprises only my original work towards the PhD,
2. due acknowledgement has been made in the text to all other material used,
3. the thesis is less than 100,000 words in length, exclusive of tables, maps, bibliographies and appendices.

Ramachandra Rao Kolluri

7 November, 2016

Preface

Research Outputs

Following are the research outputs during the tenure of this course:

Journal articles:

1. I. Mareels, J. de Hoog, D. Thomas, M. Brazil, T. Alpcan, D. Jayasuriya, V. Muenzel, L. Xia and R. R. Kolluri, "On Making Energy Demand and Network Constraints Compatible in the Last Mile of the Power Grid", *Annual Reviews in Control*, Volume 38, Issue 2, 2014, Pages 243-258.;

2. R. R. Kolluri, I. Mareels, T. Alpcan, M. Brazil, J. de Hoog and D. Thomas, "Stability and Power Sharing in in Droop Controlled Microgrids: Effect of Clock Mismatches," *Automatica*, Under review.

3. R. R. Kolluri, I. Mareels, T. Alpcan, M. Brazil, J. de Hoog and D. Thomas, "Power Sharing in Angle Droop Controlled Microgrids," *IEEE Transactions on Power Systems*, Accepted.

4. R. R. Kolluri, I. Mareels, T. Alpcan, M. Brazil, J. de Hoog and D. Thomas, "Power Sharing in Frequency Droop Controlled Microgrids Experiencing Clock Drifts," *IEEE Transactions on Power Systems*, Submitted.

5. L. Xia, R. R. Kolluri, J. de Hoog, T. Alpcan, M. Brazil, D. Thomas and I. Mareels, "Voltage-Demand Relationship Modelling in Distribution Networks for Demand Management and PV Curtailment", *IEEE Transactions on Smart Grid*, Submitted.

Conference articles:

1. R. R. Kolluri, T. Alpcan, I. Mareels, M. Brazil, J. de Hoog and D. Thomas, "On the effect of component mismatches in inverter interfaced microgrids," *Power Engineering Conference (AUPEC), 2014 Australasian Universities,* Perth, WA, 2014, pp. 1-6.

2. R. R. Kolluri, I. Mareels, T. Alpcan, M. Brazil, J. de Hoog and D. Thomas, "Power sharing correction in angle droop controlled inverter interfaced microgrids," *2015 IEEE Power & Energy Society General Meeting*, Denver, CO, 2015, pp. 1-5.

3. R. R. Kolluri, L. Xia, J. de Hoog and I. Mareels, "Operating inverter interfaced microgrids - robustness issues," *The Third International Education Forum on Environment and Energy Science 2014* December 2014.

4. R. R. Kolluri, J. de Hoog, K. Abdulla, I. Mareels, T. Alpcan, M. Brazil and D. Thomas, "Siting and Sizing Distributed Storage for Microgrid Applications," *2017 IEEE Conference on Smart Grid Communications*, Dresden, Germany, Accepted.

Other reports:

1. K. Abdulla and R. R. Kolluri, "Multi-verter - Multi-purpose Multi-level Power Converter" *Technical Report*, December 2015.

2. L. Xia, R. R. Kolluri, I. Mareels, T. Alpcan and I. C. Jennings, "Power Quality Management and Optimization for Business Customers with Private Local Networks" *Technical Report*, September 2015.

Individual contributions

1. Ramachandra Rao Kolluri is the main contributor of journal articles #2, #3 and #4 and conference articles #1, #2, #3 and #4 that are elaborated as original work in Chapters 4, 5 and 6 of this thesis. This work has been carried out under the principal supervision of Prof. Iven Mareels and co-supervision of Prof. Doreen Thomas, A. Prof Marcus Brazil, A. Prof. Tansu Alpcan and Dr. Julian de Hoog

all of whom have been instrumental in developing the ideas and have been listed as co-authors to the articles in order of their contribution.

2. Some interesting discussions have taken place between Ramachandra Rao Kolluri and Khalid Abdulla on battery sizing and optimization which led to Khalid Abdulla being added as a co-author on conference article #4. The authors on conference article #4 also have been listed in the order of their contribution.

Financial support

This work has been partly funded by a Linkage Grant supported by the Australian Research Council, Better Place Australia and Senergy Australia.

Acknowledgements

To begin with, I would like to thank God for giving me this opportunity. I have been very fortunate.

I would like to thank my supervisors, Prof. Iven Mareels, Prof. Doreen Thomas, A. Prof. Tansu Alpcan, A. Prof. Marcus Brazil and Dr. Julian de Hoog for their continued support, patience and encouragement throughout the degree. Their knowledge and insights are crucial in building up the ideas that formed this thesis. I shall be ever grateful to them for their faith in me and always look up to them as my guides in research and beyond.

I would like to thank my advisory committee chair, Prof. Mohammad Aldeen for his suggestions and encouraging comments on this work. I would like to thank my postgraduate colleagues for their friendship. Especially, Valentin Muenzel, Lu Xia and Khalid Abdulla.

I would like to thank Prof. Graham Holmes, Prof. Brendan Mcgrath and Dr. Carlos Texiera for their support and guidance in the experimental studies. I would like to extend my thanks to all the reviewers who helped refine the ideas in this thesis.

I would like to thank my mother Adi Lakshmi Kolluri and my sister, Sri Lakshmi Kolluri for making me what I am today. You were, are and forever remain my inspiration.

I would like to thank Varsha Shrivastav who has been with me throughout my journey. Her love and support has no bounds.

Finally, I would like to thank my father, Babji Manohar Kolluri. Dad, you have always been my strength. I miss you !!!

To Dad and Mom, my infinite motivation;

Contents

List of Figures

List of Tables

Nomenclature

1PPS	1 Pulse Per Second
AC	Alternating Current
CO_2	Carbon Dioxide
DAPI	Distributed Averaging Proportional Integral
DC	Direct Current
DDE	Delayed Differential Equation
DG	Distributed Generation
DRIS	Distributed Resource Island Systems
HV	High Voltage
LP	Linear Program
MILP	Mixed Integer Linear Program
MV	Medium Voltage
MW	Megawatt
NaS	Sodium Sulphur
NEMA	National Electrical Manufacturers Association

NiCd Nickel Cadmium

PCC Point of Common Coupling

PI Proportional Integral

PLL Phase Locked Loop

PR Proportional Resonant

PV Photovoltaic

PWM Pulse Width Modulation

SMES Superconducting Magnetic Energy Storage

SoC State of Charge

THD Total Harmonic Distortion

Part I

INTRODUCTION

1

Introduction

1.1 Background

THE electricity industry is undergoing a revolution due to technological advancements, changes in demand patterns, and the more widespread introduction of intermittent renewable generation sources. As a result, there is an increased need for solutions that are flexible with regard to variable supply and demand and can adapt to dynamically changing requirements in ways that lead to optimal economic and operational outcomes.

In recent years, integration of distribution level renewable energy generation with or without storage is becoming an increasingly common phenomenon. With rising atmospheric carbon dioxide (CO_2) levels and a push to promote *carbon neutral* or *green* technologies, a major transition into renewable energy based generation seems imminent [58, 114]. Strong reductions in the costs of renewable technologies (putting them at grid parity in many parts of the world) are also promoting renewable energy intake. While many large-scale renewable generation plants exist, often renewables are introduced in small-scale and distributed ways (and indeed wind and solar are both well suited to this) making them more distributed/scattered throughout the grid. Small isolated electricity networks based on distributed generation, known as microgrids, appear

as a natural extension to this decentralization [24, 81]. Although microgrids are envisioned as exciting opportunities, providing services identical to the traditional electrical power system, often referred to as the grid, is much more complicated.

Traditional or *inertial* generation is very well understood and its availability is deemed very important to maintain the voltage and frequency levels within acceptable limits while producing the required amount of energy. The inherent dynamics of inertial generation within the grid govern power sharing and synchrony between various sources. However, the generation mixture in the microgrid scenario is quite different. Most of the renewable energy sources need a power electronic interface to merge into and utilize the existing power system infrastructure. Improved understanding of power electronics, over the years, has made the control and grid integration of these distributed sources familiar.

Nonetheless, our understanding of interconnected operation of these distributed power electronic converter interfaced systems in microgrids scenarios is not very mature and relies on fairly recent technological developments. Given that microgrids tend to have a major portion of their generation from power electronic interfaced sources, or simply *converter* based sources, it is very important to understand the interactions between such systems. Therefore, the main objective in microgrid design is to maintain reliability, robustness and stability that is comparable with the traditional grid model. Sometimes, as in scenarios involving critical loads, the reliability requirements of microgrids are far higher than traditional grid models making proper microgrid design and analysis exceptionally important.

The majority of the methods envisaged to operate and achieve synchrony between connected converter-based sources build either on generator emulation or simple feedback methods. A few challenges such as, sizing energy storage, ensuring power sharing and stability, etc., still exist in this domain and they limit opportunities the power electronic converters might provide. In this light, this thesis addresses operating converter

interfaced microgrids from both theoretical and practical perspectives.

1.2 Objectives

The primary research objectives of this thesis are:

- To establish an accurate understanding of how to model generation in various microgrid scenarios.
- To demonstrate a control design shown to be effective in sizing and operating storage devices for a master-slave microgrid topology.
- To identify the effects of component mismatches and parameter drifts on stability and power sharing in droop controlled converter interfaced microgrids.
- To propose control designs that can achieve better power sharing and improve overall stability of droop controlled microgrids under component mismatches.

1.3 Specific research questions

In view of the above objectives, we formulate specific research questions as follows:

Part 1: Addressing energy deficits using storage

- *What is a method to model a microgrid network that is based on a master-slave topology?*
- *What is a way to size the batteries at individual households within a master-slave microgrid and operate them to satisfy realistic physical/ financial constraints?*
- *How to address uncertainty? In other words, how to improve the performance of the proposed method under uncertain load and generation forecasts?*

Part 2: Controlling parallel converter based generation under mismatches

- *How does clock accuracy/drifts affect the stability and power sharing of both angle and frequency droop controlled systems?*
- *What is a way to alleviate the effects of clock drifts on power sharing and stability for any arbitrary topology in a droop controlled microgrid?*
- *What assumptions should be made in solving this problem of clock drift effect and are these realistic?*
- *What are the conditions for achieving stability and power sharing for the methods introduced?*
- *How crucial is the output impedance design in angle droop controlled converter interfaced microgrids and what effect does impedance mismatch have on power sharing?*
- *How can control design overcome the negative effect impedance mismatch has on power sharing?*

A detailed introduction to the concept of microgrids, master-less and master-slave topologies, energy storage sizing and operation, impact of component mismatches in parallel converter based microgrids will be provided in the later chapters which will bring the research questions posed above well into context.

1.4 Thesis Outline

This thesis is structured as follows:

Chapter 1 This chapter introduces the topics covered in this research thesis and provides a brief background together with a chapter-wise summary of this report.

Part I: DISTRIBUTED GENERATION

Chapter 2 This chapter provides an in-depth background of distributed generation based on power electronic converters. It provides a critical summary of various traditional control techniques that are fundamentally used in power electronic converter based generation. Some market research and economic motivations for microgrids are also presented in this chapter.

Chapter 3 This chapter provides in-depth analysis and a review of state-of-the-art technologies in microgrids along with some illustrative examples. We present a section here that includes the research questions being addressed in this thesis and pertinent literature.

Part II: ENERGY STORAGE SYSTEM DESIGN

Chapter 4 In this chapter we provide a framework that can be used in sizing, positioning and operating batteries in a grid-connected distribution network or a master-slave microgrid. We use mixed integer linear programming (MILP) based optimization approach considering various operational/capital costs and constraints to guarantee better network quality and make financial benefits simultaneously. The performance of our approach is validated using simulations. We also present some extended results based on Monte-Carlo type simulations and receding horizon control.

Part III: CONTROLLING PARALLEL CONVERTER BASED GENERATION

Chapter 5 This chapter discusses the modelling of clock drifts in converter based systems. The power sharing mismatch and instability that occur as a consequence of the clock drifts in frequency droop controlled microgrids are identified. Based on

this, we introduce a sparse communication-based control technique that alleviates power sharing errors. We analyze the stability of the microgrid operating with the proposed technique. Simulation results are presented to validate the performance of the proposed methods.

Chapter 6 This chapter discusses the impact of impedance distribution and clock drifts on angle droop controlled microgrids systems. These mismatches cause huge power variations that can be destabilize the microgrid if left uncontrolled. We then propose a two-part control technique that uses sparse communication to rectify the power sharing errors and subsequently analyze the stability of the modified microgrid. Simulation results are presented to validate the performance of the proposal.

PART IV: CONCLUSION

Chapter 7 The thesis is concluded in this chapter. Some directions for future research that are aligned with the topics covered in this thesis are presented.

1.5 Contributions

The research contributions made in this thesis can be encapsulated into two distinct parts.

Part 1: Addressing energy deficits using storage

1. A linear radial master-slave microgrid model is developed in Chapter 4 using principles and devices described in Chapters 1, 2 and 3. This model encapsulates the network characteristics, local generation and demand characteristics using simple Kirchoff's laws. The model is then used in developing an optimization framework that sizes, positions and operates batteries in a distributed manner within the mi-

crogrid. Various physical and financial constraints are used in in the constraint set for the optimization algorithm. We solve the problem as an MILP to accommodate integer battery sizes. The results show improvement in the network quality as well as the economics of operating the microgrid. Monte-Carlo simulation analysis is used in extending the results of the optimization algorithm to address uncertainty in forecasts.

Part 2: Controlling parallel converter based generation under clock drifts and mismatches

1. In Chapter 5 we identify the ill-effects of clock/ frequency mismatches on the power sharing and stability of frequency droop controlled converter-based microgrids. To counteract these ill-effects, especially in terms of power sharing, we introduce a modified frequency droop controller. This controller is based on sparse inter-node communications, where all the converters influence their neighbours to achieve a global consensus in power sharing without compromising frequency synchronization. We impose some conditions on the integral control variable (within modified frequency droop) to establish microgrid stability. These conditions are developed using an eigenvalue analysis of a linearized state space model of the microgrid containing constant impedance loads. Simulation results are presented to illustrate the performance of the proposal.

2. In addition, we identify the effect of disproportionate impedance distribution between angle droop controlled converters in a microgrid in Chapter 6. We also identify that frequency/ clock mismatches can impact the stability and power sharing accuracy of angle droop controlled converter-based microgrids. We propose modified angle droop as a method to cope with these problems. The proposed controller is based on sparse inter-node communications and comprises two control stages: one to establish frequency consensus and one to counteract the power sharing deviations. Conditions that ensure frequency consensus and power sharing accuracy are developed. It is shown that for a given network, its physical characteristics and

the overlaying communication network connectivity are crucial in developing stability conditions. The performance of the proposal is illustrated using simulation results.

✧✧✧

Part II

DISTRIBUTED GENERATION AND MICROGRIDS

2

Background

Notation

The variable t represents time. Derivative of a function $u(t)$ with respect to time is represented by $\dot{u} = \frac{du(t)}{dt}$. For any sinusoidal signal, $e(t) = e_0 \sin(ft + g)$, e_0 represents the amplitude, f represents the frequency and g represents the phase angle. The phasor representation of the above sinusoidal signal, $e(t)$ is $e_0 \angle g$. The phasor notation is valid if and only if the frequency, f is a global constant. Let $\underline{y} = a + jb$ be a complex number with $j = \sqrt{-1}$; its real part is given by $\Re\{\underline{y}\} = a$ and the imaginary part is given by $\Im\{\underline{y}\} = b$. The complex number $\underline{y}^*$ denotes the complex conjugate of the complex number $\underline{y}$, *i.e.,* $\underline{y}^* = a - jb$. We define the n-dimensional column vector $x = col(x_i) = [x_1, x_2, \ \ldots, x_n]^T$ where $(.)^T$ represents a transpose function. Let $diag(x_i)$ be a $(n \times n)$-dimensional diagonal matrix with x_i in the ith row and ith column and 0 elsewhere. The $(n \times n)$-dimensional identity matrix is given by $\mathbf{I}_n = diag(1)$. The matrix $1_{n \times n}$ is a $(n \times n)$-dimensional matrix with all elements equal to 1. The communication network is represented as a graph $\mathbf{G}_c = (\mathbf{V}_c, \mathbf{E}_c)$. $\mathbf{V}_c$ is the set of nodes and $\mathbf{E}_c$ is the set of edges which represent the communication links between nodes. We define the communication degree matrix $\mathbf{D}_c \triangleq diag(\deg(i))$, where $\deg(i)$ is the number

of communication links connected to the ith node and n is the number of active nodes in the system. Adjacency matrix $\mathbf{A}_c$ represents the connection between nodes in the communication graph with $a_{ij} = a_{ji} = 1$ if the nodes i and j are connected, and $a_{ij} = a_{ji} = 0$ otherwise. Self loops are avoided, resulting in $a_{ii} = 0$ for any node i. We denote the communication graph Laplacian $\mathbf{L}_c = \mathbf{D}_c - \mathbf{A}_c$. The vector 1_n is basis of the kernel of $\mathbf{L}_c$ i.e., for any vector $v = \theta 1_n, \theta \in \mathbb{R} \setminus \{0\}$ we have $\mathbf{L}_c v = 0_n$ and since the matrix is symmetric we also have $v^T \mathbf{L}_c = 0_n^T$. Its eigenvalues $\{\lambda_{c,1}, \lambda_{c,2}, \ldots \lambda_{c,n}\}$ obey the relationship $0 = \lambda_{c,1} < \lambda_{c,2} \leq \ldots \lambda_{c,n}$.

2.1 Introduction

POWER flow in the traditional electricity grid is radial, i.e., power is produced at central generation stations and flows to the customers through various transmission and distribution stages as shown in Figure 2.1. The hierarchy followed by this traditional grid is typically vulnerable and has some significant disadvantages. At the generator level, the energy conversion efficiency of these large central generators can be as low as one third, without considering waste heat recovery and the subsequent CO_2 emissions [160]. The transmission and distribution line losses accumulate to 8% of the energy produced on an average [1]. These losses alone account for about 1.2 trillion metric tonnes of annual CO_2 emissions [61].

Other important factors in evaluating the traditional grid are energy sufficiency, proper utilization and economic impact. In many networks, as much as 20% of the generation (and transmission) capacity exists only to supply peak demand, which may only occur once or twice a year. This forces the generators to run at a reduced efficiency during off-peak periods leading to significant under-utilization. In recent years, the economics of the radial grid are not very attractive either. The expenses for the supply capacity and losses have to be borne by the consumers.

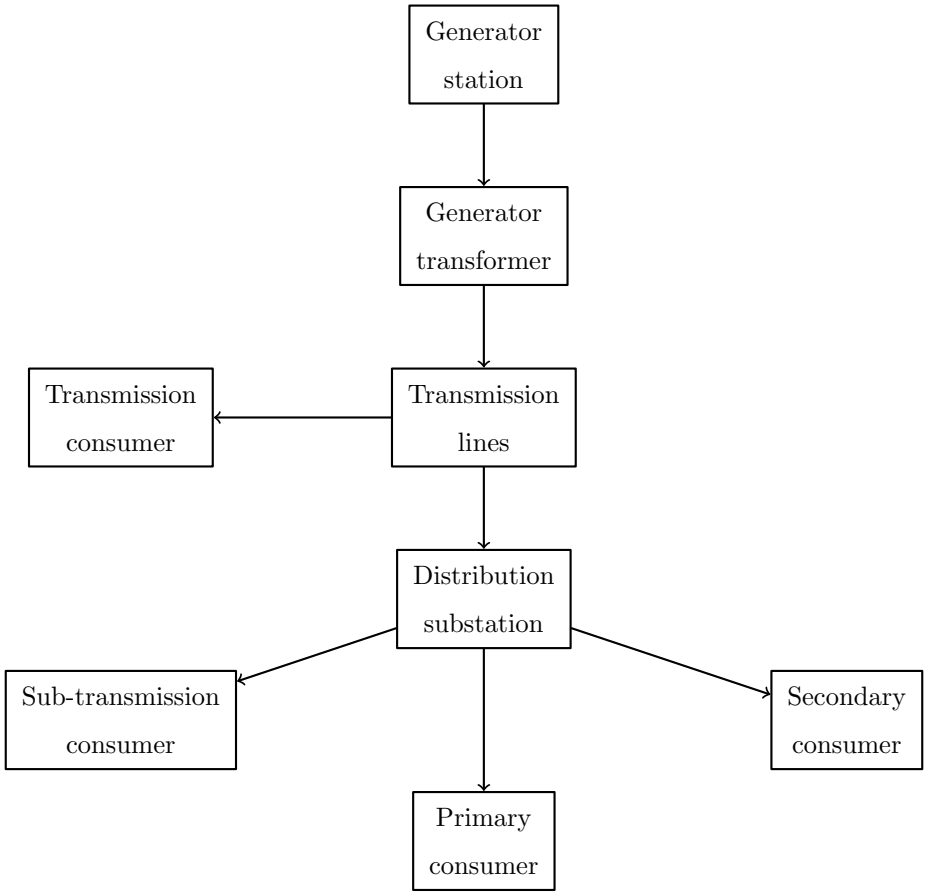

Figure 2.1: Traditional grid paradigm.

2.2 Distributed generation

Distributed generation (DG) is an approach that employs small-scale technologies to produce electricity close to the end users of power [152]. Recent years have seen distributed generation, particularly at the residential or commercial level, becoming more and more widely installed in many countries. Distributed generators, such as roof-top photovoltaic (PV) system, are currently very attractive in countries like Germany and Australia where abundant sunshine is matched with government incentives to encourage consumer participation. The market structure is envisaged to see major changes to accommodate these new technologies [14]. While sustainability and independence from

fossil fuels are the major advantages of distributed generation, others may include:

- Reduced capital cost per capacity - given the generation is local.
- Reduced carbon emissions when the local generation is based on non-conventional energy sources like solar energy.
- Reduced electricity bills by avoiding major line losses, behind-the-meter consumption and grid feed-in.
- Increased resilience to grid disturbances (in off-grid operation) and electricity price fluctuations.

Most of the advantages scale inversely proportional to the availability of efficient and widespread network infrastructure. However, this is hard to achieve in most countries, for example see [66]. For all of these reasons, there is increased interest and economic motivation for the use of distributed energy generation, and the use of microgrids.

However, most distributed generation is not independent of the utility grid. Grid-connected operation of distributed generation is very common and well understood. The grid supervises the power quality and harmonizes the interaction between the distributed generators to avoid any ill-effects the latter may introduce. For example, uncontrolled distributed generation may increase voltage levels up a distribution line. The substation transformer will then become a control point where the moderator can change the transformer tap set-point to cope with the voltage rise. It is also the responsibility of the grid to maintain the frequency of a distribution line within acceptable limits. Overall, the grid has a unifying influence to maintain the health and safety of the network. Therefore, we can conclude that any grid-connected distributed generation system only reduces the need for energy from the grid but does not alleviate the need for transmission, distribution and other power quality services.

2.3 Introduction to microgrids

A set of standards known as, *IEEE 1547 Series of Standards for Interconnecting Distributed Resources with Electrical Power Systems* were introduced in 2004 to govern the design and integration of distributed sources into the grid [17]. However, in 2011 a modification to [17] was made to facilitate the design and operation of interconnected standalone distributed sources [140]. This modification introduced a global definition for distributed resource island systems (DRIS), often referred to as *microgrids.* According to [140], the term microgrids is used for sections of electrical power systems that:

- have at least one distributed generation resource and a load,
- have the ability to disconnect from and parallel with the area electrical power system, i.e., *main grid*,
- include the local electrical power system and may include portions of the area electrical power system, and
- are intentionally planned.

Over the last few years, there has been an observable increase in the number of critical loads [24]. Supplying critical loads, such as military facilities, hospitals and so on, without interruption was one of the primary original motivations for the introduction of microgrids. In addition, new business models are emerging in many countries where cheap distributed generation (often with storage) can replace the need for transmission line upgrade or installation, leading to the formation of further microgrids. The operating modes for microgrids are recognized and defined [140, Clause 4] as follows:

1. Grid-connected mode,
2. Transition to island mode,
3. Island mode, and
4. Reconnection mode.

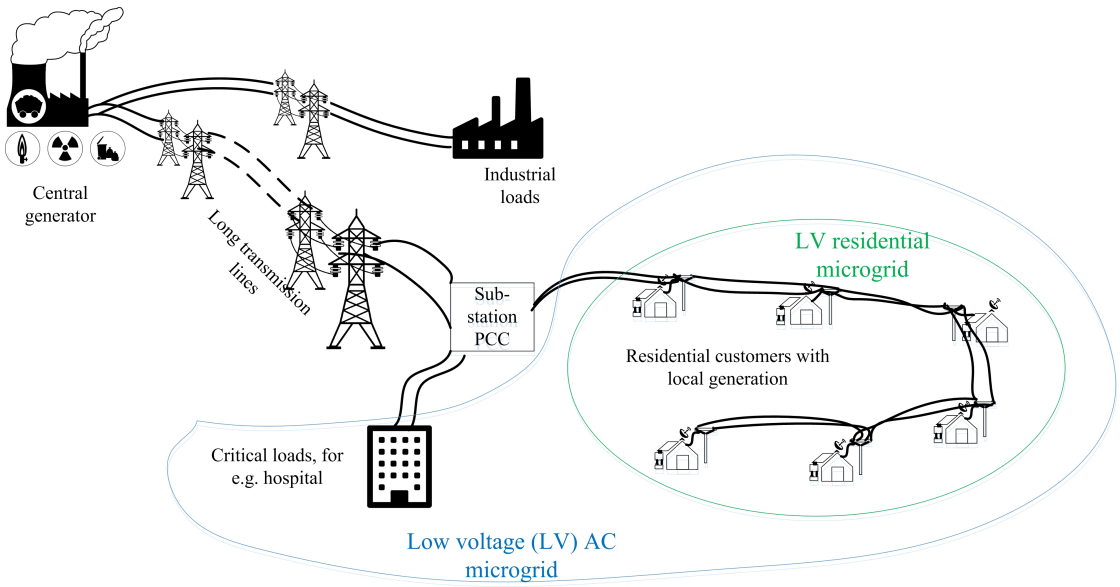

Figure 2.2: A typical microgrid example.

With renewable energy sources being naturally replenished, successfully operating *microgrids* in isolation will increase the areas' security of supply to critical loads (from disturbances in the grid), reduce the losses that are incurred from energy transmission (if it were from a central generator far away from the area) and provide several other opportunities. A graphical representation of a low voltage microgrid is given in Figure 2.2. Observe that the point of common coupling (PCC) is generally located at the distribution substation and controls the microgrid disconnection/reconnection. Although Figure 2.2 is one possible configuration, the PCC can be located anywhere in the network. A single line diagram showing possible islanding combinations is extracted from [140] and shown in Figure 2.3.

2.3.1 Economic significance of microgrids

It is predicted that close to 80% of countries will have solar generation reach grid parity (in terms of retail cost of generation) by the year 2017 [127]. With such improvements in renewable energy prices it is evident that there is significant potential for rapid growth in the microgrid market, which in turn will impact global electricity markets. Accord-

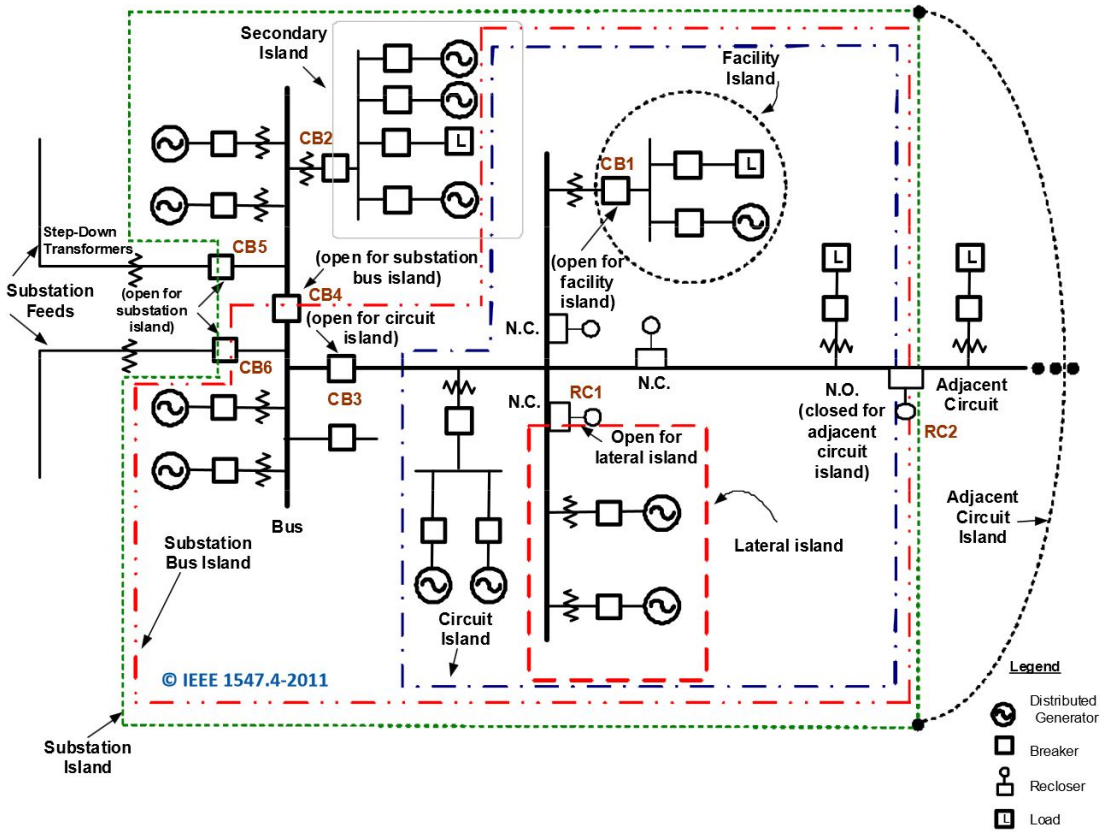

Figure 2.3: Few possible island configurations for microgrids [140].

ing to research conducted by Asmus et al. in 2013 the revenue of the global microgrid market is $8.3 billion and is expected to increase to at least $40 billion by the year 2020 [9][1]. As shown in Figure 2.4, about 1500 megawatt (MW) of microgrid capacity was deployed globally in 2011 and this is projected to increase to about 4500 MW by 2017 [11]. The projections in [11] are accurate up to 2013 according to the microgrid deployment status reports [9, 10]. Some microgrids currently deployed/under research can be found in [25, 44, 60, 76, 102]. With growing security requirements and renewable energy promotions, microgrids are ready to hit the mainstream power generation and distribution market very soon. Although most current deployments are not predominantly power electronic converter-based sources, with such immense interest in

[1]Based on average penetration and various other relevant assumptions.

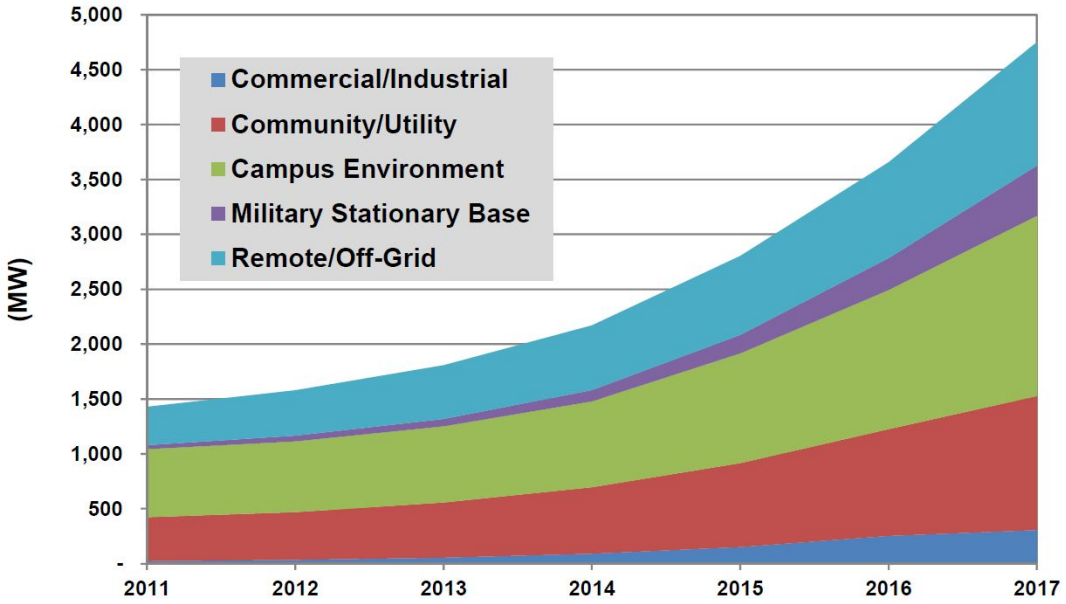

Figure 2.4: Forecast on global microgrid capacity (segmented by sector) between 2011 - 2017 based on an average penetration [11].

renewable energy based microgrid, fully converter-based renewable energy microgrids seem very likely.

2.4 Source disparity

Microgrids with local generation have always formed part of the electrical power system. Until recent years, however, the generation was usually via synchronous generators (rotating machines) operated on readily available fossil fuel. One advantage of these synchronous generators is that they operate on kinetic energy from the combustion of a transportable fuel and therefore can be operated for extended times. Renewable energy, on the other hand, is mostly a converted form of energy. Most renewable energy sources like solar photovoltaic systems, generally have a direct current (DC) supply characteristic and connect to an alternating current (AC) or DC load through a power electronic interface known as a converter. Unlike synchronous generators, the operation of these

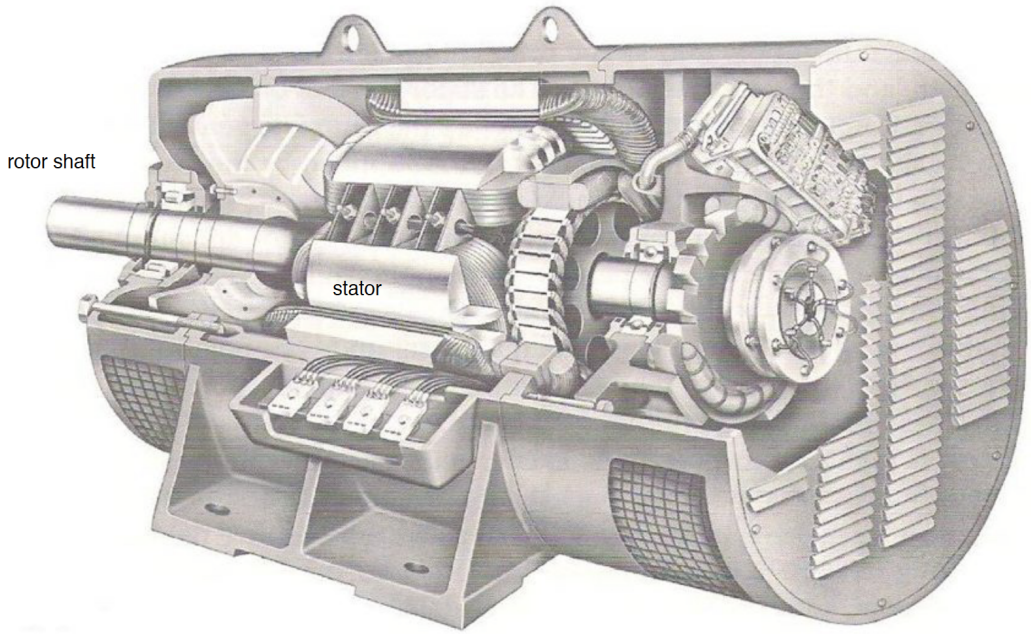

Figure 2.5: Cutaway view of a synchronous AC generator (used with permission from [53]).

converter-based renewable energy sources is limited by the amount of energy on the DC side. These energy bounds, however, can be extended by installing a battery storage system.

2.4.1 Inertial generation

This section gives a brief introduction to energy generation based on rotating machines. The prime mover, for example a steam turbine, is attached to the coil-wound rotating shaft of generator known as a *rotor*. The coil-wound stationary part of the generator, or simply *stator*, is mounted over the rotor. The conductive coil windings on the rotor are called *rotor windings* or *field windings* and those corresponding to the stator are known as *stator windings* or *armature windings*. Figure 2.5 shows a cutaway illustration of a typical synchronous generator with a rotor shaft and a stator [107]. There is a current

flowing in the rotor winding which is supplied by the rotor exciter. The rotation from the prime mover produces a change of flux in the stator windings which in-turn produces an electromotive force, termed as voltage. This voltage gives rise to the flow of electrical current through a closed electrical path, thereby harnessing electrical energy. Electromagnetic induction is the basis for this type of generation. Most inertial generation sources use this or a similar structure to generate electrical energy from mechanical energy. We refer to [73] for more information.

2.4.2 Non-inertial generation

Generation sources based on power conversion, on the other hand, do not involve rotating parts. These devices are a combination of semiconductor switches that are controlled to provide alternate current flow paths. Traditionally power converters are classified based on their input and output characteristics. Thus, we have:

- DC / AC converter, commonly known as an *inverter*, interfaces a DC system to an AC system - average power flow will, therefore, be from the DC to the AC side.
- AC / DC converter, commonly known as a *rectifier*, interfaces an AC system to a DC system - average power flow will, therefore, be from the AC to the DC side.
- DC / DC converter
  - Buck converter - The output DC voltage is lower than the input DC voltage
  - Boost converter - The output DC voltage is higher than the input DC voltage
  - Buck/Boost converter - The output DC voltage is either higher or lower than the input DC voltage based on the application.
- AC / AC converter - the voltage and frequency of the output is varied according to the application - for e.g. variable frequency drives, cycloconverters etc.

Structurally, the DC / AC and AC / DC converter systems are equivalent, therefore they can be used to achieve bidirectional power transfer depending on their set-up

and switching/control mechanism. Transfer of energy in a converter system is achieved through proper circuit design and appropriate switching of the semiconductor switches within. Further details regarding the characteristics and operation of various semiconductor switches can be found in [96]. Another classification in DC / AC converter systems is based on the current and voltage waveforms at their DC port. Current sourced converters are those in which the DC side currents retain their polarity after conversion, while in voltage sourced converters the DC side voltage retains the polarity. Average power flow in current sourced and voltage sourced converters is, therefore, determined by the polarity of their DC side voltages and currents, respectively.

2.5 Modelling distributed generation

2.5.1 Synchronous generators

A synchronous generator can be modelled as a voltage source behind an impedance, Z. This impedance is defined as,

$$Z = R + jX,$$

where $j = \sqrt{-1}$ is the imaginary unit, and R and X are the resistance and reactance, respectively. The magnitude of the output voltage of a synchronous generator depends on the magnitude of its output impedance and its rotor excitation current. This behaviour is attributed to, what is generally known as, the *electrical part*. The electrical part of the synchronous generator can be demonstrated with a simple per phase equivalent circuit as shown in Figure 2.6. Here the internal rotor circuit resistance and the external variable resistance of the rotor excitation circuit are combined together to form R_r, and L_r is the inductance of the field coil. The subscripts $(\cdot)_r$ and $(\cdot)_s$ represent rotor-side and the stator-side, respectively.

The per phase output voltage of the synchronous generator, v_o, is given by:

$$v_o = e_s - i_s R_s - L_s \frac{di_s}{dt},$$

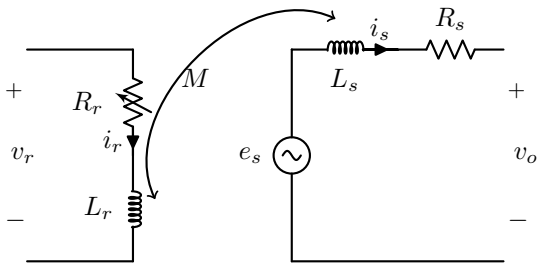

Figure 2.6: Per phase equivalent circuit diagram of a synchronous generator with the rotor circuit on the left and the stator circuit on the right.

and the internal / no load voltage e_s is given by:

$$e_s = \frac{d}{dt}(Mi_r \cos\theta_{gen}) = Mi_r\dot{\theta_{gen}} \sin\theta_{gen} - M\dot{i_r} \cos\theta_{gen},$$

where M is the mutual inductance between the coils as shown in the Figure 2.6 and θ_{gen} is the angle between the stator and the rotor windings. Therefore, for constant load and winding parameters, the output voltage, v_o is directly proportional to the rotor excitation current, i_r. See [164] for equivalent discussion on three-phase synchronous machines.

Furthermore, the rotating speed of the rotor is responsible for the frequency of the generator; and this is called the *mechanical part*. These frequency dynamics can be represented by the *swing equation* [154]:

$$J\ddot{\theta}_{gen} = T_m - T_e - D_p\dot{\theta}_{gen},$$

where θ_{gen} is the angular position of the rotor in radians, J is the moment of inertia of the rotor and its parts, T_e is the electromagnetic torque, T_m is the mechanical torque and D_p is the damping factor. The mismatch between mechanical torque and electrical torque is reflected in the generator frequency and the angular position as a consequence. Here the angular position, θ_{gen} is given by:

$$\theta_{gen} = \omega t + \delta_{gen},$$

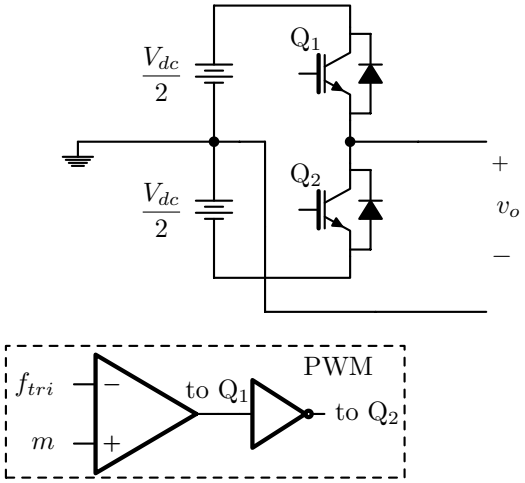

Figure 2.7: A half-bridge inverter with sine-triangle PWM switching control.

where ω is the system frequency. Therefore, if $\omega_r = \dfrac{d\theta}{dt}$ is the angular speed of the rotor in the synchronous generator, then $\delta = \int(\omega_r - \omega)dt$ is the angle between the rotor and the system, often called the load-angle. We refer to [41] for a detailed description on synchronous generator fundamentals. Observe that the moment of inertia, J is involved in the dynamics and has an impact on this system, therefore generation of this kind is known as *inertial generation*.

2.5.2 Converter technology

Distributed generation sources based on power electronics converters is the basis of the majority of this thesis. This section covers the fundamentals of such generation systems. The fundamental building block of *non-inertial* or converter-based generation is the half-bridge converter.

2.5.2.1 Half-bridge inverter

A half-bridge DC / AC inverter is given in Figure 2.7. This fundamental circuit, qualitatively, forms the basis of any inverter circuit. The semiconductor switches Q1 and Q2 are switched using gating signals from the pulse width modulation (PWM) block,

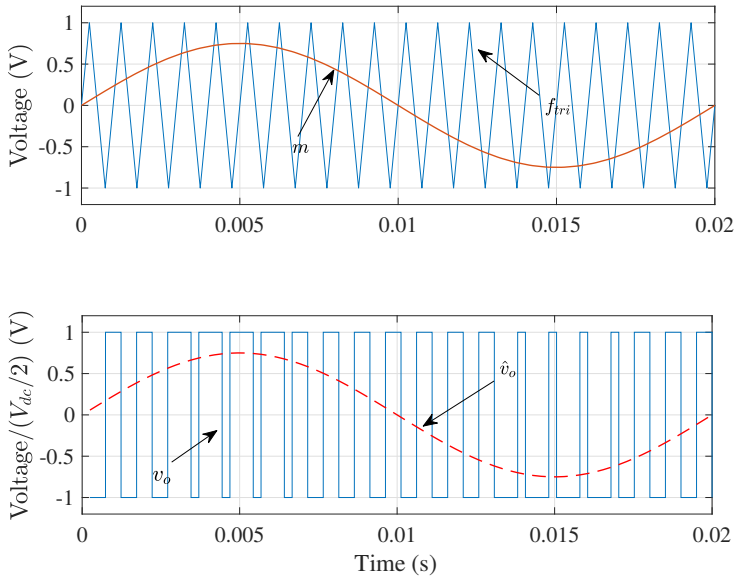

Figure 2.8: Pulse width modulation and the corresponding half-bridge voltage output.

thereby providing alternate paths to currents from the DC side (From V_{dc}) to the AC side (v_o).

Pulse width modulation (PWM) is a type of modulation scheme where a high frequency triangular waveform (also known as the *carrier signal*) is compared to a low frequency modulating waveform (also known as the *control signal*) to generate pulses of varying duty-cycle. This is illustrated in Figure 2.8. The modulating waveform, m, for the DC / AC inversion is generally a (scaled) sinusoid. The amplitude of the carrier signal, f_{tri}, and the control signal, m, is between ± 1 with $f_{tri,max} >$ depth of modulation m_{max}. Therefore, the pulse width modulation signal to the switch Q_1 is given by:

$$\text{PWM}_1 = \begin{cases} 0, & \text{if } f_{tri} \geq m, \\ 1, & \text{otherwise.} \end{cases}$$

This logic is implemented on a control platform, for example a microcontroller. The

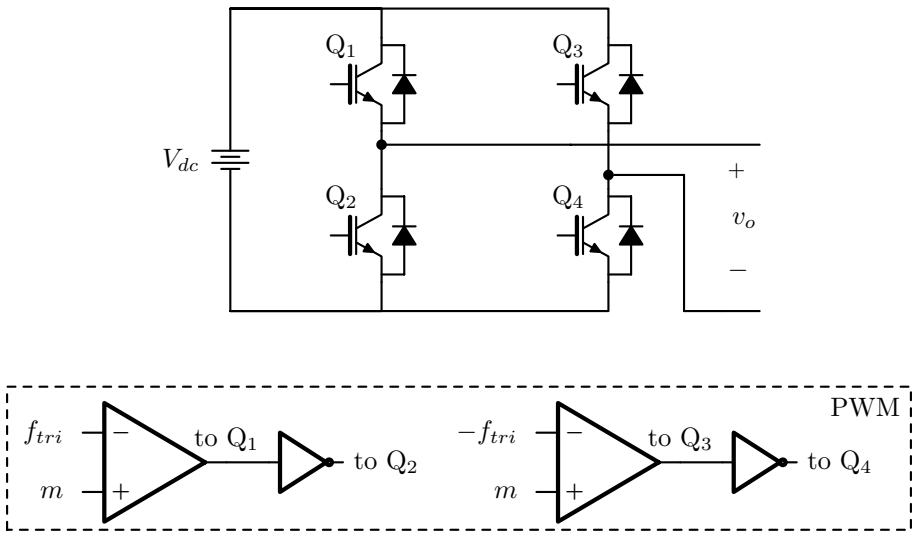

Figure 2.9: Full or H-bridge inverter.

microcontroller generates the carrier signal within itself and the control signal m is presented as input. An inverted PWM is supplied as a gating signal to switch Q_2. However, a deadband time gap is required between PWM_1 and PWM_2 to avoid shorting the legs of the half-bridge [3]. The output of the inverter is passed through a low pass inductor (L) or inductor-capacitor (LC) or inductor-capacitor-inductor (LCL) filter to eliminate the high frequency components of the switched voltage, v_o, thereby producing a smoother sinusoidal voltage, $\hat{v}_o$. Disregarding losses within the half-bridge circuit and the filter, the relationship between the control signal, m, and filtered output voltage, $\hat{v}_o$, is given by,

$$\hat{v}_o = m\frac{V_{dc}}{2}. \tag{2.1}$$

So, it is understood that the control signal, m is used to vary the output voltage, v_o of the inverter.

2.5.2.2 3-level H-bridge inverter

With half-bridge inverters, the maximum peak-to-peak output voltage is only one half of the DC side voltage, V_{dc}. For larger AC outputs one can use either a step-up transformer

on the AC side or a voltage booster on the DC side. This requirement can be mitigated using a full-bridge inverter. As shown in Figure 2.9 two half-bridges are connected in parallel to form a H-bridge inverter. Similar to a half-bridge inverter, the H-bridge inverter also operate on PWM switching. Two carrier signals, f_{tri} and $-f_{tri}$ are used to generate PWM signals for leg a (switches Q_1, Q_2) and leg b (switches Q_3, Q_4), respectively. From Figure 2.10 it can be observed that the output voltage of the inverter v_o is measured between terminals v_a (the voltage between leg a and common) and v_b (the voltage between leg b and common). This output voltage v_o also has three levels $(0, \pm V_{dc})$. The filtered output voltage, $\hat{v}_o$ for a H-bridge inverter is given by,

$$\hat{v}_o = mV_{dc}.$$

Therefore, the maximum output is the same as the DC voltage, V_{dc}. In reality, the peak-to-peak amplitude of the control signal m needs to be a little less than that of the carrier f_{tri} to ensure PWM accuracy and subsequently the sinusoidal shape of the signal. So the amplitude of m is generally chosen to be in the range of (0.7 - 0.8) units.

2.5.2.3 3-phase 6-switch inverter

A three-phase inverter is composed of three parallel half-bridge inverters as shown in 2.11. Here the control signal m, is a vector $\vec{m} = [m_a; m_b; m_c]$. The control signal m_a is phase shifted by $\frac{2\pi}{3}$ and $\frac{-2\pi}{3}$ to obtain m_b and m_c, respectively. Therefore, three distinct PWM waveforms are generated through modulation, which are then applied to the three legs of the inverters. The output voltage of each leg is $\frac{mV_{dc}}{2}$ on average.

From the circuit diagram of an averaged three-phase inverter shown in Figure 2.12, a state-space model of the inverter can be developed. Assuming equal filter parameters (L, C and R) on all three phases, i.e., $L_a = L_b = L_c = L$, $C_a = C_b = C_c = C$ and $R_a = R_b = R_c = R$, and applying Kirchhoff's voltage and current laws yield,

$$L\frac{d\vec{i}}{dt} = \vec{v_t} - \vec{v_s} - R\vec{i_l}, \tag{2.2}$$

$$C\frac{d\vec{v_s}}{dt} = \vec{i_l} - \vec{i_o}, \tag{2.3}$$

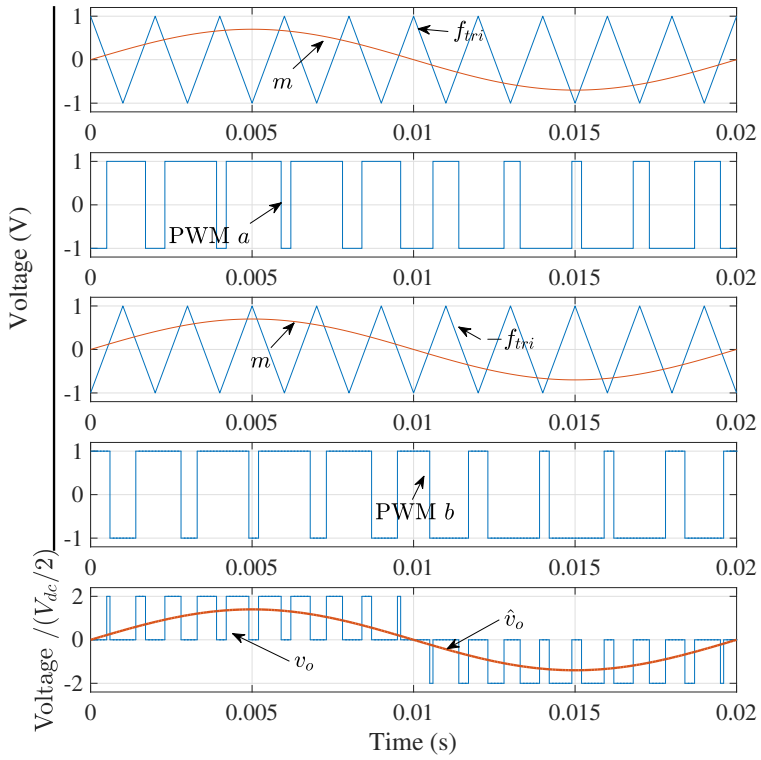

Figure 2.10: Full bridge inverter switching waveforms and output voltages.

where $\vec{i_l} = [i_{la}; i_{lb}; i_{lc}]$ is the vector inverter terminal current, $\vec{i_o} = [i_{oa}; i_{ob}; i_{oc}]$ is the vector inverter output current, $\vec{v_t} = [v_{ta}; v_{tb}; v_{tc}]$ is the vector inverter terminal voltage, and $\vec{v_s} = [v_{sa}; v_{sb}; v_{sc}]'$ is the vector inverter capacitor voltage. Substituting $\vec{v_t} = \vec{m}\frac{V_{dc}}{2}$, the equation (2.2) is transformed into:

$$L\dot{\vec{i_l}} = \vec{m}\frac{V_{dc}}{2} - \vec{v_s} - R\vec{i_l}. \tag{2.4}$$

Applying the synchronous frame transform (see Appendix A) to (2.4) and (2.3) yields,

$$\begin{aligned} L\frac{di_{ld}}{dt} &= m_d\frac{v_{dc}}{2} - v_{sd} - Ri_{ld} + L\omega i_{lq}, \\ L\frac{di_{lq}}{dt} &= m_q\frac{v_{dc}}{2} - v_{sq} - Ri_{lq} - L\omega i_{ld}, \\ C\frac{dv_{sd}}{dt} &= i_d - i_{ld} + C\omega v_{sq}, \end{aligned}$$

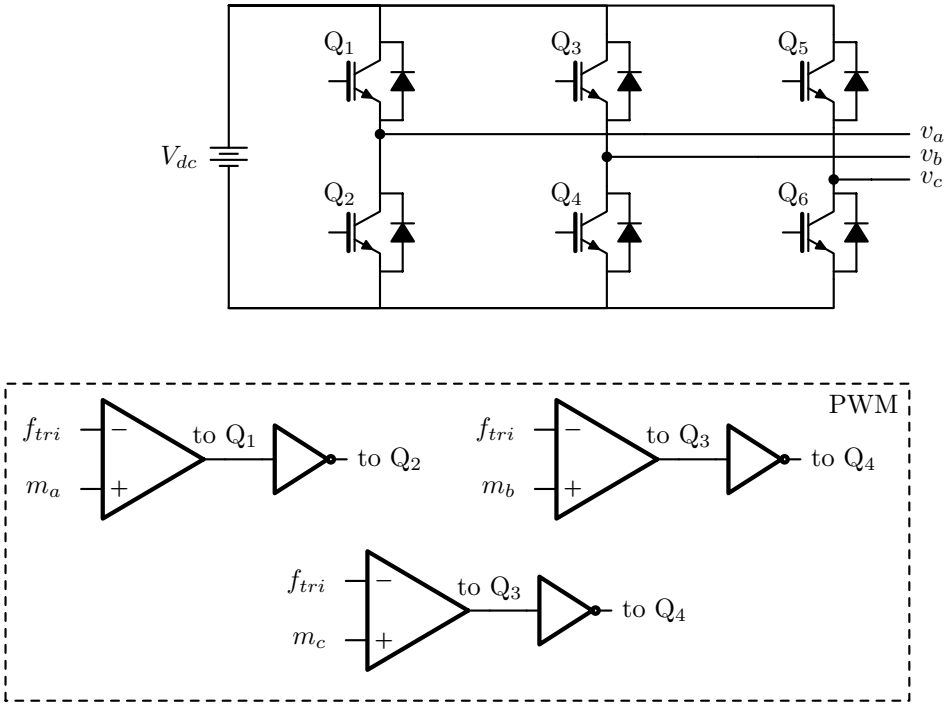

Figure 2.11: Three phase inverter.

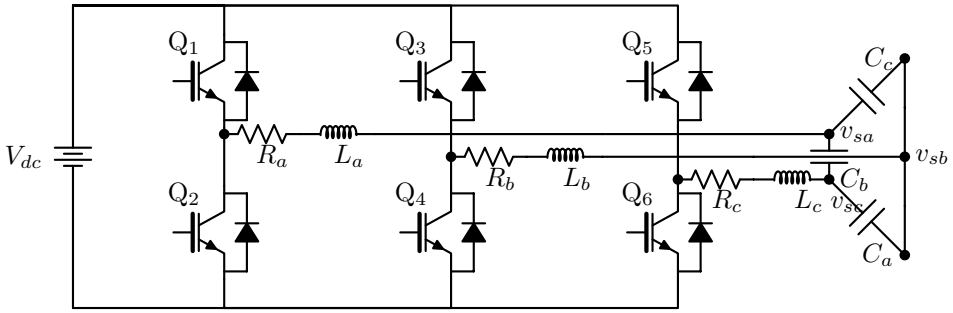

Figure 2.12: Simplified circuit model of a three-phase inverter with three phase LC filter supplying a microgrid.

$$C\frac{dv_{sq}}{dt} = i_q - i_{lq} - C\omega v_{sd},$$

where ω is the frequency of the sinusoidal control signal m. The importance of frequency, its evolution with time (ωt) and its relevance to the present work will be explicit in the subsequent chapters. From the above equations it can be seen that, if the currents and

voltages are fed-forward along with the frequency, the coupled system in synchronous reference frame is transformed into two decoupled subsystems making the measurement and control block design easier [158]. The frequency measurement is important since the decoupling process requires frequency information as shown in Appendix A. A state space model of the inverter in standard form:

$$\frac{dx}{dt} = Ax + Bu,$$

where $x = [i_d; i_q; v_{sd}; v_{sq}]$, $u = [i_{ld}; i_{lq}; m_d; m_q]$,

$$A = \begin{bmatrix} \frac{-R}{L} & \omega & \frac{-1}{L} & 0 \\ -\omega & \frac{-R}{L} & 0 & \frac{-1}{L} \\ \frac{1}{C} & 0 & 0 & \omega \\ 0 & \frac{1}{C} & -\omega & 0 \end{bmatrix} \quad \text{and } B = \begin{bmatrix} 0 & 0 & \frac{v_{dc}}{2L} & 0 \\ 0 & 0 & 0 & \frac{v_{dc}}{2L} \\ \frac{-1}{C} & 0 & 0 & 0 \\ 0 & \frac{-1}{C} & 0 & 0 \end{bmatrix}.$$

This state space model is typically used in designing application specific control for the converter. The next part of this chapter discusses the control techniques used in controlling power electronic converters in more detail.

2.5.3 Control of power electronic converters

2.5.3.1 Feedback control basics

Tracking a known reference signal can be achieved using feedback. For a better understanding, consider a physical system with transfer function $G(s)$ (in s domain[2]) with input and output in time-domain, u and y, respectively. Such a system can be represented by an input and output to the plant block (enclosed in dashed box) in Figure 2.13. Let y^* be the reference signal that should be tracked. Closing the loop using unity-gain output feedback, we generate an error signal, $(e = y^* - y)$ which is passed through a controller whose transfer function is $H(s)$. The output of the controller acts as the new input to the plant, $G(s)$. A set-up for feedback control is as shown in Figure 2.13. Let $U(s), Y(s)$ and $Y^*(s)$ be the Laplace transformations of their time domain counterparts

[2] s is a Laplacian operator.

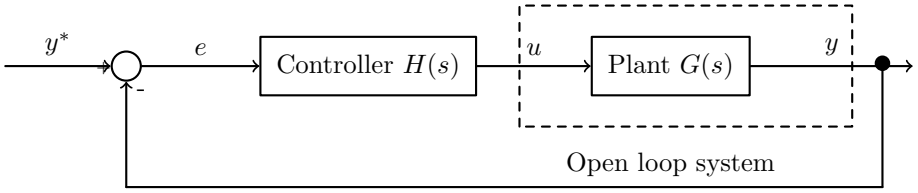

Figure 2.13: Closed loop system with unity-gain feedback.

u, y and y^*, respectively. The closed loop system will now have the form:

$$\frac{Y(s)}{Y^*(s)} = \frac{G(s)H(s)}{1 + G(s)H(s)}.$$

For efficient signal tracking, the compensator $H(s)$ is designed such that the gain of the closed loop transfer function becomes close to unity. Using standard frequency domain methods, such as *loop shaping* [158] or similar, the controller can be designed for application specific requirements.

2.5.3.2 Proportional-integral (PI) and Proportional-resonant (PR) controllers

In operating converters the reference signals can either be a DC signal or an AC signal. Controllers of the type known as Proportional-integral (PI) controllers are very efficient at DC signal tracking [167]. The transfer function of a PI controller is typically in the form:

$$H_{PI}(s) = k_p + \frac{k_i}{s},$$

where k_p and k_i are the proportional and integral gains respectively. With DC reference and as $t \to \infty$, zero steady state error is ensured in tracking as

$$\lim_{\omega \to 0} |H_{PI}(j\omega)| = \infty.$$

Employing a PI controller for AC or any other periodic signal tracking results in steady state amplitude and phase error [158] for common gains. Accurate periodic signal tracking can only be achieved by a high gain PI controller, which is hard to implement amidst various actuation constraints. On the other hand, various applications, especially in renewable energy generation, require AC signal tracking owing to network compatibility

issues[54].

A proportional resonant (PR) controller can be used to meet the metrics associated with AC signal tracking [142, 167]. The transfer function of a PR controller is typically in the form:

$$H_{PR}(s) = k_p + \frac{k_r s}{s^2 + \omega_o^2},$$

where k_p, k_r and ω_o are the proportional gain, integral gain and resonant frequency, respectively. It can be seen that the gain of the resonant term reach infinity at ω_o. Therefore, with proper design the steady state error is eliminated in tracking a sinusoid of frequency ω_o and a desired transient behaviour can be achieved simultaneously [54]. See [68] for more details on controllers and [109] for the design of output harmonic filters used in renewable energy generation.

2.5.3.3 Control of a grid connected half-bridge inverter

A half-bridge inverter with inductor filter is shown in Figure 2.14. Its dynamics are described by,

$$L\frac{di}{dt} = v_t - Ri - v_s, \tag{2.5}$$

where L is the filter inductance, R is the filter resistance, v_t is the inverter terminal voltage and v_s is the grid voltage. Applying a Laplace transformation to (2.5) yields,

$$sLi(s) = V_t(s) - Ri(s) - V_s(s).$$

Using (2.1), the open loop transfer function of the half-bridge inverter can be graphically represented as shown in Figure 2.15. For the system to supply a specific amount of power a closed loop current control is necessary[3].

The closed loop control of this system is given by Figure 2.16 (modified from [158]). The feedback error, $(i_{ref} - i)$ is fed through a controller. The output of the controller

[3]Only current control is required since the grid voltage is not manipulatable locally

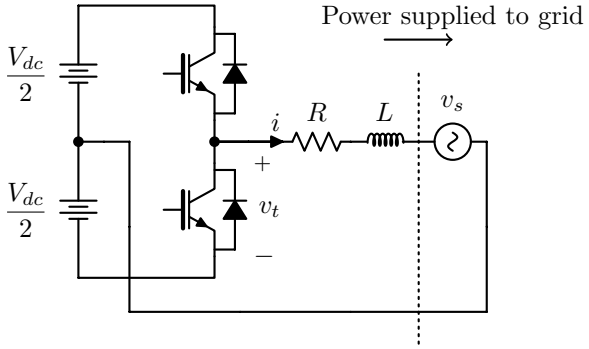

Figure 2.14: Grid connected half-bridge inverter.

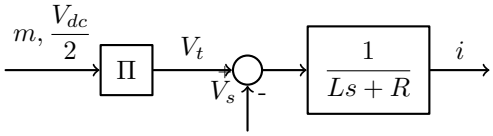

Figure 2.15: Open loop diagram of the grid-connected half-bridge inverter.

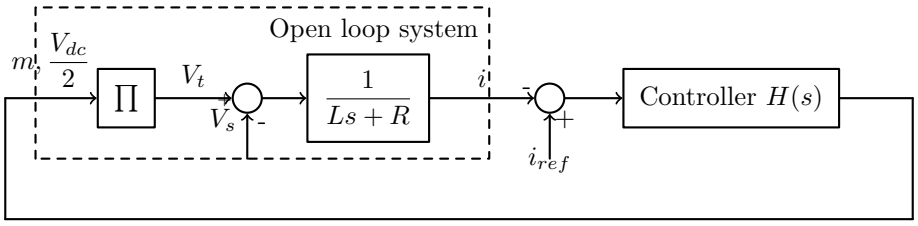

Figure 2.16: Closed loop control of grid-connected single phase inverter.

is scaled by the DC gain, $\frac{V_{dc}}{2}$ to compensate for its gains through the feedback loop and this becomes the modulating signal which drives the inverter. As discussed earlier, the controller is suitably chosen to ensure accurate tracking of the reference signal. Similar control can be applied to three-phase inverters. Since the phases a, b and c are coupled to each other in a three-phase system, decoupling transformations are used to transform these variables into independent variables and consequently reduce the complexity of implementation. See Appendix A for stationary reference frame ($\alpha\beta$) and synchronous reference frame (dq) transformations. Usually the current feedback control is used to provide a better dynamic performance and it is feasible to implement over-

current protection [68]. Voltage control is therefore indirectly achieved through current control. Various configurations and current control strategies of inverters are discussed thoroughly in [68, 158].

The grid interactive operation of an inverter based energy source requires a phase locked loop (PLL) for obtaining the voltage, frequency and phase information of the grid. The inverter controls use these frequency and phase angle values as references and follow them. Synchronization in frequency is a critical requirement here. The real and reactive power (P and Q) outputs of the inverter are subsequently controlled by the current controller using the phase variable as the reference input. Supplying current in-phase with the grid voltage corresponds to a real power supply (P at a power factor = 1) and out-of-phase corresponds to a real and reactive power supply (P and Q at a power factor $\neq$1). The current controllers for the three-phase operation are implemented in either a stationary reference frame ($\alpha\beta$) or synchronous reference frame (dq) to simplify the control and also preserve the three-phase coupling [158] as shown in the Appendix A.

2.5.4 Control in unbalanced conditions

Synchronous reference transformation converts three-phase balanced voltages into DC quantities. A proportional-integral (PI) control (DC signal tracking control) can therefore be used for balanced networks. In unbalanced networks, the synchronous reference transform does not result in DC quantities owing to the improper coupling between phases. Therefore, using stationary reference transformation is more appropriate when the networks are unbalanced or contain non-linear loads. A periodic signal tracking controller known as PR control can then be used to track the reference signals resulting from the stationary reference transformation [158]. Apart from power generation, power electronic devices are also used in static compensator [40] and other flexible AC transmission system devices [57]. Also, more details about single-phase phase locked loops can be found in [30], and three-phase phase locked loops can be found in [29].

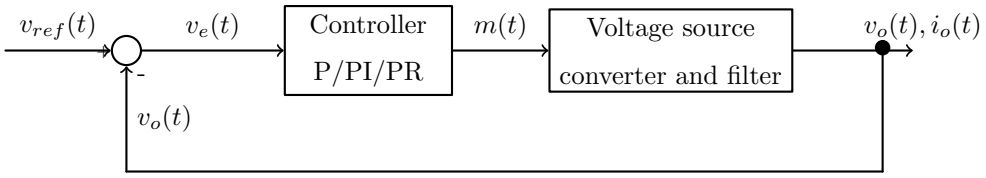

Figure 2.17: Single loop voltage controller for an islanded voltage source converter.

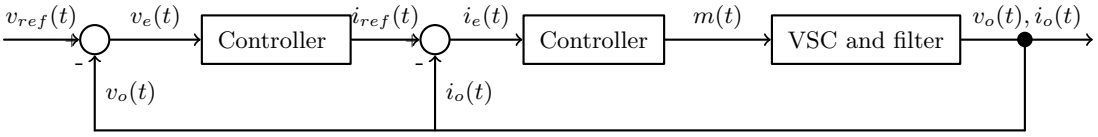

Figure 2.18: Dual loop voltage controller for an islanded voltage source converter.

2.5.5 Control of islanded converters

Controlling converters in islanded mode is an important topic for microgrids. Supply robustness is a key constraint in operation of a microgrid. The absence of the grid will present some requirements for the inverter apart from simple power (P and / or Q) control when compared to the grid-connected scenario. Typically, the primary requirement would be to maintain the frequency (AC) and the voltage (DC and AC) at a certain level when supplying a given load. This kind of control can be accomplished in two ways: a) a single loop voltage regulator as shown in Figure 2.17 or b) a dual loop voltage regulator as shown in Figure 2.18. Either of these systems use the load voltage as feedback signal to estimate the error between the present and the desired voltage and subsequently command the PWM switching in a way that the desired voltage is reached, in terms of either frequency or amplitude or both. However, the dual loop controller shown in Figure 2.18 presents a few advantages like better transient performance and overcurrent protection, when compared to the single loop method. Observe that both the methods will need a reference voltage signal ($v_{ref}(t)$, DC or AC) for tracking which can be generated by manual set-point methods or based on power or current feedback loops. These reference generating subsystems of islanded converter control will be discussed in the more detail in the later parts of this work.

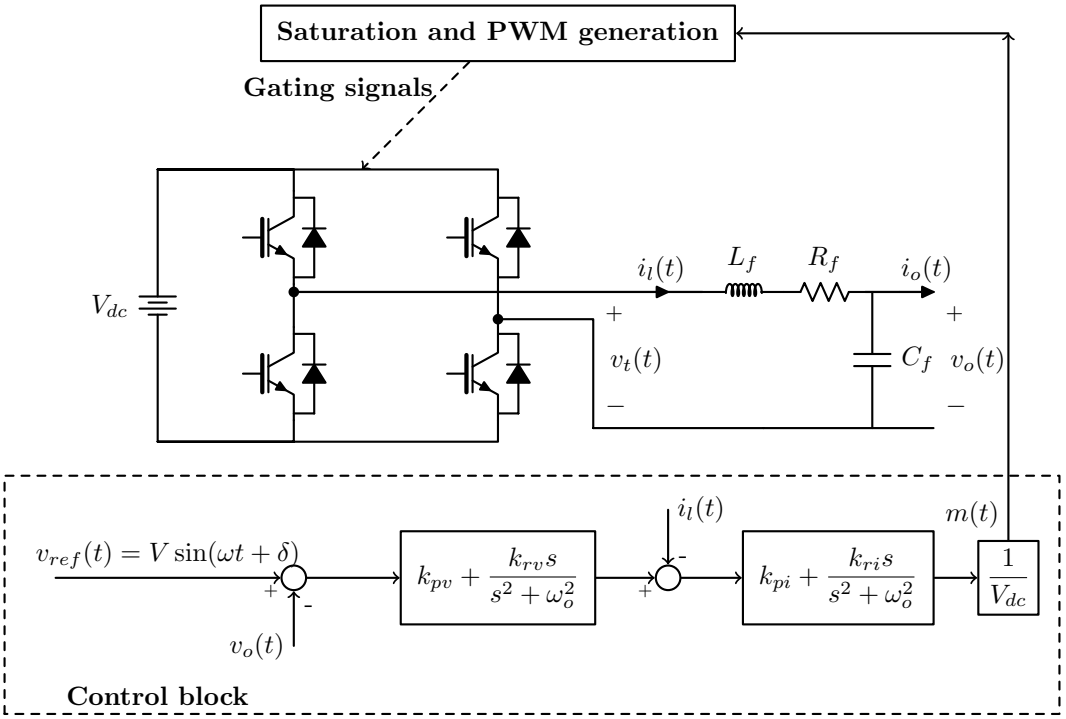

Figure 2.19: Dual loop control voltage control based voltage source inverter.

2.6 Energy Storage

Energy availability is crucial for the reliable operation of microgrids. If there is a sufficient amount of base load being generated from traditional sources, a significant amount (approximately 50%) of renewables can be tolerated [34]. However, in most cases energy storage becomes imperative for renewable energy penetration beyond half the microgrid capacity. The reason being its intermittent nature - the generation variability of renewable energy sources can cause energy deficiencies which might disrupt microgrid operation. For example, a large cloud passing over a local solar farm can cause an immediate power shortage and jeopardize supply. Improvements can be made to the renewable energy penetration levels if load shedding can be used to compensate for intermittent supply. Microgrids are less able to use such solutions due to the presence of critical loads. Energy storage provides more flexibility for balancing generation and

Table 2.1: A summary of various storage technologies [141].

Parameter	Battery	Flywheel	SMES	SuperCap	NaS
Efficiency (%)	60 - 80	95 - 98	95 - 98	95	70
Energy density (Wh/kg)	20 - 200	5 - 50	30 - 100	<50	120
Power density (W/kg)	25 - 1000	10^3 - 5×10^3	10^3 - 10^5	4000	120
Response time (ms)	30	5	5	5	<100
Cycle life (no. of cycles)	200 - 2000	>2000	10^6	>5000	2000
Cost (US$/kWh)	150 - 1300	380 - 2500	high	250 - 350	450

demand and therefore is considered essential to increase the proportion of renewable energy generation in microgrids. A brief summary of energy storage technologies which have potential application in microgrids is given in Table 2.1.

- *Electrochemical* or *Battery storage* - Batteries store energy in the form of electrochemical reactions. Some examples of battery chemistries are, Lead-acid, Nickel-cadmium (NiCd), Nickel-Iron, Lithium-Ion etc. They all have reasonable efficiency and power density.

- *Flywheel energy storage* - energy in the form of rotational kinetic energy is stored in flywheels. Their efficiency and power density are higher than that of electrochemical storage but the limiting factor remains their cost.

- *Superconducting magnetic energy storage* (SMES) - In this type of energy storage, a superconducting magnetic field stores energy. These are highly efficient with very high power density. Since this type of storage inherently relies on conducting material and stabilizers, their cost has to be considered in estimating its price per capacity.

- *Supercapacitors* - in this type of energy storage technology energy is stored in the two series capacitors with a electrical double layer in between. Their efficiency is comparable to flywheel energy storage.

- *Sodium Sulfur* (NaS) batteries - Extensive research is being carried out on sodium-sulfur batteries to increase the energy density reduce their operating costs.

2.7 Preliminaries of Lyapunov's indirect method

Lyapunov's indirect method uses linearization of a system to determine its stability around an equilibrium. Let us consider a system

$$\dot{x} = f(x, t),$$

with $f(x_0, t) = 0$ for all $t \geq 0$. Here x is the state vector, x_0 is the equilibrium vector, $f()$ is a function that determines the evolution of the states and t represents time. Let

$$A(t) = \frac{\partial f(x,t)}{\partial x}|_{x=x_0}$$

be the Jacobian matrix of $f(x, t)$ with respect to x evaluated at the equilibrium. Let us also define a time independent linearized system

$$A = \frac{\partial f(x)}{\partial x}|_{x=x_0}$$

which is obtained by linearizing the time independent non-linear system $\dot{x} = f(x)$. The eigenvalues of A (or $A(t)$ in the time dependent case) determine the local stability of the system i.e., the stability of the system $f(\cdot)$ around the equilibrium x_0. The Jacobian matrix A defines three main subspaces:

- The space spanned by the generalized eigenvectors corresponding to the eigenvalues λ with real part $\Re(\lambda) < 0 \ \rightarrow$ stable subspace;
- The space spanned by the generalized eigenvectors corresponding to the eigenvalues λ with real part $\Re(\lambda) > 0 \ \rightarrow$ unstable subspace; and
- The space spanned by the generalized eigenvectors corresponding to the eigenvalues λ with real part $\Re(\lambda) = 0 \ \rightarrow$ center subspace.

We refer to [101] for more details.

2.8 Summary

Predominantly renewable energy based microgrids rely on a master source/s backed by energy storage to produce the voltage the converter controls can use as a reference and work as grid-connected systems. Design and placement of energy storage systems becomes crucial for such master-slave microgrids systems. However, in the next chapter we see some control techniques that do not rely directly on master source/s for microgrid operation. We identify the advantages and disadvantages of the techniques which will then allow us to formulate precise research questions.

✧✧✧

3

Microgrids

Microgrids will evolve to become a "fundamental building block" of the 21st-century grid.

– NEMA [104]

3.1 Interaction between AC voltage sources

MULTIPLE sources must be connected together to increase the overall generation capacity within a microgrid. There are two simple ways of connecting multiple sources: 1) designate a master source and allow the remaining sources to follow the master source's voltage and supply real and/or reactive power - a master-slave topology; and 2) connect sources in parallel - a master-less topology. This chapter will provide an introduction to master-slave and master-less microgrids following the principles covered in Chapter 2. One main benefit of connecting sources in parallel, rather than connecting them in a master-slave topology, is to improve the robustness from loss of generation. Typically, these generators are voltage sources that, in the ideal scenario, share the load in proportion to their power ratings. This phenomenon is known as *power sharing* or *load sharing*.

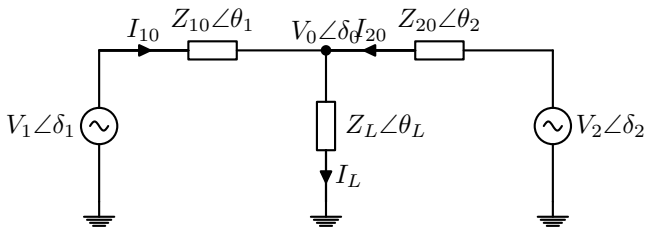

Figure 3.1: Power flow within a system consisting of two voltage sources supplying a common load.

Why is power sharing important?

- Coordination amongst sources is of utmost priority given that the microgrid scenarios are energy limited in most cases - especially when sources with a power electronic interface have some power limitations[67].
- Power sharing can be implicitly used to achieve energy balance between sources.
- In microgrids, lines are typically heavily loaded to allow maximum utilization which makes the system stability susceptible to small disturbances in power sharing. Disproportionate power sharing may also cause system outages in some cases[137].
- Energy capacity or state of charge (SoC) estimation of storage systems becomes easier for given initial conditions.
- Global parameters such as frequency, can be used to estimate the global load and thereby deduce the loading on each source.

Power sharing between any two voltage sources operating at the same constant frequency can be described using simple proportional approximations when the constituent network is dominantly inductive or dominantly resistive. Here, we revisit a simple power sharing example presented in [77]. When both voltage sources in Figure 3.1 are operating at an exact common frequency, we can represent them by $V_i\angle\delta_i$ using phasor notation. Subsequently, the phasor power flow between the source at node 1, represented by $V_1\angle\delta_1$,

and load at node 0, represented by $V_0\angle\delta_0$, is given by:

$$\underline{S}_{10} = P_{10} + jQ_{10} = \underline{V}_1\underline{I}_1^* = \underline{V}_1\left(\frac{\underline{V}_1 - \underline{V}_0}{\underline{Z}_{10}}\right)^*, \tag{3.1}$$

where the complex variable $\underline{S}$ represents apparent power, $\underline{I}$ represents current, $\underline{V}$ represents voltage and $\underline{Z}$ represents impedance as a complex sum of resistance R and (imaginary) reactance X and the subscript $(\cdot)_{10}$ indicates flow direction from node 1 to node 0. Expanding the equation (3.1) we obtain real and reactive powers:

$$\begin{aligned} P_{10} + jQ_{10} &= \frac{V_1^2(\cos\theta_1 + j\sin\theta_1)}{\sqrt{R_{10}^2 + X_{10}^2}} - \frac{V_1V_0(\cos(\delta_1 - \delta_0 + \theta_1) + j\sin(\delta_1 - \delta_0 + \theta_1))}{\sqrt{R_{10}^2 + X_{10}^2}}, \\ &= \frac{V_1^2\cos\theta_1 - V_1V_0\cos(\delta_1 - \delta_0 + \theta_1)}{\sqrt{R_{10}^2 + X_{10}^2}} + j\frac{V_1^2\sin\theta_1 - V_1V_0\sin(\delta_1 - \delta_0 + \theta_1)}{\sqrt{R_{10}^2 + X_{10}^2}}. \end{aligned} \tag{3.2}$$

For arbitrary values of resistance and reactance, the coupling between voltage, phase angle, real power and reactive power is very complex. However, for inductive lines (or for systems having inductive output impedances) we can use the property $X/R \gg 1$. This means that the impedance angle is approximately equal to $\frac{\pi}{2}$ radians. Substituting $R \approx 0$ and $\theta_1 \approx \frac{\pi}{2}$ in (3.2) yields,

$$P_{10} \approx V_1V_0\sin(\delta_1 - \delta_0)/X_{10}, \tag{3.3}$$

$$Q_{10} \approx V_1(V_1 - V_0\cos(\delta_1 - \delta_0))/X_{10}. \tag{3.4}$$

For small angle differences $(\delta_1 - \delta_0)$ the trigonometric (sine and cosine) functions in (3.3) and (3.4) can be replaced by their truncated Taylor series expansions:

$$\begin{aligned} \cos(\delta_1 - \delta_0) &\approx 1, \\ \sin(\delta_1 - \delta_0) &\approx (\delta_1 - \delta_0). \end{aligned}$$

Substituting these truncated values in (3.3) and (3.4) results in,

$$(\delta_1 - \delta_0) \cong \chi_{10}P_{10}, \tag{3.5}$$

$$(V_1 - V_0) \cong \chi_{10}Q_{10}V_0, \tag{3.6}$$

where $\chi_{ij} \triangleq X_{ij}/(V_i V_j)$, is the reciprocal of maximum power that can flow between nodes i, j at any given instance. As observed from (3.5) and (3.6), the amount of real power flowing between two nodes can be controlled by altering the phase angle between them and the amount of reactive power flowing can be controlled through voltage variations.

3.2 Parallel operation of converters

As discussed earlier, integrating a number of inverter based energy sources operating in isolation as a microgrid is a challenging task and many technical issues may arise [82]. This section presents a literature review of such microgrid structures along with strategies used for power sharing, frequency and voltage control.

> **Note:** This part of the literature is based on a recent modification to IEEE Standard 1547.2003 [17] in 2011 [140] which allows intentional islanding. Any anti-islanding schemes (for example [28]) that may normally exist are disabled in such approved islanded microgrids.

3.2.1 Load sharing techniques

One simple way to share loads in an electrical network is to determine the desired power set-points for each inverter using some sort of communications and then to use these set-points in a communication-based master-master topology. Another alternative is a communication-based master-slave topology where a central converter control assigns power set-points to all the other inverters depending upon their power ratings and the master converter's capacity [59]. Traditional master-slave topology is an implicit communication-based load sharing technique as reported in [151, 153]. In this type of control a master inverter maintains the voltage and frequency of the entire microgrid and the slave inverters follow the master inverter's voltage and frequency information while supplying the desired (or available) amounts of real and reactive power.

A PLL based system can be used to obtain the local voltage and frequency information for the slave inverters. This type of architecture reflects a grid formation. Therefore the strength and reliability of the master inverter dictates the reliability of the microgrid. This master-slave configuration is deemed to be a weak strategy due to the associated robustness to loss-of-generation, especially at the master[82]. However, some works have parameterized the energy requirements for such systems. According to [78, 79] the master inverter should have at least 5% energy rating compared to the entire microgrid it is supporting. While their metric gives us an insight into the energy requirement for master-slave control, there is no standard measure that guarantees stability under generation uncertainty known to us.

3.2.2 Virtual inertia for inverters

Master-less or parallel operation of sources within a microgrid can be achieved when the sources are operating in voltage control mode, i.e., when their output voltage is controlled (as seen in Section 2.5.5). Synchronous generators are voltage sources and are well known to work in parallel [77]. One main difference between a simple sinusoidal wave generator and a synchronous generator is how the latter's output voltage depends on it's mechanical characteristics. We have seen that inertia plays an important role in the dynamics of synchronous machines in Section 2.5.1. Intuitively, connecting sources in parallel becomes easier if inverters can behave in a manner similar to synchronous machines. However, inverters are not capable of generating an inertial response naturally since there are no rotating parts involved. Therefore, a virtual inertia behaviour must be introduced into the inverters to mimic synchronous generator operation. Since the inverters are controlled by fast processors and respond to changes very quickly, the inertial response emulation can be achieved with ease by using a closed loop voltage control. Chandorkar et al., first introduced frequency and voltage droop controllers for inverters [26]:

$$\omega_i = \omega^* - m_i \times (P_i - P_i^*), \tag{3.7}$$

$$V_i = V^* - b_i \times (Q_i - Q_i^*),$$

where ω^*, V^*, P_i^* and Q_i^* are the global nominal (rated) frequency, global nominal voltage, local nominal real power and local nominal reactive power, respectively. The constants m_i and b_i are the droop coefficients to modify real and reactive power, respectively and are given by,

$$m_i \leq \frac{\omega_{max} - \omega_{min}}{P_{i,max} - P_{i,min}} = \frac{\Delta\omega}{\Delta P_i},$$
$$b_i \leq \frac{V_{max} - V_{min}}{Q_{i,max} - Q_{i,min}} = \frac{\Delta V}{\Delta Q_i},$$

where subscripts $(\cdot)_{min}$ and $(\cdot)_{max}$ denote the minimum and maximum allowable values of the parameter, respectively. The permitted range for frequency variations is $\pm 0.2\%$ [13] and voltage variations is $+10\%$ and -6% [15] in Australia.

In an attempt to facilitate power sharing, some design conditions on droop coefficients and nominal power ratings were also introduced in [26]. They are:

$$m_i P_i^* = m_j P_j^* := \xi \quad \forall i, j = 1, \ldots, n, \tag{3.8}$$

$$b_i Q_i^* = b_j Q_j^* := \kappa \quad \forall i, j = 1, \ldots, n, \tag{3.9}$$

where n is the number of inverter based distributed generators in the microgrid that are using droop control. The power sharing properties of the constituent sources can be understood as follows. The total load in the microgrid is given by the sum of the load and line losses. The converter-based sources, however, cannot distinguish between loads and losses since they use local feedback. When (3.8) and (3.9) are used in designing the droop coefficients, power sharing may be achieved between the inverters without any explicit communication. Here, power sharing refers to the actual power consumed and the losses being shared proportionately. A typical inverter interfaced microgrid is given in Figure 3.2.

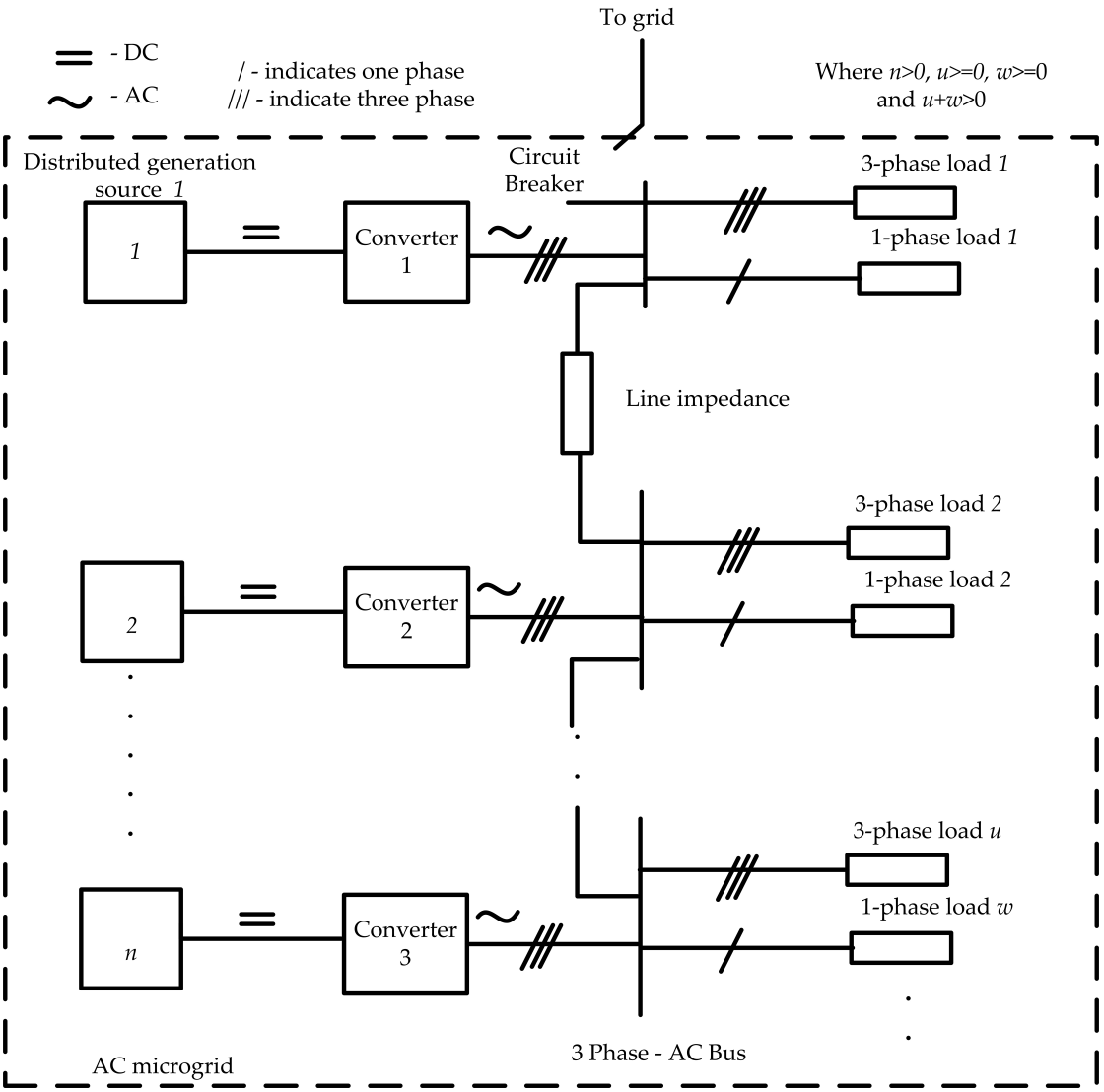

Figure 3.2: An example inverter-interfaced AC microgrid with n inverters, u 3-phase loads and w single-phase loads.

3.2.3 Power sharing by droop control: an illustrative example

Real power sharing between two inverters using frequency droop control is illustrated in Figure 3.3. The droop coefficients are represented by lines with negative slopes, m_1 and m_2 on the frequency axis. Their gradients are different indicating different power sharing capacities. At time, $t = t_o$ the real power supplied by each inverter is $P_1^* = P_2^* = 0$W.

Recall that the condition $m_i P_i = m_j P_j$ for $m_i \neq m_j$ and $P_i^* = P_j^*$ is satisfied only at $P_i^* = P_j^* = 0$W. Therefore, the total load on the system is 0W. The frequencies corresponding to these powers are $\omega_1^* = \omega_2^* = \omega^*$. Suppose a load change occurs at time $t = t_o + T$ and; from the design criteria, we can clearly see that the real powers $P_1(t_0 + T)$ and $P_2(t_0 + T)$ are not equal owing to the non-identical droop slopes. The system frequency is synchronized to a new (lower) value $\omega_{sync} = \omega_1(t_0+T) = \omega_2(t_0+T)$.

The relationship between voltage and reactive power also descends in a similar fashion, albeit there may be no single synchronous voltage as a result of disproportionate impedances (if any). To improve the transient response of the $(P - \omega)$ droop, integral (only used in grid-connected mode) and derivative terms are added to the proportional droop controller [45]. Proper tuning of these terms will ensure zero steady state error in tracking reference powers in grid-connected mode and better transient performance of the inverters [150]. Altogether, this power sharing control technique is generally known as *primary microgrid control*. In an ideal scenario, islanded converters that are using frequency droop as their control law only achieve accurate power sharing, voltage stability and frequency synchronization. The steady state deviations (from nominal values) in frequency and voltage are addressed by controllers that work on a slower time-scale. This is known as secondary control and it will be discussed in the later parts of this chapter.

3.3 State-of-the-art

3.3.1 Network characteristics and their effect on power sharing

From (3.2) it can be observed that real and reactive power decoupling and power sharing between inverters is highly dependent on the output / network impedance. With network cables offering a significant proportion of impedance in some cases, a closer look into the cable inductance and resistance characteristics provides a better intuition into power sharing. Table 3.1 gives the approximate cable reactance-to-resistance ratios at various

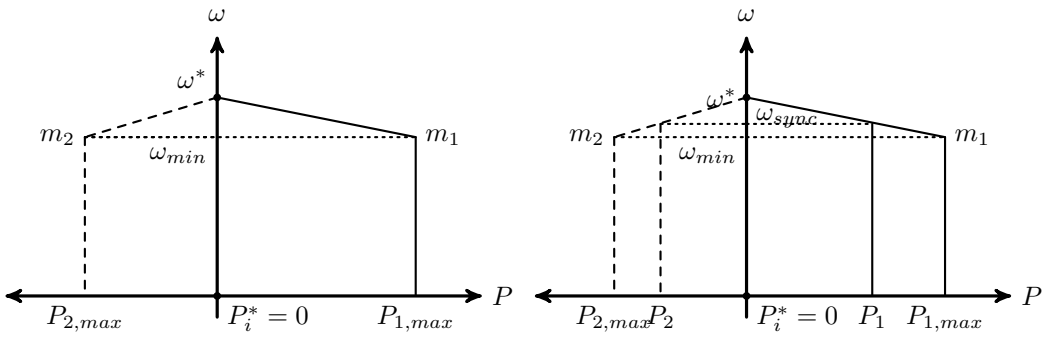

Figure 3.3: Power sharing between two inverters via conventional droop control. Load is increased at time $t = t_o + T$. (left) $P - \omega$ characteristic of the two inverter system at time $t = t_o$ and (right) at time $t = t_o + T$.

Table 3.1: Cable reactance-to-resistance (X/R) ratios at various voltage levels.

Voltage level	Low Voltage	Medium Voltage	High Voltage
Type of network	Distribution	Sub-transmission	Transmission
Voltage range (kV)	< 10	$10 <$ MV < 100	>100
X/R **ratio** (p.u)	$\ll 1$	≈ 1	$\gg 1$

voltage levels. The $(P - \omega)$ and $(Q - V)$ droop controls work satisfactorily for inverters operating in high voltage networks where the cable X/R ratio is very high. Conversely, for networks with low or medium X/R ratios the droop controls do not achieve desired synchronization and power sharing objectives.

By substituting a low reactance-to-resistance (X/R) ratio into (3.2) and following a similar deduction procedure, we conclude that voltage affects real power and concurrently the phase angle plays a primary role in reactive power transfer. Building on this characteristic, several authors [80, 148] introduced reactive power - frequency, $(Q + \omega)$ boost and active power - voltage, $(P - V)$ droop controls.

A transformation matrix method is introduced in [32] which takes, as inputs, the

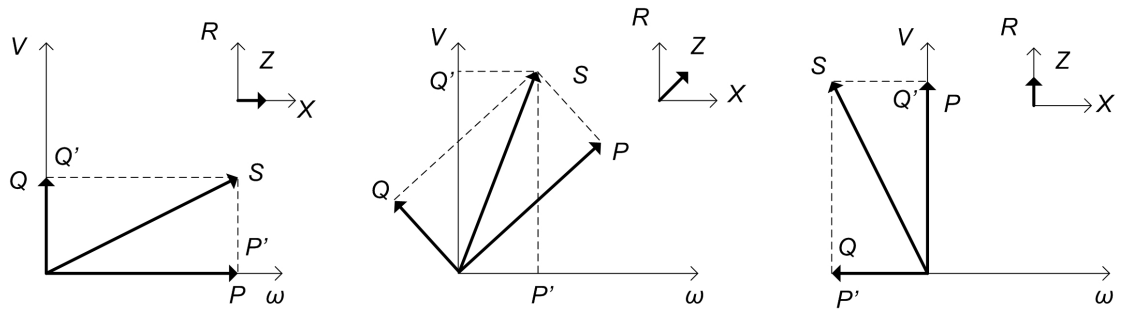

Figure 3.4: Influence of real and reactive power on voltage and frequency for different line impedance ratios, (left) high voltage networks; (centre) medium voltage networks; (right) low voltage networks.

real and reactive power and transforms them into suitable quantities (using the cable reactance-resistance ratios) in a manner that allows the conventional $(P-\omega)$ and $(Q-V)$ droops can be used in any type of network. In [113] a detailed explanation is given about how the droop controller should be modified for different output/network impedances. This explanation uses a transformation matrix method that follows from (3.2) and is given by equation (3.10). The influence of impedance on real and reactive power is shown graphically in Figure 3.4.

$$\begin{bmatrix} P' \\ Q' \end{bmatrix} = \begin{bmatrix} \frac{X}{Z} & -\frac{R}{Z} \\ \\ \frac{R}{Z} & -\frac{X}{Z} \end{bmatrix} \begin{bmatrix} P \\ Q \end{bmatrix} \tag{3.10}$$

3.3.2 Virtual impedance emulation

Extending conventional $(P-\omega)$ and $(Q-V)$ droop techniques to operate at any voltage level is useful. This is especially true when all the well established theories from conventional droop control of synchronous machines can be applied to converter based sources with little or no modification. Consider the situations where:

1. the per-unit output impedances of all the inverters that are being operated in parallel should be same to achieve accurate reactive power sharing [162].

2. the impedance design is a critical step to achieve a desired transient response in real power sharing.

Drawing motivation from these requirements the authors of [45] and [32] introduced techniques which are in general known as virtual impedance emulation. This method allows impedance matching to provide the desired interaction between paralleled inverters. Subsequently, using this emulation technique the inverter behaves as an inductive output voltage source and facilitates the use of traditional droop equations at any voltage level without line loss trade-off. A simple control diagram shown in Figure 3.5 illustrates the processes involved in implementing a droop controlled inverter. The droop equations determine the reference signal (in terms of voltage and frequency). The dual loop voltage regulation scheme is used in this case. The outer voltage loop and inner current loop together provide the modulating signals to the PWM switching scheme. The virtual impedance modifies the reference signal at each inverter as:

$$v_{i,ref}^{new}(t_i) = v_{i,ref}(t_i) - i_o(t_i)R_v - L_v\frac{di_o}{dt_i},$$

where i_o is the output current, R_v and L_v are the desired output virtual resistance and inductance, respectively.

While virtual impedance emulation can cope with the reactive power (or real power in low voltage networks) sharing problems, its design and analyzing large networks that use virtual impedance matching between sources is not straightforward [83]. Moreover, the changes in the frequency (as normally seen in droop controlled systems) will introduce some major complications in the virtual impedance loop design. Adaptive virtual impedance [45] is a possible solution but increases the complexity and subjects the system to unforeseen new dynamics.

A scheme to regulate the effect of load on load voltage and consequently power sharing was proposed in [116]. But the proposed scheme fails to capture the effect of droop control on power sharing. Both the effects of load voltage drop and the voltage drop

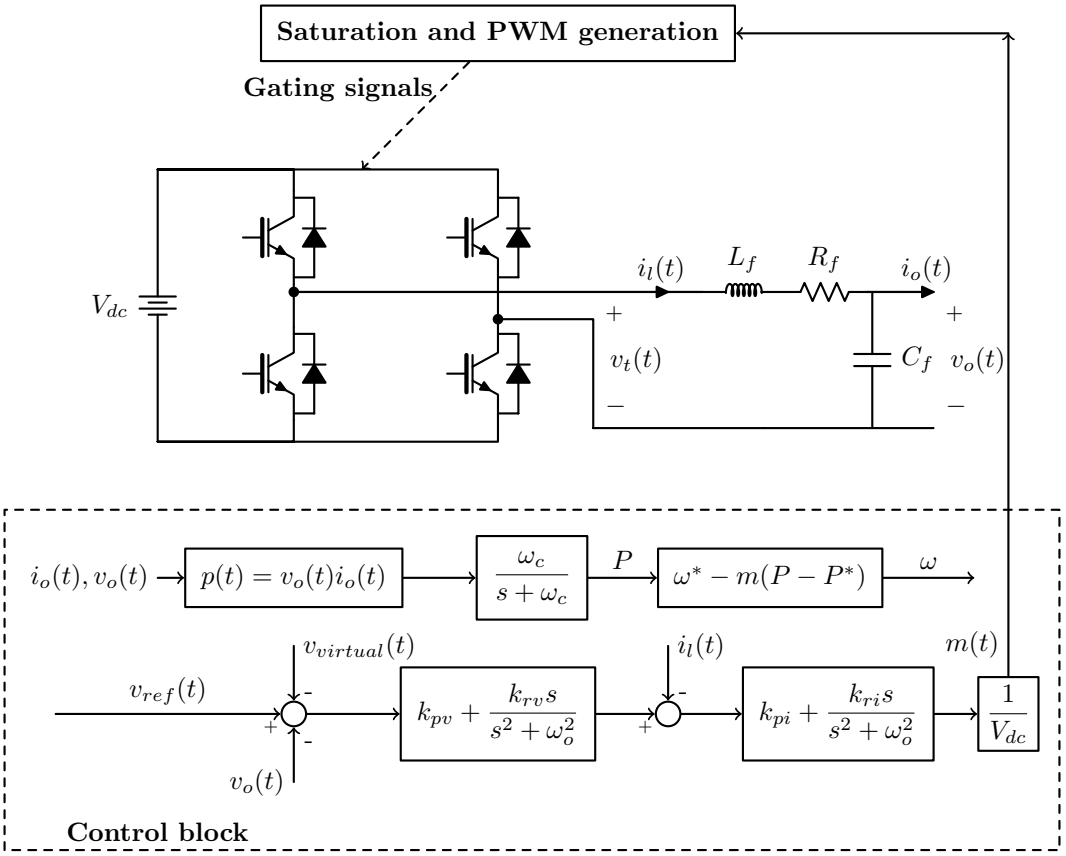

Figure 3.5: Implementation block diagram for a single phase inverter system with virtual output impedance.

induced by droop control can be captured using the method introduced in [162], where a robust droop controller is presented to achieve accurate power sharing in networks with disproportionate impedance distribution without using virtual impedance. This method uses (communicated) load voltage to modify the droop voltage and uses the modified voltage as a control input to achieve accurate power sharing.

In [113] $(P - \omega)$ droop and $(Q + V)$ boost controls are analyzed for inverters with capacitive output impedance emulation. This work is an enhancement of [161, 165] where the output impedance of the inverter is controlled to behave like a capacitor. Although capacitive impedance emulation has little relevance to impedance matching

and power sharing for microgrids, it could be used to reduce the total harmonic distortion (THD) of the system. A question, "does capacitive impedance emulation behaves like a capacitor in all ways?" has not been addressed.

3.3.3 Other parallel operation techniques for AC microgrids

As discussed in Chapter 2 the DC side of the converter based sources could either be a source or a combination of a source and storage. Both DC and AC variables are indicative of some important parameters with the source and using them may provide a higher degree of flexibility in the microgrid. Based on this and also based on conserving the qualitative behaviour of droop control presented in [26], many different droop based technologies have been derived to achieve specific aims. They can be broadly divided into three categories based on the choice of variables utilized: 1) those based on AC side variables, 2) those based on DC side measurements, and 3) hybrid control techniques.

3.3.3.1 Control based on AC variables

With little modification to traditional droop control, the paper [45] proposed an improved droop control where integral coefficients are used together with the proportional coefficients to achieve better steady-state behaviour for grid-connected microgrids. A major droop control scheme is the angle droop control introduced in [92, 94]. Using relationship between angle difference and real power flow (3.5), the phase angle, δ is chosen as the control variable to achieve real power sharing, instead of the frequency. However, since there is no equivalent alternative to voltage, no changes are made to the reactive power controller. The local measurements of voltage and current are used to obtain the real and reactive power. The real power is then used in the angle droop control equation (3.11) to obtain the desired output angle.

$$\delta_i = \delta_i^* - m_i \times (P_i - P_i^*). \tag{3.11}$$

These angle measurements at each inverter have to be calculated over a common time / frequency reference, for example 50 Hz. This angle droop controller is modified from

a simple proportional control to a robust proportional-differential controller in [93] to improve the transient performance. Furthermore, in [164] all the parameters (such as excitation current, damping ratio, moment of inertia, etc.) are added to the inverter control forming a "synchronverter". It is shown that this kind of inverter mimics all aspects of the synchronous generators. Grid connected operation of synchronverters is presented using simulations results. The authors also remark that the droop control is implicitly followed when synchronverters are operated in parallel increasing the interoperability.

3.3.3.2 Control based on DC variables

A change in the DC link voltage is used as an energy balance indicator in [147]. They proposed a control technique which uses the inverter DC terminal voltage as a droop parameter to regulate its AC terminal voltage based on this energy balance phenomenon. It appears that measurement accuracy may play a major role in implementation of this control methodology. Acknowledging this fact, they have modified their droop scheme to capture the balance between dispatch capacity and available energy of the energy source. Here the inverters are operated either using conventional (or reversed droop) controls or the DC link voltage droop control depending on the power available at the DC side. They have also identified that the normalized DC link voltage can be used as a global variable for estimating various characteristics of such microgrids [145].

In [89], a state-of-charge based droop control is presented where the battery source with highest state-of-charge injects more power into the microgrid, assuming the initial conditions of the batteries are known. Considering the battery capacity level, a simple (inverse) proportional change in droop coefficients is presented in [47] as shown below,

$$m = \frac{m_{min}}{\alpha},$$

where m_{min} is the droop coefficient at full charge and $0 < \alpha < 1$ is the level of charge of

the battery. To ensure bounded droop values, the battery charges are saturated between 1 and 0.01.

3.3.3.3 Hybrid control techniques

Communication based power sharing between parallel inverters based on droop control considering both the DC and AC side variables is another important area for research. Several groups [87, 98, 99, 103] discussed the application of communication based consensus control in improving the power/energy sharing and state-of-charge balancing capabilities of droop controlled inverters connected in parallel. Communication based consensus voltage droop control for accurate reactive power sharing is discussed in [121].

Several papers of Shoeiby et al. [128–130] have identified the limitations droop control introduces, especially in the loss of current control on the voltage. To mitigate this limitation they have introduced a technique to operate parallel inverters using current control. Their current control strategy is combined with a predictive voltage controller to achieve voltage stability and a current droop controller to achieve better (somewhat less accurate) power sharing between inverters. In the most recent of these papers [130], they claim that the current controller they identified has an intrinsic droop characteristic that causes deviations in system frequency. Based on this observation, they introduce a frequency regulator based current control to mitigate the drawback of the current control strategy in [128]. Grid connected operation of the current controlled microgrid is discussed in [129]. Power sharing accuracy of these current-control techniques is influenced by the impedance distribution between converters, making proper impedance design an imperative.

Some recent works [35, 63–65, 138] proposed a virtual oscillator type control of inverters to facilitate parallel operation. Making use of the fast response time provided by power electronic devices, the inverters are controlled to emulate non-linear "deadzone" oscillators using only local information. Their results show better power sharing and

transient response compared to the simple droop controlled inverters [138].

3.3.4 Dynamic stability and frequency synchronization

Stability of conventional droop controlled microgrids based on the design parameters such as, droop co-efficients, power filter cut-off frequencies, etc has been the focus of papers [21, 47, 111, 119]. Detailed dynamic (state space) models of constant impedance load microgrid systems are developed in [111, 119, 122]. The non-linearities in the dynamics of each subsystem are linearized and combined to form a small signal dynamic model of the entire microgrid. In [119] some conditions that guarantee the stability of the linearized dynamical system are proposed. On the other hand, in [111] the eigenvalues of a typical microgrid example are calculated and the power controller is reported to be the most sensitive part of the entire system. For fixed system parameters the stability of their microgrid model is very sensitive to any change in the droop gains. Their study also examines the effect of both voltage and current controller gains and harmonic filter parameters on system stability. A sensitivity analysis (from system eigenvalues) is performed on their linearized system to identify the participation of different state variables in system stability. In general, linearized approaches have been very popular and important in analyzing microgrid stability.

In [52] a time domain optimization is carried out to find control gains that minimize the eigenvalue based objective functions, thus ensuring stability. It is worth mentioning that microgrid modelling in [52] is carried out in a manner similar to [111]. The state-transition matrix of the entire microgrid is determined from individual subsystem models. With optimized parameters as the control gains and droop coefficients (constrained to maximum and minimum values) a particle swarm optimization is performed to minimize the eigenvalue based objective functions. The effect of electrical network connectivity and impedance characteristics on the voltage and frequency stability is discussed in [122] Subsequently stability conditions are presented based on linear dynamics models by making some assumptions on line impedance characteristics.

Improved transient stability offered by virtual impedance emulation is discussed in [46, 48]. The stability an angle droop-controlled inverter-based microgrid is discussed in [91, 118]. The stability issues arising from battery charge based droop control are discussed in [47]. Even though synchronverters are believed to provide a better understanding of inverter-interfaced microgrid from a stability point-of-view, no work so far has shown any results proving this belief. The stability of consensus based droop control for microgrids with constant power loads is discussed in [87]. The stability of communication-based droop-free control introduced in [103] is also discussed in the same paper. The works [8, 19, 87, 103, 121, 136] have used distributed communication between inverters for achieving various aims.

While most papers use linearization of the nonlinear dependencies to analyze the stability of microgrids, a few works have conducted a complete nonlinear analysis on droop controlled microgrids. In [135] the operation of inverters in parallel supplying constant power loads is described as a multi-rate Kuramoto model of coupled oscillators. The authors use a Kuramoto oscillator dynamics type formulation to analyze the stability of droop controlled inverters using the well established Kuramoto oscillator physics. Using the droop control dynamics coupled together with network admittance distribution, a non-linear analysis is carried out from which necessary and sufficient conditions for frequency synchronization were obtained. They have also determined the rate of frequency synchronization as a function of the network connectivity and system loading. Although they have only considered first order dynamics of sources and constant power loads, their work bridged the gap between the analysis based on droop coefficient design and that based on network power imbalance.

Conditions for synchronization of virtual oscillator control based inverters coupled through linear network impedances is presented in [64]. A main finding of this work is that the synchronization condition is independent of the number of oscillators present in

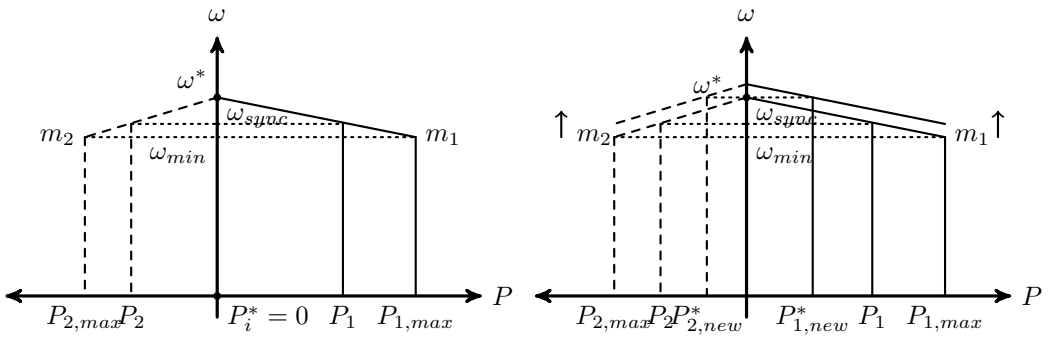

Figure 3.6: Secondary control: Nominal power is modified to achieve frequency synchronization between the microgrid and the grid.

the network. An array of hardware experiments is conducted to validate their proposals. According to the authors, the oscillator control restores the system to steady state operation even after a large disturbance, an issue which has not been addressed in droop control research. While works [35, 64] concentrate on single phase implementation, three phase operation is reported and validated using hardware in [63].

3.3.5 Control hierarchy in droop controlled AC microgrids

While traditional droop control provides an explicit communication independent architecture to control the microgrid, it primarily concentrates on local power sharing only. As we have seen in the microgrid definition, the operation of a microgrid also extends to providing an array of services like grid synchronization, etc. In conventional power systems in particular the control of energy sources is carried out in a hierarchical manner. The interactions between droop controlled inverters have been divided into three control levels [48, 49, 62]:

1. *Primary control* - power sharing and synchronization in island mode
2. *Secondary Control* - synchronization and grid transition
3. *Tertiary Control* - grid-connected operation

Since the previous sections have described the primary control in detail, this section concentrates on the secondary and tertiary control of microgrids. When the droop controlled microgrid needs to be reconnected to the grid, the frequency of the grid, ω_{grid} must be obtained at each inverter (through some form of communications). The synchronization to grid process needs to be accurate [45] to avoid large power transients in between the grid and the microgrid. The secondary control is made to operate on a slower time-scale so that its impact on the primary control dynamics are minimized.

3.3.5.1 Secondary control: an illustrative example

Once the inverter obtains the grid information, a secondary control action (as depicted by two small arrows in Figure 3.6 (right)) which essentially moves both the droop lines upward, is initiated. This control is carried out by changing the nominal power, P_i^* of each inverter to a new value, $P_{i,new}^*$ in such a way that the microgrid operates at the desired frequency while supplying the given load, thus, facilitating reconnection. This secondary control operation is, essentially, a phase locked loop system acting between the grid and each inverter in the microgrid. The droop curves are now modified to as shown in Figure 3.6. The voltage, V and the reactive power, Q changes are analogous, and therefore not discussed here.

3.3.6 Grid synchronization using communications

Centralized secondary control is proposed in [150], where a central controller calculates the frequency offset between the microgrid and the grid and then communicates the frequency offset value to each inverter. The inverters include the frequency offset in their droop equations and react accordingly. However the central controller provides a single point of failure which is undesirable. Mitigating this drawback, a distributed secondary control approach is introduced in [126] using sparse-communications. The effects of communication latencies on secondary control are also discussed in this work. The authors of [19], on the other hand, propose a multi-agent based secondary control wherein all the

constituent inverters act as agents in achieving a frequency consensus. The secondary control implicitly depends on the time-scale separation between primary control and grid-connection control, in which case a load change after "connect to grid" causes a steady state error in frequency restoration. Mitigating these drawbacks, [136, 137] propose a time-scale independent distributed-averaging proportional-integral (DAPI) controller to achieve secondary control. This structure uses minimum communication and is shown to be able to regulate the network frequency under large and rapid (but still slow compared to the bandwidth of the internal control loops) variations in load.

Secondary control is, reportedly, not required for angle droop techniques presented in [92, 94] since there is no deviation of system frequency from the nominal value. For synchronverters in [164], a dedicated synchronization (phase locked loop) unit is used. After making some necessary changes to the core of the synchronverter controller a self-synchronized system is proposed in [163]. Secondary control of the DC link based droop controller proposed in [147] is presented in [146].

The grid-connected operation of the microgrid is achieved through tertiary control [49]. The real power flow from and to the microgrid (or grid) can be controlled by changing the frequency of the microgrid. With grid (swing bus) in the configuration, this leads to a change in phase angle between the two entities in steady state. In general, a simple PI controller is implemented to achieve this tertiary control. The authors of [149] propose a control scheme based on the droop method which automatically adjusts the inverter parameters by using a grid-impedance estimation method. This estimation is based on analysing the voltage and current variations at the point of synchronization (POS) or PCC.

3.3.7 Other aspects of AC microgrids

High frequency switching in converters may results in harmonics in the network. These harmonics can arise from either the source side or the load side. Source side harmonics

arise as a result of improper DC component filtering, while load side harmonics arise from harmonic or non linear loads [155]. The elimination of DC side harmonics can be achieved through proper filter design. The potential to reduce THD through capacitive impedance emulation is shown in [161, 165]. Also, supplying these harmonic currents is necessary in the case of some harmonic loads. Virtual impedance emulation enhances harmonic current sharing (by adding a virtual harmonic resistance for the necessary harmonics) [46]. Harmonic load sharing via harmonic current injection is discussed in [20, 48]. Papers [26, 46, 144] discussed the inherent ability of droop control in non-linear load sharing.

In many countries, loads at the distribution level are connected single-phase. These single phase loads may cause phase current imbalance which in turn leads to unwanted zero sequence currents. Therefore maintaining the microgrid under these conditions needs a control mechanism which acts individually on each phase. The disadvantage of this method is that the individual control, without any co-ordination from each phase, might result in a higher overall imbalance. The maximum permissible levels of voltage unbalance are $\pm 2\%$ according to NEMA standards [110]. From [110] it can be seen that a negative sequence voltage component exists in unbalanced systems. In [117] an unbalance compensation technique is presented in which each inverter injects a negative sequence reactive power reducing the negative sequence voltage and consequently eliminating the unbalance in the system. The compensation effort is also shared between the sources in a distributed manner.

Energy balancing in the microgrid scenario is of primary importance since the scenario is highly energy limited. The flexibility that energy storage systems provide to the microgrid is effectively applied in [86] to autonomously achieve supply-and-demand balance. The energy storage system draws power when the frequency (droop controlled) of the microgrid is greater than a threshold limit. Between the threshold frequency and allowable minimum frequency, the system behaves as a simple droop controlled inverter.

It has to be mentioned that the threshold frequency levels are known from the power measurements assuming perfectly nominal frequencies. It is determined in [38] that an effective inverter based control design should depend on both regulation and the DC source characteristics.

3.3.8 DC microgrids

As discussed earlier, microgrids offer exciting opportunities for electrical networks that have a high penetration of renewable energy generation. The majority of the renewable energy systems produce their energy in DC form making them most attractive and directly compatible to DC microgrid systems. The parallel operation of DC sources in a microgrid has also been a topic of great interest in recent years. As with AC microgrids, power sharing accuracy and voltage stability are recognized as the main issues in DC microgrids.

A DC microgrid operation based on a central controller is well addressed in the literature [50]. Master-slave DC microgrid systems and their stability are discussed in [51]. It is apparent that a central controller based on a master-slave design provides a single point-of-failure. To alleviate the single point of failure, a parallel operation scheme for DC sources using droop control was proposed in [88]. Similar to reactive power - voltage droop ($Q - V$) in high voltage (HV) AC microgrids, power sharing in droop controlled DC microgrids depends on the output impedance ratio between the sources and the loads [56]. While proper impedance design can alleviate a majority of the power sharing issues, such a design becomes increasingly difficult for large and complex networks. For this reason many communication based techniques are proposed in the literature to address the power sharing mismatch, for example see [97].

3.4 Research focus of this thesis

This section reviews all the literature that addresses the topics covered as research contributions in this thesis. Continuing from the state of the art exploration, certain research gaps are identified here and listed as research questions.

3.4.1 Part 1: Addressing energy deficits using storage

Storage technologies play a tremendously important role in increasing the rate of renewable energy uptake for a number of reasons such as the intermittent nature of renewable energy as well as their unpredictability. With increasing demand on electricity networks, network operators and consumers are now finding many benefits in using storage and photovoltaic systems in combination. The majority of recent literature are focused on demand control for providing better power quality and voltage stability to the networks [33, 72, 84, 95, 108]. A further important research area is the operation of energy storage (at the distribution network level [2] and the household level [4, 100]) for economic gain, by exploiting temporal arbitrage made possible by a time-varying price signal or tariff structure. The impact of rising electricity tariffs and falling feed-in tariffs is considered in the lifetime evaluation of solar systems linked with storage [100]. In [105], the authors addressed the problem of operating distributed storage systems of a given size to satisfy some network constraints. The main contribution of the paper was utilizing the time-of-use price arbitrage to reduce the operational cost of batteries.

As seen in the background chapters, master-slave microgrids are a good alternative in situations where master-less microgrids are difficult to implement [23]. In master-slave microgrids, energy dispatch has to be intelligently controlled to improve the overall performance and longevity, and at the same time make the microgrid robust to energy deficits. Researchers have considered the battery sizing problems from various perspectives. It is known that sizing and optimal operation of batteries is subject to the stochastic nature of the renewable energy supply. This fact was considered in [27] where

the authors applied a mixed integer linear programming approach to find the optimal battery size that can alleviate the power imbalance in the network under forecast uncertainties. Mismatch in the response times between synchronous and inverter-interfaced generation has also been considered in sizing batteries [156]. A survey of the battery types was conducted and a subsequent techno-economic viability of batteries was performed in [115].

Many papers in literature addressed the energy storage system sizing problem for microgrids from an energy/power balance perspective, [70] for example. A recent paper [6] proposed a framework that can be used in sizing energy storage systems in a distributed manner within a microgrid. Optimal battery sizing for microgrid data-centres considering financial as well as environmental constraints is discussed in [143]. Constraints on microgrid frequency deviation were used in obtaining storage decisions in [157]. Sizing for long term microgrid operation has been addressed in [5]. Unit commitment based optimal battery storage sizing for wind power based microgrids under forecast errors using particle swarm optimization has been discussed in [71].

Sizing and proliferation of storage systems has potential benefits not only in improving the economics of a microgrid but also in achieving better network quality. Distributed voltage control, power balancing and avoiding reverse power flow are some key criteria in operating a master-slave microgrid. An integrated approach that solves the battery sizing problem in conjunction with voltage control, power balance and operational cost minimization is not available, to the best of our knowledge.

3.4.2 Part 2: Controlling parallel converter based generation under mismatches

3.4.2.1 Modelling master-less sources

Moving on to primary control of sources in a master-less microgrid. Based on the background literature, we use the following voltage source inverter model in the remainder of this thesis. Any sinusoidal voltage source is a simplified representation of a DC source interfaced to the AC network via a power electronic inverter interface. Each inverter has a DC energy source such as a battery or photovoltaic system. Assuming that there is sufficient energy in the DC source and its terminal voltage is maintained well within inverter limits, the DC and AC sides of the inverter can be decoupled and each inverter can be approximately modelled as a voltage source behind an impedance [155]. This assumption is preceded by an implicit assumption that the switching frequency of the inverter is much faster than any other control loops within the power electronics interface. Since, typical inverter switching frequencies are of the order of a tens of kHz and the control loops within are much slower, dynamics of switching average out over the time interval under consideration [69]. In such a scenario, the output voltage of the inverter $v_i(t)$ can then be represented by

$$v_i(t) = d_i V_{i,DC} \cos\left(\omega t + \delta_i\right), \tag{3.12}$$

where t is the time, d_i is the modulating signal, $V_{i,DC}$ is the voltage across the DC source, ω is the inverter output frequency and δ_i is its phase angle. Typically the modulation depth d_i is chosen between 0 and 1 to preserve the sinusoidal shape of the output. From (3.12) it can be seen that any changes in d_i or ω or δ_i will reflect changes in $v_i(t)$.

3.4.2.2 Clock drifts

In this thesis, we particularly focus on the consequences of clock accuracy, and the impact this has on implementing a global frequency across the microgrid. The majority of the

literature generally assumes that inverters can maintain a particular nominal frequency, yet this nominal / operating frequency can fluctuate. As there are no synchronous machines, there is a compelling case to considering the consequences of clock drift. In practice, as a consequence of clock drift, an inaccuracy of 0.1% in frequency is quite typical in commercial inverters [37, 112, 123] (see also Table 3.2). In a grid-connected scenario these inaccuracies may lead to some fluctuations in power factor. But, in autonomous microgrid operations with inverters operating in parallel these drifted clocks have much larger implications. In some cases these small fluctuations will hamper the system performance and may affect the system's lifetime.

To facilitate such an analysis, we denote the voltage at each inverter in terms of a common reference time t and represent the local time t_i at the ith inverter with respect to the reference time t [120]:

$$t_i = t\,(1 + \epsilon_i)\,, \tag{3.13}$$

where ϵ_i is the drift of the local clock with respect to the reference clock. Here we consider a time invariant drift. The stability results will allow us to infer robustness with respect to slow time varying drifts. When there is no master clock in the system a drift in local clocks is natural.

From the above definitions the ith inverter based source can be modelled in terms of the reference time t (with a slight abuse of notation) as

$$v_i(t) = V_i \cos(\omega_i t + \delta_i), \tag{3.14}$$

where $V_i = d_i V_{i,DC}$ is the voltage amplitude, $\omega_i = \omega + \eta_i$ with $\eta_i = \epsilon_i \times \omega$ is the frequency generated by inverter i and δ_i being the phase angle.

Using commonly reported values for the clock drift, ϵ_i a frequency drift in the order of 0.03 Hz (for reference frequencies around 50 or 60 Hz) is to be expected, as seen in

Table 3.2: Drifts in commercial inverters.

Reference	$\lvert\eta\rvert$(Hz)	γ
[123]	0.05	1 ± 0.001
[37]	0.025	1 ± 0.0005
[112]	0.05	1 ± 0.001
[90]	0.06	1 ± 0.001
[159]	0.025	1 ± 0.0005

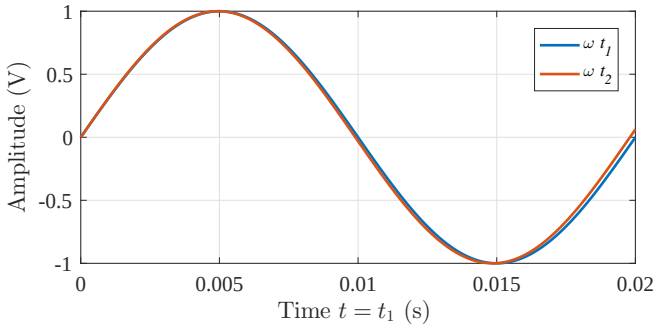

Figure 3.7: Time drifts, $\epsilon_1 = 0$ and $\epsilon_2 = 0.01$.

Table 3.2. The table lists $\eta = \epsilon\omega$ as well as the corresponding per unit time scale variable $\gamma = 1/(1+\epsilon)$. The physical effect of this drift is shown in Figure 3.7 with a two voltage source example. It can be clearly seen that inverter 2 appears to produce a higher frequency output when viewed from the perspective of inverter 1 despite implementing the same frequency, ω.

Under isolated operation, the plug and play capability of sources and the load-independent stability of the microgrid are very important. Broadly, our work falls into the category of methods to improve the modularity of inverter based sources in a microgrid. Although there is an extensive literature available for microgrids, very little focus

is made on understanding critical criteria like manufacture and design induced stability issues. When the system stability / flexibility is at risk it is crucial not to underestimate these kind of mismatches. In this work, we present a method which can increase the stability margin and make power sharing more robust in microgrid systems with minimal changes to their design topology.

3.4.2.3 Frequency droop and mismatches

As seen in Section 3.3.4 and 3.3.1, the majority of the work in inverter interfaced microgrids based on droop control focuses on the stability and efficiency of these systems under certain assumptions. Papers [131, 162] comment on the significance of computational delays, numerical errors and parameter uncertainties and show their effect on power sharing between systems and overall stability. A simulation analysis in [131] shows the effect of computational delays on microgrid stability. In [162] a qualitative analysis was performed to demonstrate the contribution of these component mismatches to inaccuracy in power sharing (specifically those arising from voltage, where $(P-V)$ droops were used for a LV network). A robust voltage controller was then proposed to mitigate these effects. The authors make no attempt to comprehend the effects of the parameter mismatches on the stability of the system, particularly when the mismatches are in the form of frequency (or, equivalently, angle) errors. Some authors have acknowledged the issues arising from these mismatches but have not discussed them in extensive detail [85, 148, 162]. While it is possible to have frequency related mismatches arising from various scenarios like crystal inaccuracies or inaccurate pre-synchronization of inverter interconnection [148], the stable frequency assumption has pervaded the research communities until recently. Stability issues arising from clock uncertainties have been looked into in more detail by [120]. However, their conservative assumptions on line impedances and small clock drifts might not always hold. It has also been shown in a recent work [75] that distributed averaging based proportional integral controllers[133] that are used in secondary control cannot guarantee proper power sharing in the presence of clock drifts.

3.4.2.4 Angle droop and mismatches

As already seen, one well known decentralized control technique is the angle droop control introduced in [92]. Implemented only on real power (P_i - for highly inductive networks), this scheme is motivated by the well-known fact that small angle differences will cause a change in the power sharing between the sources. Therefore, each inverter i is controlled to change its phase angle, δ_i, according to its real power output, P_i. Depending on the network characteristics, the angle droop control is also modified to control the real or reactive power flow in microgrid networks [94]. Although their implementation is supposedly harder than frequency droop control, angle droop controlled inverter based systems provide better stability margins [91, 118] owing to their inherent reliance on frequency accuracy. Unlike frequency droop control [26], angle droop control produces a zero steady state frequency error [92].

It has been shown that power sharing between angle-droop controlled inverters is subject to the impedance distribution between them [94]. This is owing to the fact that impedance distribution introduces a phase angle shift between inverters which is not taken into consideration when designing the droop coefficients. The power sharing inaccuracy that results from disproportionate impedance distribution in angle droop controlled microgrids is analogous to reactive power sharing in $(Q-V)$ droop controlled systems (as seen in [126] and [121]).

3.5 Specific research questions

Here, we re-iterate the research questions posed in the beginning of this thesis.

Part 1: Addressing energy deficits using storage

- *What is a method to model a microgrid network that is based on a master-slave topology?*
- *What is a way to size the batteries at individual households within a*

master-slave microgrid and operate them to satisfy realistic physical/ financial constraints?

- *How to address uncertainty? In other words, how to improve the performance of the proposed method under uncertain load and generation forecasts?*

Part 2: Controlling parallel converter based generation under mismatches

- *How does clock accuracy/drifts affect the stability and power sharing of both angle and frequency droop controlled systems?*
- *What is a way to alleviate the effects of clock drifts on power sharing and stability for any arbitrary topology in a droop controlled microgrid?*
- *What assumptions should be made in solving this problem of clock drift effect and are these realistic?*
- *What are the conditions for achieving stability and power sharing for the methods introduced?*
- *How crucial is the output impedance design in angle droop controlled converter interfaced microgrids and what effect does impedance mismatch have on power sharing?*
- *How can control design overcome the negative effect impedance mismatch has on power sharing?*

✧✧✧

Part III

ENERGY STORAGE SYSTEM DESIGN

4

Optimally Sizing Batteries for a Microgrid

4.1 Introduction

IN this chapter we address the problem of how to size (and also to position, as size will include the option of having no battery at a location) and operate household batteries in a master-slave microgrid. The problem will be formulated in such a way to ensure that the power quality, and the network constraints (cable current limits, voltage limits) are taken into account. Simultaneously, we formulate the problem in a way that reduces both economic cost of running the network as well as the installation costs.

4.1.1 Modelling sources and loads

An example microgrid network with three houses, acting as slaves, and a master generator at the beginning of the radial line is given in Figure 4.1. The kind of network adopted for analysis accommodates grid-connected households that have roof-top solar systems and are intending to go off-grid with the support of a master source. In terms of co-ordination and battery operation this method can be used by a third-party network aggregator that finds mutual benefit in reducing energy demand. One example for this

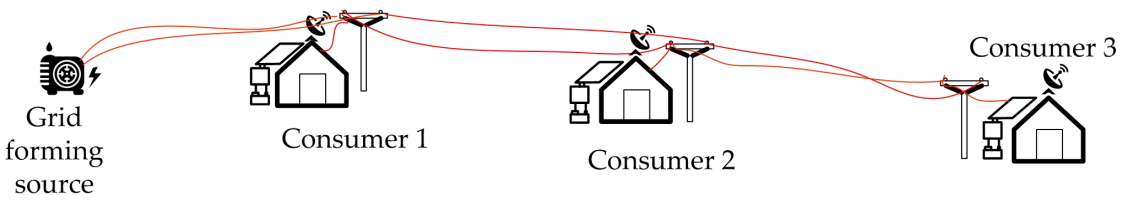

Figure 4.1: An example of a microgrid.

kind of scenario is that of using the communication-based master-slave system presented in [166]. Another example is a decentralized approach where the slaves unite to decide on battery sizing and operation so that they can reduce the energy consumption from an external master.

- *Grid forming source:* The grid forming source is ideally a voltage source that is capable of supplying the entire microgrid in scenarios where local generation provides no output. This voltage source can be based on an inertial generator or converter based generation [119]. This type of voltage source will be either DC or AC depending on the network type.

- *Household loads:* In general, houses contain a variety of loads and they can be accurately represented as impedances. Consequently, an ideal model would formulate houses as impedances varying over time. On the other hand, data loggers at distribution substations measure the amount of power consumed at a transformer level, meaning impedance information for each house is generally unknown. In such cases, it is often assumed that the houses are current-sinks varying over time. This assumption relaxes the condition that the consumption at a household depends on the local voltage pattern. Another advantage to this approach is that the power at the transformer can be averaged (divided by the number of houses) to find the current demand at each house. Therefore, throughout this chapter the household loads are considered as current loads varying from one interval to the next. Observe that, in principle the consumer can be any point in a grid where energy is required.

- *Roof-top photovoltaic systems*: we consider a conventional PV system that is implementing a phase locked loop (PLL) based grid connection and the power output of this system is driven by the maximum power point tracking (MPPT) algorithm. We assume a unity power factor supply from the PV system. The power can then be expressed in direct current (DC) terms as supplied to a system at a given voltage. Note that the PV system produces a constant power output for a given insolation and does not depend on the voltage. For example, if the voltage at a house goes below the nominal voltage the current output will increase to maintain a constant power, for a given insolation. To avoid non-linear constraints, we will consider the roof-top PV systems as voltage-independent current sources, throughout this work.

- *Batteries*: These can act as sources or sinks. In an ideal scenario, batteries act as constant power loads or generators with current-limited capability from their respective DC-AC converters. Similar to the modelling carried out in the earlier sections, we can assume that batteries will be either current sources or current sinks for a given time period and are voltage-independent. The amount of current flowing in and out of the battery is constrained by the charge capacity and charging current limitations. These will be discussed in detail in the later sections.

4.1.2 Network model and constraints

We divide the finite time interval of interest for the design into T discrete time intervals each of length τ. So the problem formulation now becomes discrete and has time entries from the set $\mathbf{T} = \{\tau, 2\tau, \ldots, T\tau\}$ where τ is the length of each time slot.

We consider a radial master-slave microgrid network as shown in Figure 4.2. This a very practical network configuration on the distribution level [33] and any future reference to the network corresponds to a network of similar topology where the houses are connected to a voltage source in a single line. However, our analysis can be extended to a branched network with very little modification. In Figure 4.2, the houses are indexed

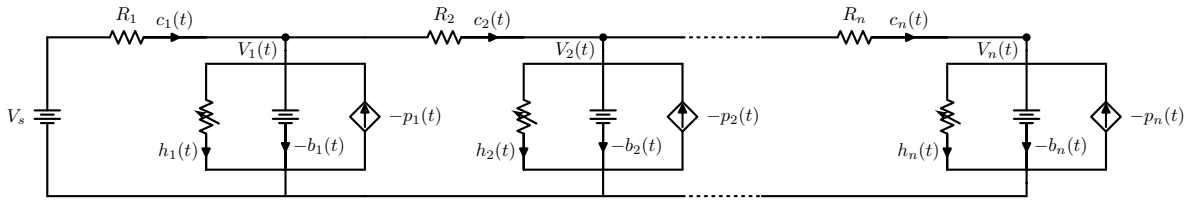

Figure 4.2: A radial resistive low voltage distribution network model. Each house in the network is equipped with a photovoltaic system and a battery storage system.

by the set $\mathbf{N} = \{1, 2, 3 \ldots n\}$. The number assigned to each house is in an ascending order which places house 1 closest to the master source, V_s, and the house n farthest away.

According to [33], distribution networks generally have a high cable resistance to reactance (R/X) ratio. Based on this, we can reduce the full complex AC network equations to DC equations, thereby, simplifying the analysis. Also assuming unity power factor loads and sources makes our method directly applicable to DC as well as AC systems. This justifies the DC-type network and constraint description in the subsequent sections. Our analysis is based on a quasi steady-state assumption, as we are only interested in energy dispatch, not transient stability.

Each house, x in the network has a local voltage V_x and is potentially fitted with a battery together with a rooftop photovoltaic system. The current flowing from the network into a load at house x at time t is $h_x(t)$, where $x \in \mathbf{N}$ and $t \in \mathbf{T}$. As mentioned in Section 4.1, the household load is modelled as a current sink, which reduces the non-linear dependence of current on local voltage and converts the load into a linear independent term.

The current flowing through the cable (of resistance R_x) between house $x-1$ and x is given by $c_x(t)$. The battery current at house x at time t is $b_x(t)$. Since, the current flow through the battery is bidirectional, we define charging as the period when the current is flowing into the battery i.e., $b_x(t) > 0$ and discharging when $b_x(t) < 0$.

The photovoltaic current at a house x at time t is given by $p_x(t)$. We assume all currents are constants during a time interval, τ. In Figure 4.2 the household load is represented by a variable resistor and the PV current source is represented by a dependent current source to signify the variance in loads and the dependency on solar irradiance, etc., respectively.

4.1.3 Voltage Constraints

In general, it is the responsibility of the network operator (or consumer in the decentralized scenario) to maintain the voltage between specified levels at every node (house or grid forming source) of the network. In Australia this should be between 6% below (0.94 p.u) and 10% above (1.1 p.u) the nominal 230V rms (root mean square) value [15]. Violating the voltage limits could adversely affect the operation and life-span of household loads and network infrastructure. From the radial model shown in Figure 4.2 and the assumptions made in the previous sections, the voltage at the x^{th} house at time t for a stable voltage source can be written as :

$$V_x(t) = V_s(t) - \sum_{i=1}^{x} R_i \left(\sum_{j=i}^{n} h_j(t) + b_j(t) + p_j(t) \right),$$

where $x \in \mathbf{N}$ and $t \in \mathbf{T}$. The voltage constraints can be written as,

$$V_{min} \leq V_x(t) \leq V_{max},$$

where the suffixes V_{min} and V_{max} represent minimum and maximum permissible voltage levels.

4.1.4 Nominal Current Rating Constraints

The losses on cable sections are directly proportional to the amount of current flowing through them squared. Prolonged heat losses can cause permanent physical damage to the cables. To avoid physical damage to the cables the amount of current flowing through each cable segment has to be limited. From the system model given in Figure

4.2, in a given time interval the amount of current flowing through the cable prior to house x can be written as,

$$c_x = h_x + b_x + p_x + c_{x+1}$$

The current constraints can be written as,

$$-c_{max} \leq c_x(t) \leq c_{max},$$

where $x \in \mathbf{N}$ and $t \in \mathbf{T}$, c_{min} c_{max} is the maximum cable currents that can flow through the cables without causing any significant physical damage to them.

4.1.5 Constraints on Batteries

4.1.5.1 Fixed capacity

Batteries cannot charge or discharge beyond their capacity ratings. For this reason it is required to impose a capacity constraint on the battery at each house. The absolute state of charge of each battery at a specified time t', $C_x(t')$, depends on the $C_x(t'-1)$ of the battery and the current flowing through the battery during the time interval $(t'-1)$ and (t'). This can be written as shown in (4.1).

$$C_x(t') = \tau \sum_{t=1}^{t'} b_x(t) + C_x(0), \tag{4.1}$$

where $x \in \mathbf{N}$, $t, t' \in \mathbf{T}$, $C_x(0)$ represents an initial state of charge and τ is the length of the time slot. The associated constraint can be written as,

$$C_{min,x} \leq \tau \sum_{t=1}^{t'} b_x(t) + C_x(0) \leq C_{max,x},$$

where C_{min} and C_{max} are the minimum and maximum charge capacity the battery can hold. As seen in the earlier scenario, we can replace the global capacity constraints with local capacity constraints which will satisfy the above inequality.

It is worth mentioning that the charge capacity is assumed to be independent of the battery voltage and cycling regimes, which otherwise, make the problem complex and very hard to solve.

4.1.5.2 Optimal sizing

We can find the optimal battery size by formulating the optimization problem as a combined (scaled) cost of 1) operation of battery and 2) the optimum size of battery at each house. Let Γ_x denote the capacity of the battery [Ah] (typically a discrete value) at each house. The "Ah" denotes ampere hour units as subsequently used in Table 4.2. We can write the battery charge capacity constraints as:

$$C_{min,x} \leq \tau \sum_{t=1}^{t'} b_x(t) + C_x(0) \leq \Gamma_x \leq C_{max,x} \tag{4.2}$$

where $x \in \mathbf{N}$, $t' \in \mathbf{T}$ and $\Gamma_x \in \{1, \cdots, C_{max,x}\}$. Here we assumed that the discrete valued battery sizes as integers in [Ah] capacity. This form of normalization allows us linearize the problem and also allows to encapsulate battery capacities over a wide range as integer values, for example, 230 Wh as 1 Ah at 230V nominal voltage which gives four choices within a kWh capacity. We acknowledge that the optimization method remains sub-optimal for some arbitrary choice of battery sizes (see Remark 4.2.1). If the battery sizes are available in sizes that are varying in linear steps, normalizing the entire optimization problem to result in integer battery sizes remains an option. Non-linear profiles in battery sizes, however, cannot be accommodated in the proposed method.

4.1.5.3 Charge rating constraint

In general, batteries have specified charging and discharging rates. Exceeding these ratings is not always possible and, if it happens, might reduce the operational lifetime of the battery. These limits are generally imposed on the current flow of the battery (at the rated voltage of the battery converter). Therefore, it is essential to impose bounds on the amount of current that can flow to or from the battery. Let $b_{min,x}$ and $b_{max,}$ be the minimum and maximum input and output current ratings of the battery at house x, respectively. This can be enforced by a battery current constraint which is written as,

$$b_{min} \leq b_x(t) \leq b_{max},$$

where $x \in \mathbf{N}$ and $t \in \mathbf{T}$. The majority of the time the battery current limitations are proportional to its size and charging capacity. This is depicted by the constraint:

$$\delta_{min}\Gamma_x \leq b_x(t) \leq \delta_{max}\Gamma_x,$$

where δ_{min} and δ_{max} are the minimum and maximum charge rating factors, respectively.

4.2 Optimization Problem

In this section we define our optimization problem, which is to minimize the cost of importing electricity, $J(b_x, \Gamma_x)$, from the grid forming source while satisfying the network and battery constraints. Assuming that the users have unrestricted communications, unrestricted control over the batteries and reasonable forecasts of load, PV and prices for a given time horizon $\mathbf{T}$ we formulate the optimization problem as shown in equation (4.3). In (4.3), we define the vector of battery currents, $\boldsymbol{b} := [b_1(\tau), \ldots, b_1(T\tau), \ldots, b_n(T\tau)]$, the vector of battery sizing decisions $\boldsymbol{\Gamma} := [\Gamma_1, \ldots, \Gamma_n]$. Observe that, sizing based on reasonable forecasts will avoid significant undersizing or oversizing. However, if the optimization is used to obtain short term charging and discharging decisions for installed batteries, optimal operation can only be guaranteed by short yet precise forecasts.

In most microgrid scenarios, the grid forming source that is supplying energy has restricted energy feed-in for various reasons. The optimization problem can be formulated in such a way that the overall self consumption is maximized and the batteries are sized appropriately for the same application. Table 4.1 provides the description of all the variables used in the optimization problem. The formulation results in a MILP with integer battery sizing decisions.

$$\min_{\boldsymbol{b}\in\mathbf{R}^{nT},\boldsymbol{\Gamma}\in\mathbf{Z}^n} J(\boldsymbol{b},\boldsymbol{\Gamma}) = \tau V_s \sum_{t=\tau}^{T\tau} P_i(t) \sum_{j=1}^{n} (h_j(t) + b_j(t) + p_j(t)) + \gamma \sum_{x=1}^{n} \Gamma_x + \beta \qquad (4.3)$$

subject to

$$\begin{aligned} V_{min} \leq V_s(t) - \sum_{i=1}^{x} R_i \left(\sum_{j=i}^{n} b_j(t) + h_j(t) + p_j(t) \right) \leq V_{max} \\ -c_{max} \leq \sum_{j=x\neq 1}^{n} (b_j(t) + h_j(t) + p_j(t)) \leq c_{max} \\ C_{min,x} \leq \tau \sum_{t=1}^{t'} b_x(t) + C_x(0) \leq \Gamma_x \leq C_{max,x} \\ \delta_{min}\Gamma_x \leq b_x(t) \leq \delta_{max}\Gamma_x \end{aligned} \tag{4.4}$$

and

$$0 \leq \sum_{j=1}^{n} (h_j(t) + b_j(t) + p_j(t)) \leq c_{max} \tag{4.5}$$

if the master source has energy feed-in restrictions.

Remark 4.2.1. *The relaxed version of* (4.3) *is a LP problem where battery sizes are no longer integer multiples of a given size. Solving such a problem, of course, will result in non-integer battery sizes which should eventually be rounded to the nearest available (integer or discrete) battery capacity. However, in doing so the battery distribution and temporal operation might no longer be optimal nor feasible. For that reason, we have formulated the problem to be a MILP instead of a linear program (LP).*

Remark 4.2.2. *In* (4.3) β *is a daily charge that should be paid by the customers for accessing the network and maintaining voltage. Although* β *is an uncontrollable overhead, for example, from the contract between the grid forming source and the customers, it is added to the optimization problem to indicate that the grid forming source is always being paid for supplying and maintaining the network infrastructure and maintaining the voltage that is required for the proper functioning of the network.*

Remark 4.2.3. *Since there are no assumptions made on controllability and deferability of household loads, the practical realization of this optimization procedure is achievable with minimum changes to current infrastructure. With the advent of technologies like*

communication ready smart energy meters [39] and battery inverters[139], the proposed scheme is readily implementable.

Table 4.1: Description of parameters used in (4.3).

Parameter	**Description (units)**
x	index of house, $x \in \mathbf{N}$
t	index of time, $t \in \mathbf{T}$
τ	length of time slot (hr)
$V_x(t)$	voltage at a house $x \in \mathbf{N}$ (V) at time t
V_s	voltage at the grid forming source (V)
R_x	resistance of the cable between house $(x-1)$ and house (x) (Ω)
$P_e(t)/P_i(t)$	price of electricity exported/imported (\$/kWh) at time t
$c_x(t)$	current through the cable segment between house $x-1$ and house x (A) at time t
$b_x(t)$	current through the battery at house x (A) at time t
$h_x(t)$	current through the load at house x to the ground (A) at time t
$p_x(t)$	current from the PV system (could go to battery, house, or cable) at house x (A) at time t
$C_x(t)$	charge in the battery at house x (Ah) at time t
γ	daily proportion of capital investment on batteries considering the lifetime/ payback period (\$/Ah.day)
$\mathbf{\Gamma}_x$	Maximum battery capacity at house x (Ah)
δ	charge rating factor (1/hr)

4.3 Simulations and discussion

4.3.1 Case 1: Optimization under perfect forecasts

In this case, we consider the following optimization problem: the network and battery sizing parameters used in this case are given in Table 4.2. The demand current of house 1, $h_1(t)$ (shown in Figure 4.3 (bottom)) is populated using data averaged on a monthly basis from [16]. The demand data for the remaining houses is different but obtained from the same reference. Houses 1, 2 and 5 have a 1.5 kW roof-top PV. The roof-top PV output data used here is obtained from [100]. The average data is extrapolated to 12 days by adding white Gaussian noise (with signal to noise ratio (SNR) = 20 when $p(t) \neq 0$) to account for variability during the day. Variability during the night is suppressed by simply adding Gaussian noise only when $p(t) < 0$. This shown in Figure 4.3 (top). The generation at each house equipped with PV is made identical to capture closeness between houses and is scaled to 1.5 kW capacity (from 2.5 in [100]) to ensure that the system is not overly constrained. For the price, we use a two part time-of-use tariff. Each kWh imported from the master source is priced at \$0.30 between 3 pm to 9

Table 4.2: Numerical values for parameter used in the example case study.

Parameter	**Value**
n	6
T	24×12 (hours × days)
τ	1 hours
R_x	1/30 Ω $\forall x \in \mathbf{N}$
C_{min}, C_{max}, $C_x(0)$	0, 11, 0 Ah $\forall x \in \mathbf{N}$
V_s,V_{max},V_{min}	230, 253, 216 V
c_{max}	120 A
γ (1 year payback)	0.2 \$/Ah.day
δ_{min},δ_{max}	-1, 1 (1/hr)

pm and \$0.20 during other times, daily.

The voltage and cable current profiles of each house, when the batteries are not installed, are shown in Figure 4.4. It can be seen that the voltage profiles follow the aggregate network demand profile. As observed from the figure, drops in voltage coincide with times where the aggregate demand is higher that the overall PV generation. There are also instances where a small amount of energy is fed into the master source. These times are depicted by reverse current flow as seen on the first cable section (thick blue line in Figure 4.4 (bottom)). It is important to note that master sources may have restricted energy feed-in. So, in such cases this microgrid cannot be sustained in the current form unless the PV output is wasted.

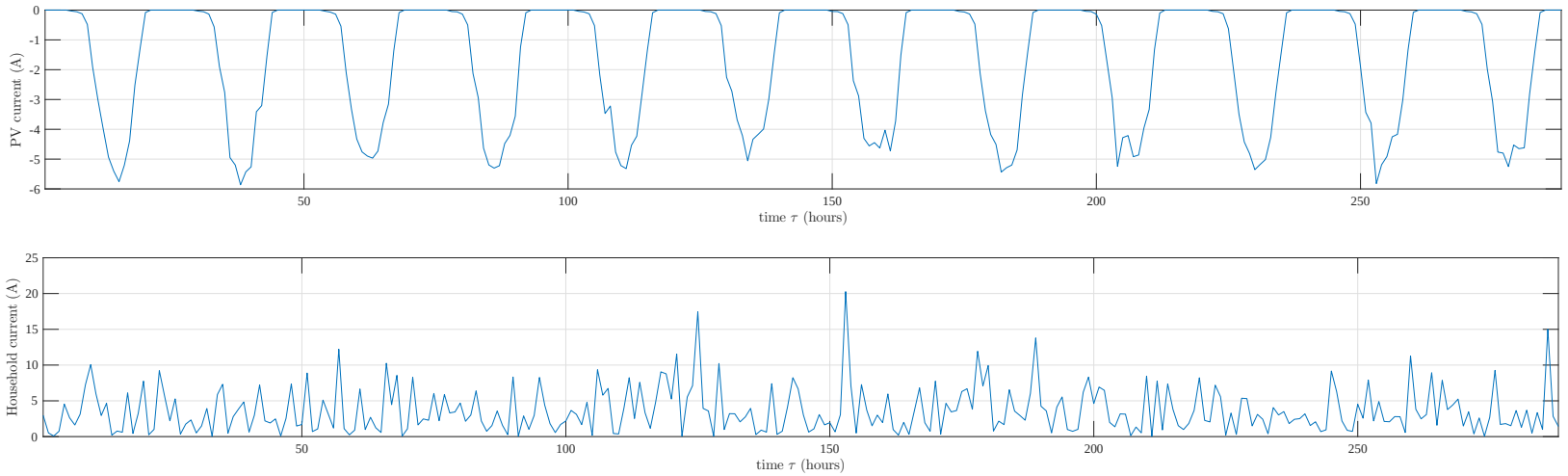

Figure 4.3: Graphs showing (top) output of a 1.5 kW roof-top PV system obtained by adding white Gaussian noise on an hourly basis, and (bottom) household electricity demand in terms of load current $h_1(t)$ for a house in Victoria over a period of 12 days ($12 \times 24 = 288$ hours).

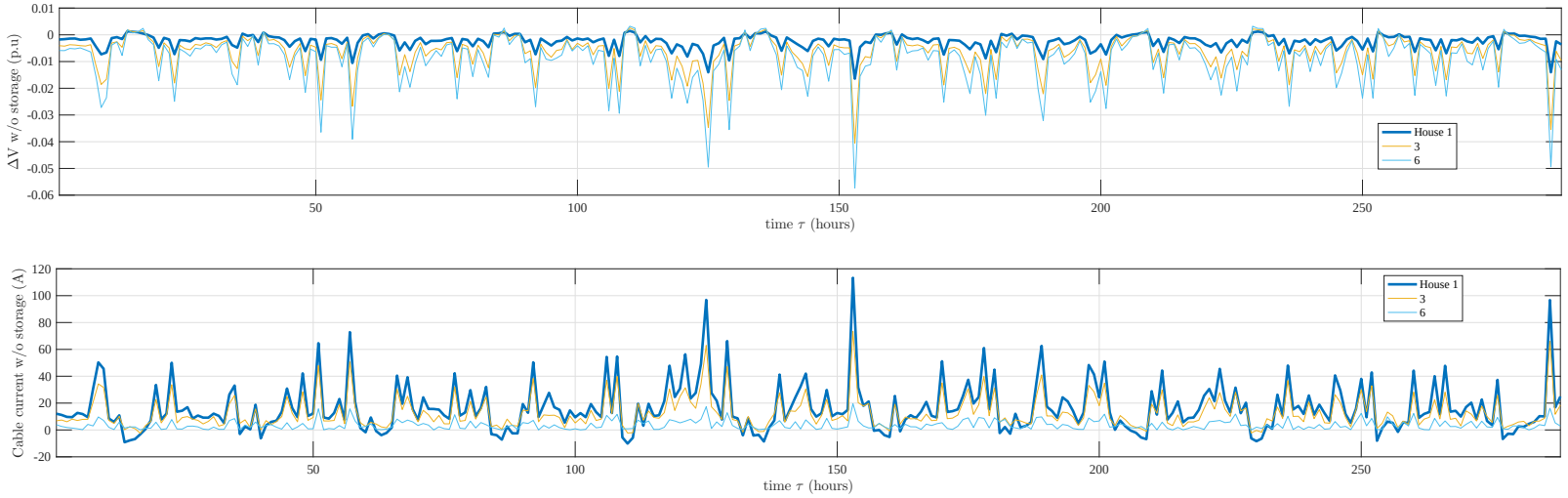

Figure 4.4: Voltage (top) and cable current (bottom) profiles at houses 1,3 and 6 in Case 1 when there are no batteries installed in the microgrid over a period of 12 days ($12 \times 24 = 288$ hours).

Table 4.3: Battery capacities to be installed at each house according to the proposed algorithm under perfect forecasts (Case 1).

House No.	1	2	3	4	5	6
Battery Capacity (Ah)	11	6	0	7	0	3

Considering the same parameters (shown in Table 4.2) we solved the MILP (4.3) with constraints (4.4) and (4.5) in MATLAB. These results are presented in Figures 4.5, 4.6 and 4.7. According to the solution, suitable storage system positions and sizes are shown in Table 4.3. From Figure 4.5 (top) it can be seen that the voltage profile looks different from earlier scenario given that there is battery charging and discharging involved. The major result here is that the cable current prior to house 1, c_1 is not less than zero (or the change in voltage, ΔV_1 is never going above 0 p.u) indicating zero energy feed-in as shown in Figure 4.5 (bottom). The charging and discharging profiles of the batteries are shown in 4.7. The batteries at houses 1 and 2 act as (virtual) loads when there is supposed to be current injection back into the master source and discharges during energy deficits. The main role of the remaining batteries in this case is to satisfy their local constraints during battery operation. The battery profiles (as shown in Figure 4.7) will ensure that the network and battery constraints are satisfied.

The optimization problem is solved to output a battery size that ensures local constraints are not violated by charging or discharging. A histogram distribution of the cable currents and voltages at each house is shown in Figure 4.6. It can be clearly seen that the voltage on house 1, V_1 fluctuates between 1.01 p.u and 0.985 p.u when the batteries are not installed. Similar to the voltage deviations, the cable currents are both positive and negative at this house when there is no storage. When the batteries are installed, the lowest current on cable prior to house 1 is zero. The voltage deviation on house 1 is restricted as well. It is also seen that the voltage at any house remains within the limits ($\Delta V_{x>1}$ between 0.1 p.u and -0.06 p.u) when the batteries are installed. As we

have also included prices in the optimization algorithm, in most cases, the current drawn from the master source minimized. However, if it has to be drawn from the master, it is mostly done during the off-peak periods to accommodate loads in th peak periods. In this manner the overall benefit is increased substantially.

For this network, the benefit can be calculated based on the amount of PV energy wasted when the batteries are absent. The cost of installing batteries for the operational period is approximately \$65 and is calculated using the value γ listed in 4.2. The net profit of installing batteries is \$6 for this day period not taking into consideration that the batteries are also acting as energy buffers to sustain the microgrid. Profit is low mainly owing to the quick payback period we have chosen. This increases to \$33 when the wasted PV energy is also considered. The cost of PV energy wasted is calculated using the daily energy price curves. For overly constrained networks or under-sized microgrids, using the proposed battery sizing algorithm to estimate suitable battery sizes can achieve grid independence (as an energy source). Since this case study is based perfect forecasts the decisions made can become sub-optimal for some cases.

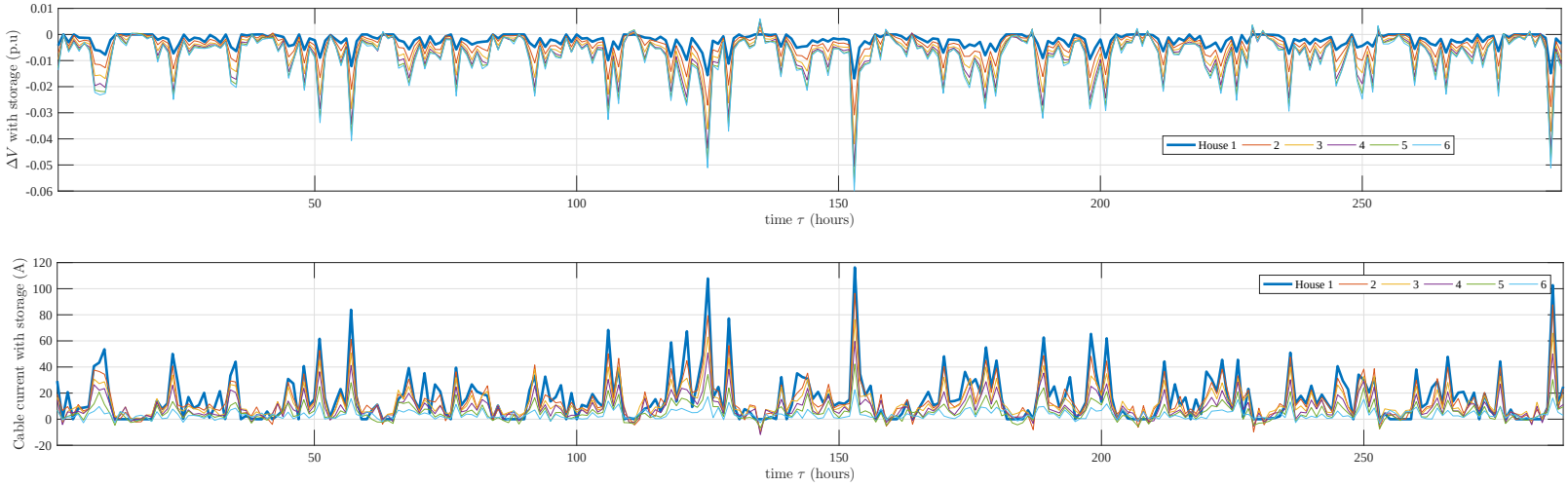

Figure 4.5: Voltage (top) and cable current (bottom) profiles at each house when batteries are installed over a period of 12 days ($12 \times 24 = 288$ hours).

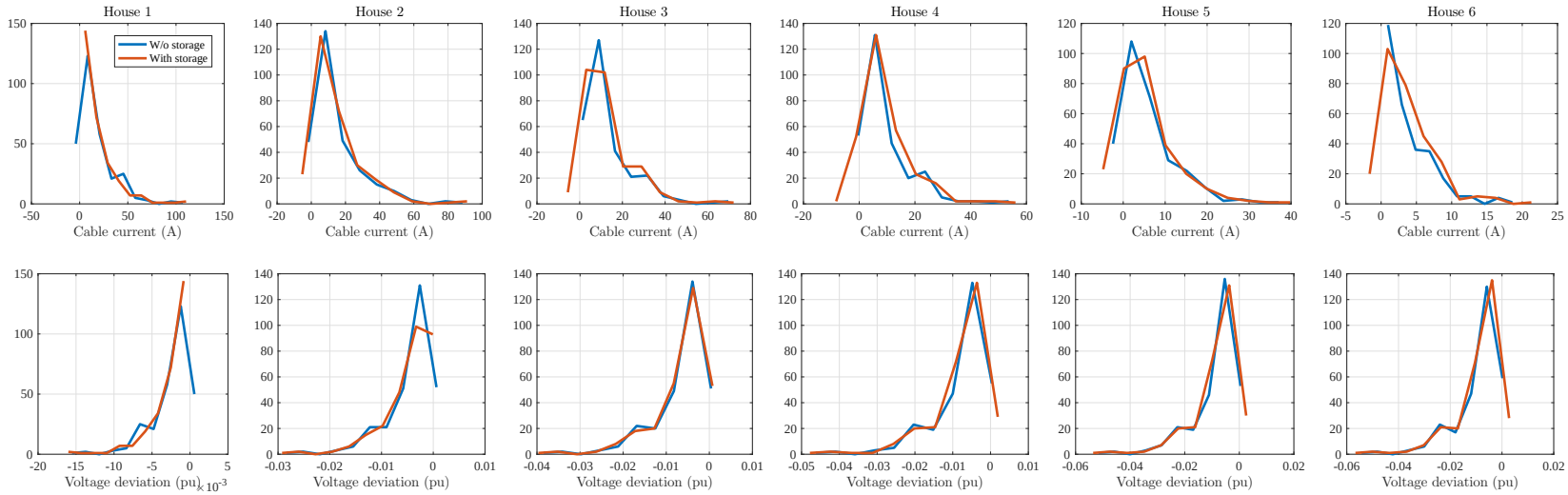

Figure 4.6: Histogram showing the distribution of cable currents (top) and voltage deviations (bottom) at each house during the time period of interest in Case 1.

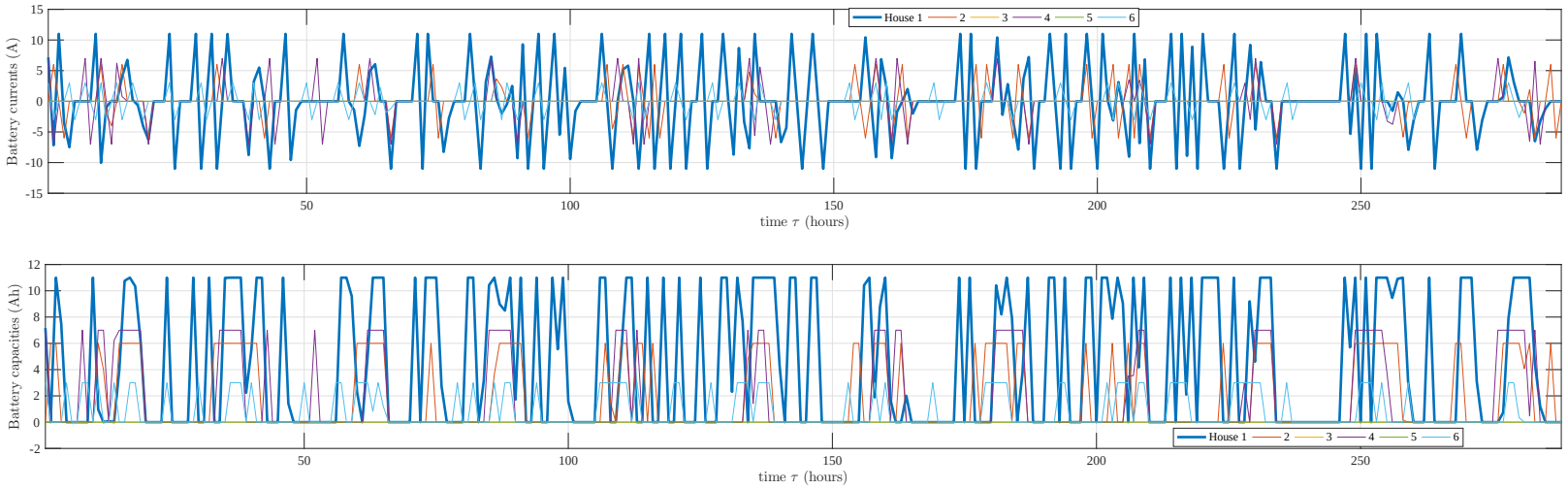

Figure 4.7: Battery current (top) and charge capacity (bottom) profiles for each house over the given time period of operation.

4.3.2 Case 2: Optimization under uncertainty using Monte-Carlo simulations.

Solving for battery sizes under perfect scenarios only produces conservative results in terms of operational economics for longer periods of time. This is especially true taking into account the variability of load and generation at the distribution level or the small microgrid level. It is well known that forecast uncertainty has a profound effect on sizing and installation problems in general [12]. Typically, the solution that copes with the worst case scenario is chosen in such situations. But, such decision may oversize the batteries for prolonged operation thereby reducing the overall benefit in the microgrid. Since the availability of a master source is essential in our case, assuming that large deviations in energy are taken care of by this source, we can perform a Monte-Carlo simulation based analysis to address uncertainty in demand and generation forecasts. In this manner, we can analyze the networks response to varying demand profiles, and, choose the sizing decision that can withstand certain level of deviation from predictions.

For the Monte-Carlo simulations, we have chosen daily demand data from the annual demand data for a typical Victorian customer [16]. The PV data is also chosen in a similar fashion adding white Gaussian noise with SNR = 20 to PV data from [100]. Each simulation begins on a random day in a year and runs for 12 days at an instance. We ran approximately 4000 simulations to derive the best estimate on sizing decisions. It should be mentioned that we used linear programming to obtain the sizing decisions and rounded them to the nearest greater integer, mainly due computational constraints. The number of decision variables = 6 battery currents $\times$ 24 hours in a day $\times$ 12 days + 6 battery sizing decisions = 1734 for one instance of simulation. The constraint matrix is size 13872 $\times$ 1734 and the time taken to solve the problem as an LP is 10 seconds on average. With integer decision variables on battery sizing, the time taken to solve increases to 69 seconds on average, where majority of the time is spent on iterations for obtaining integer values for the sizing decisions following an optimal LP

Table 4.4: Battery sizing scenarios following Monte-Carlo simulation analysis (Case 2).

House No.	1	2	3	4	5	6
Battery Capacity (Ah) scenario 1	0	0	0	0	0	0
Battery Capacity (Ah) scenario 2	11	0	0	4	4	4
Battery Capacity (Ah) scenario 3	11	0	0	7	7	7
Battery Capacity (Ah) scenario 4	11	11	11	11	11	11

solution. Hence, the LP has been chosen the fastest approach to address the problem. The rounding decision may depreciate the optimality of the sizing decision. This is reduction in optimality is comparable with that arising from forecast error.

The histograms in Figure 4.8 show the distribution of sizing decisions over all the scenarios simulated. It can be clearly seen that house 1 needs a 11 Ah size battery to cope with the excess PV generation. The sizes of batteries at the remaining houses highly varies. However, house 4,5 and 6 need at least a small battery (approximately 4 Ah in all cases) to satisfy local constraints. As remarked in Remark 4.2.1, the rounded LP solutions may be sub-optimal for each particular instance. Once the batteries decision are made using the Monte-Carlo simulation analysis, we can use our optimization algorithm with (4.1) instead of (4.2) to obtain the battery charging and discharging decisions that satisfy given constraints for varying fixed length forecasts, thereby reaching a local optimum for the network based on the rounded battery size. Observe that complexity of the optimization problem is reduced by the number of battery sizing integer decisions, thereby reducing the overall computational overhead. This method is termed as receding horizon control.

We have used such control to see how our sizing decisions, based on Monte-Carlo simulations, can cope with weekly (7 day) load and generation changes in a year. The data used here is similar to the earlier case, albeit being an year long. These results are shown in Figure 4.9. In this figure, we compare the economics of four different scenarios

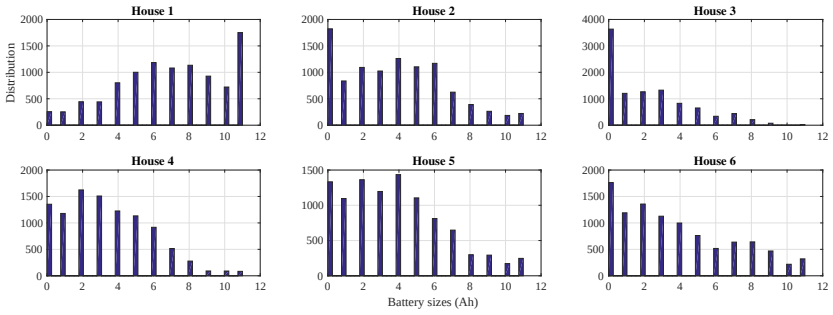

Figure 4.8: Distribution of battery sizing decisions from Monte-Carlo type simulations (Case 2).

given in Table 4.4. Scenarios 2 and 3 are based on the histograms and have similar battery positions. However, the constituent battery sizes are different. In scenario 1, no batteries are installed making the capital investment on batteries zero. The operational costs are the highest of all scenarios as the price arbitrage cannot be utilized. The reverse power flow impedes PV generation in scenarios 1 and 2. The PV curtailment is carried out by reducing the PV output to zero when the voltage constraints are violated. The violations are on an hourly basis in a 12 day window since the problem is solved 12 days at a time. We re-solve the optimization problem for an entire year with the curtailed PV output to obtain the results post-curtailment. Cost of the PV energy wasted is calculated as the value of the PV energy at a specified time based on the daily price curves. The batteries in scenario 4 are extremely oversized for the given network if the forecasts are reasonable. The lower operational costs are compromised by the huge investment upfront. The optimal solution, in this case, is scenario 3 where the PV is not wasted and the battery sizes are moderate. This leads to proper utilization of time-of-use price arbitrage as well as all the PV generation. The smaller battery sizes will also need much lower capital investment than scenario 4 adding to the overall benefit.

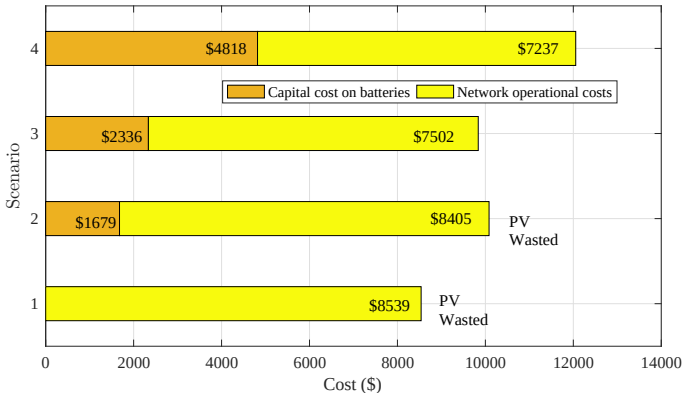

Figure 4.9: Cost of operating the microgrid under different sizing scenarios given in Table 4.4.

4.4 Summary

In this work we have shown how to optimally size and place a battery in a radial master-slave microgrid network. We formulated an optimization problem and solved it for a particular example of a radial network of 6 houses with monthly average profiles over one year using MILP block-set in MATLAB. Being a simplified optimization approach, our method relies on the accuracy of the load, generation and price forecasts. However, when the accuracy of the forecasts is under question and the battery sizes are fixed, our optimization algorithm can be used for receding horizon type control or online optimization-based control to maximize the benefit of operating batteries. Results obtained from the Monte-Carlo simulations extend our understanding of the given microgrid by subjecting it to a range of forecasts. Sizing decisions that follow from the Monte-Carlo simulation analysis are shown to be more resilient to small changes, albeit being sub-optimal from an economic perspective.

✧✧✧

Part IV

CONTROLLING PARALLEL CONVERTER BASED GENERATION

5

Modified Frequency Droop

5.1 Frequency droop and clock mismatches

FREQUENCY droop is envisaged as a complete solution to address the problem of operating converter interfaced sources in parallel over many years. The impact of clock drifts on frequency droop controlled microgrids has been neglected by majority literature and will be discussed in this chapter.

5.1.1 Assumptions

In the remainder of this chapter we assume the following:

- there are n inverters in the microgrid that are interfaced via controllable power electronics and have a DC link (for example, a storage unit) that can allow bi-directional power flow. Since we are not looking at long term operation of the sources, the battery here can also be considered as an infinite DC bus in the time period of interest;
- the output voltage amplitude of the inverter is held at a constant value. In other words, the analysis carried out here does not consider the dynamics of voltage amplitude and any voltage amplitude control loops such as, reactive power voltage droop, etc., are neglected;

- the line resistances, although present, are assumed to be small as per the traditional frequency/angle droop controller assumptions. In this regard, if this was not the case, a virtual impedance emulation technique can be used to ensure this assumption is valid;

- we analyze the network based on Kron reduction using an assumption that the loads are constant impedance type. So we have Y_{ii} as the self-admittance on inverter i and Y_{ik} as the admittance between inverters i and k . The admittance is defined as $Y_{ik} = G_{ik} + jB_{ik} = |Y_{ik}|\angle\phi_{ik}$ where G is the conductance, B is the susceptance at the nominal frequency and θ is the admittance angle. We recommend the reader to refer to Appendix C for more details on Kron reduction and [18] for discussion on implications that arise from different load types.

- the reference signal, $v_{i,ref}(t_i)$ is perfectly tracked by the inner (voltage/current) control loops of the inverter, any changes to the reference signal, either in voltage amplitude and / or frequency are reflected by equivalent proportional changes in the output voltage. For proper voltage reference tracking, the reference signal $v_{i,ref}(t_i)$ at each inverter is assumed to be a constant value within the carrier interval, i.e., the switching frequency [55]. This essentially means that any control that changes the reference signal should not act faster than the switching dynamics.

- following the previous assumption, microgrid inverter modelling adopted in this chapter is consistent with Section 3.4. For example, in Figure 5.1 the sources v_1, v_2 and v_3 are the simplified representations converter based generation that have a local clock but represented in a global time t.

5.1.2 Power sharing mismatches in steady state

It is well-known from the literature, see for example [32, 119, 136, 137], that the power frequency droop controller has first order oscillator dynamics. Here, we revisit the theory considered in [135] and provide an extension to their stability theorem. Consider a

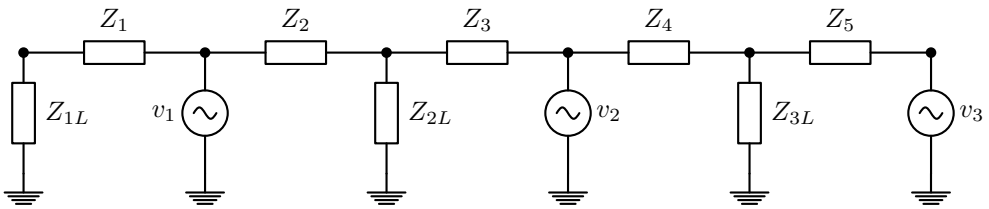

Figure 5.1: An example of microgrid consisting of three converter based sources supplying three constant impedance loads.

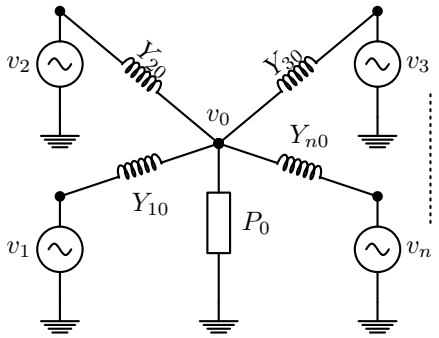

Figure 5.2: Star topology - n droop controlled inverter systems supplying a common load P_0. Each droop controlled inverter is represented by a voltage, v_i and it is connected to the load P_0 at v_0 through an output admittance Y_{i0}, respectively.

star connected frequency droop controlled microgrid, as shown in Figure 5.2. Each droop controlled source, v_i is supplying a (common) constant power load, P_0 through an impedance Y_{i0}, respectively. It is assumed that the voltage amplitude at each voltage source is constant. It is also assumed that the lines have no resistance, i.e., the lines are lossless. Although some resistance is required to be able to define a proper equilibrium, this system is still a good approximation for quasi-steady state analysis. The power flow equations in such a lossless microgrid network are given by the algebraic expression

$$P_0 = -\sum_{i=1}^{n} V_i V_0 |Y_{i0}| \sin(\delta_i - \delta_0).$$

5.1.3 Clock drift effect

The integration process at each inverter will be affected by the clock drifts [120]. Using definitions from (3.13), we can express the local integration/differentiation as follows ,

$$\frac{d(\cdot)}{dt_i} = \gamma_i \frac{d(\cdot)}{dt},$$

where $\gamma_i = \dfrac{1}{1+\epsilon_i}$. Both γ_i and ϵ_i are variables that describe how the local clock deviates from the global clock. As described earlier, we need to modify the droop equation to show the effect of clock drifts on frequency synchronization. Hence, we rewrite the frequency, ω_i incorporated with the effect of clock drifts as follows:

$$\omega_i = \gamma_i \dot{\delta}_i,$$

This transforms the droop controller in (3.7) to,

$$\gamma_i \dot{\delta}_i = \omega^* - m_i(P_i - P_i^*). \tag{5.1}$$

The feedback power P_i is a local variable measured at the ith inverter output, ω^* and P_i^* are the local constants. The above equation can be rewritten as,

$$D_i \gamma_i \dot{\delta}_i = D_i \omega^* + P_i^* - P_i,$$

where $D_i = m_i^{-1}$. By making use of the load flow equations for a star connected lossless differential algebraic network the above equation can be re-written as,

$$D_i \gamma_i \dot{\delta}_i = P_{d,i}^* - V_i V_0 |Y_{i0}| \sin(\delta_i - \delta_0), \qquad i \in \{1, \ldots, n\}, \tag{5.2}$$

where $P_{d,i}^* = D_i \omega^* + P_i^*$ is the nominal power of the ith inverter. The equation above is exactly of the form equation (6) in [135]. The synchronizing frequency, ω_{sync} can now be calculated by summing the expression (5.2) over i, to arrive at

$$\omega_{sync} = \sum_{i=0}^{n} P_{d,i}^* / \sum_{i=1}^{n} D_i \gamma_i,$$

with $D_0 = 0$ and $P_0 = P_0^*$. Based on this frequency, we provide an extension to the parametric stability condition provided in [135] as shown below[1]:

$$\Xi \triangleq \max_{i \in \{1,\ldots,n\}} |(P_{d,i}^* - \omega_{sync} D_i \gamma_i)/a_{i0}| < 1,$$

where $a_{i0} = V_i V_0 |Y_{i0}|$ is the physical maximum power that can flow through the cable section. Refer to [135] for the full proof. However, our primary interest is to show that there are power deviations associated with this clock drift.

Consider the star connected scenario with two inverters i, j. The power supplied by the ith inverter, P_i is given by,

$$P_i = P_{d,i}^* - \omega_{sync} D_i \gamma_i.$$

Similarly, the power supplied by the jth inverter is given by,

$$P_j = P_{d,j}^* - \omega_{sync} D_j \gamma_j.$$

The difference between the powers supplied by these inverters is given by,

$$\begin{aligned} \Delta P_{ij} &= P_i - P_j \\ &= (P_{d,i}^* - \omega_{sync} D_i \gamma_i) \\ &\quad - (P_{d,j}^* - \omega_{sync} D_j \gamma_j). \end{aligned}$$

Assuming all other parameters are exactly the same, the power sharing deviation introduced by (non-identical) clock drift is:

$$\Delta P_{ij} = D[\omega_{sync}(\gamma_i - \gamma_j)].$$

This shows that the power sharing is perturbed by clock deviations which may give rise to instabilities, especially when cable sections are heavily loaded, i.e., $\Xi_{\text{ideal}} \rightarrowtail 1$. Analogous results can be derived for other configurations [136].

[1] $\mathbf{\Gamma}$ is replaced by Ξ to avoid abuse of notation in later sections

An alternative method to verify the effect of clock drifts is to consider the dynamics of the phase angle alone in droop controlled inverter based systems. The phase evolution of droop controlled systems is given (5.1). Considering the same example of two inverters, i, j, we have

$$\dot{\delta_i} = \gamma_i^{-1}(\omega^* - m_i P_i + m_i P_i^*),$$
$$\dot{\delta_j} = \gamma_j^{-1}(\omega^* - m_j P_j + m_j P_j^*).$$

In stable steady state if any, both these values are equal leading to

$$\gamma_i^{-1}(\omega^* - m_i P_i^s + m_i P_i^*) = \gamma_j^{-1}(\omega^* - m_j P_j^s + m_j P_j^*),$$

where P_i^s, P_j^s are the steady state output powers of inverters i, j respectively. Assuming $P_i^* = P_j^* = 0$ and $m_i = m_j = m$, we have

$$\frac{\omega^*}{\gamma_i} - \frac{\omega^*}{\gamma_j} = m\left(\frac{P_i^s}{\gamma_i} - \frac{P_j^s}{\gamma_j}\right). \tag{5.3}$$

In general, the maximum power sharing deviation the results from non-identical clocks is

$$\frac{\max \Delta P}{\omega^*} = \max_i \left(\frac{1}{\gamma_i m_i}\right) - \min_j \left(\frac{1}{\gamma_j m_j}\right), \quad \forall i \neq j \leq n.$$

In some situations these power variations can cause phase angles to navigate beyond their stability boundary (c.f [136]) causing instability.

To summarize, there are two variables that largely affect the power sharing. First, the droop coefficient, m_i - it can be made large subject to large frequency deviations and oscillatory transient response. It follows that we must consider the clock drift in designing the droop control. But, the clock drifts are unknown and very hard to measure. Second, the (relative) clock drifts, γ_i - which are hard to measure as well. Therefore, it is very useful to find a method that ensures proper power sharing and stability for arbitrarily small droop coefficients even in the presence of unknown clock mismatches without the need of measuring extra variables. Another major advantage is that the

resilience for frequency dependent loads will then automatically be ensured without any extra control owing to the small frequency deviation from small droop coefficients. In other words, when the control is effective, the network model as adopted is justified.

5.2 Modified frequency droop and stability analysis

From (3.7), considering the clock mismatches the dynamics of the phase angle of the ith inverter in a frequency droop controlled microgrid are represented by:

$$\gamma_i \frac{d}{dt}\delta_i = \omega_i = \omega^* - m_i P_i + m_i P_i^*.$$

The feedback power P_i is a local variable measured at the ith inverter output; ω^* and P_i^* are the local constants. It is therefore understood that there is no requirement for additional communications for the simple frequency droop controller implementation. This power measurement often involves a filter stage and the associated dynamics are as follows:

$$\tau_i \gamma_i \frac{d}{dt} P_i = -P_i + p_i. \tag{5.4}$$

where τ_i is the low-pass filter time period and p_i is the actual output power of the ith inverter which is given by [77]:

$$p_i = G_{ii} V_i^2 + \sum_{j \neq i} |Y_{ij}| V_i V_j \sin(\delta_i - \delta_j + \phi_{ij}).$$

For more details on Kron reduction, see Appendix C. As seen earlier, the above criterion ensures proper power sharing between inverters under ideal conditions. We have also seen that the power sharing properties will be destroyed in the presence of frequency uncertainties; this was also shown in [120, 162]. To counter-act this anomaly we introduce a modified frequency droop control. We make use of inter-node communications to include an integral control action that enables inverters to share power according to a sharing criterion even in the presence of clock uncertainties. This kind of communication architecture is most commonly used in power systems for secondary control ([7] for instance).

Remark 5.2.1. *We introduce an integral term z_i defined as follows:*

$$\gamma_i \frac{d}{dt} z_i = k_i \sum_{j \sim \mathcal{N}_i} (m_i P_i - m_j P_j), \tag{5.5}$$

where $k_i > 0$ is the local integral control gain and $\mathcal{N}_i$ represents the set of inverters communicating with the ith inverter. We include this integral control term as a negative feedback to the frequency droop controller as:

$$\gamma_i \frac{d}{dt} \delta_i = \omega^* - m_i P_i + m_i P_i^* - z_i. \tag{5.6}$$

The integral terms have zero initial value. The importance of this will be made clear in the later parts of this chapter. It is apparent that there are no extra measurements required to perform the integral control and the communications associated are distributed. Thus, the complexity of implementation is not significantly increased and the system robustness / modularity requirements are still well-preserved. The ability of this control technique to ensure proper power sharing and stability is discussed next.

5.2.1 Stability analysis

Definition 5.2.2. *Define vectors / matrices:*

$$\begin{aligned}
1_n &:= col(1), & \mathbf{P}_a &:= col(p_i), & \mathbf{M} &:= diag(m_i),\\
0_n &:= col(0), & \boldsymbol{\delta} &:= col(\boldsymbol{\delta}_i), & \boldsymbol{\Gamma} &:= diag(\gamma_i),\\
\mathbf{P}_m &:= col(P_i), & \mathbf{V} &:= col(V_i), & \mathbf{K} &:= diag(k_i),\\
\mathbf{P}^* &:= col(P_i^*), & \mathbf{Z} &:= col(z_i), & \mathbf{T} &:= diag(\tau_{p,i}).
\end{aligned}$$

From equations (5.4), (5.5) and (5.6) and using the vector notation (from Definition 5.2.2) the dynamics of the microgrid can be represented by:

$$\begin{aligned}
\boldsymbol{\Gamma}\dot{\boldsymbol{\delta}} &= \omega^* 1_n - \mathbf{M}(\mathbf{P}_m - \mathbf{P}^*) - \mathbf{Z},\\
\boldsymbol{\Gamma}\mathbf{T}\dot{\mathbf{P}}_m &= -\mathbf{P}_m + \mathbf{P}_a,\\
\boldsymbol{\Gamma}\dot{\mathbf{Z}} &= \mathbf{K}\mathbf{L}_c\mathbf{M}\mathbf{P}_m.
\end{aligned} \tag{5.7}$$

Assumption 5.2.3. *We assume that there exists a steady-state in the system, the equilibrium vectors are denoted by* $\boldsymbol{\delta}^s$, $\mathbf{V}^s$, $\mathbf{P}^s_m$ *and* $\mathbf{Z}^s$ *and the deviation of these state vectors from their equilibrium points is denoted by the deviation vectors* $\bar{\boldsymbol{\delta}}$, $\bar{\mathbf{V}}$, $\bar{\mathbf{P}}_m$ *and* $\bar{\mathbf{Z}}$, *respectively. We also assume that the equilibrium phase angle vector is in the n-torus,* $\boldsymbol{\delta}^s \in \mathbb{T}^n : \{-\pi, \pi\}\ s.t\ \frac{\pi}{2} > |\delta^s_i - \delta^s_k + \phi_{ik}|\ \ i, k = 1, \ldots, n.$

Definition 5.2.4. *Linearizing the non-linear power flow term* $\mathbf{P}_a$ *in the ordinary differential equation set* (5.7) *with respect to* $\boldsymbol{\delta}$ *at equilibrium vectors* $\boldsymbol{\delta}^s, \mathbf{V}^s$ *yields a linear dynamical system which is much easier to analyze. This linearization is defined as:*

$$\mathbf{L}_n := \frac{\partial \mathbf{P}_a}{\partial \boldsymbol{\delta}}_{|\boldsymbol{\delta}^s, \mathbf{V}^s} = \begin{bmatrix} \frac{\partial p_1}{\partial \delta_1} & \cdots & \frac{\partial p_1}{\partial \delta_n} \\ \vdots & \ddots & \vdots \\ \frac{\partial p_n}{\partial \delta_1} & \cdots & \frac{\partial p_n}{\partial \delta_n} \end{bmatrix}_{|\boldsymbol{\delta}^s, \mathbf{V}^s} .$$

The matrix $\mathbf{L}_n$ is a network Laplacian with positive diagonal elements (l_{ii}), non-positive off-diagonal elements (l_{ik}) as shown in (5.8), (5.9) which obey condition (5.10):

$$l_{ii} = \sum_{i \neq k} a_{ik} \cos(\delta^s_i - \delta^s_k + \phi_{ik}), \tag{5.8}$$

$$l_{ik} = -a_{ik} \cos(\delta^s_i - \delta^s_k + \phi_{ik}), \tag{5.9}$$

$$l_{ii} = -\sum_{k=1, k \neq i}^{n} l_{ik}, \tag{5.10}$$

with $a_{ik} = V^s_i V^s_k |Y_{ik}|$. The matrix $\mathbf{L}_n$ has a simple eigenvalue that is zero and the remaining eigenvalues have a positive real part [119]. It is also important to note that the vector 1_n forms the basis of the kernel of $\mathbf{L}_n$ i.e., for any vector $w = \beta 1_n, \beta \in \mathbb{R}$ we have $\mathbf{L}_n w = 0_n$.

Assumption 5.2.5. *We assume that the power measurement low-pass filter coefficients of each inverter system are identical, i.e.,* $\mathbf{T}^{-1} = f\mathbf{I}_n, \quad i = 1, \ldots, n.$ *We also assume that the integral control gains are identical i.e.,* $\mathbf{K} = k\mathbf{I}_n, \quad i = 1, \ldots, n.$

Following linearization and embedding the Assumptions 5.2.3 and 5.2.5 into (5.7) we have the following closed loop microgrid model that reflects the dynamics around the

equilibrium:

$$(\mathbf{I}_3 \otimes \mathbf{\Gamma}) \begin{bmatrix} \dot{\bar{\boldsymbol{\delta}}} \\ \dot{\bar{\mathbf{P}}}_m \\ \dot{\bar{\mathbf{Z}}} \end{bmatrix} = \underbrace{\begin{bmatrix} 0_{n\times n} & -\mathbf{M} & -\mathbf{I}_n \\ f\mathbf{L}_n & -f\mathbf{I}_n & 0_{n\times n} \\ 0_{n\times n} & k\mathbf{L}_c\mathbf{M} & 0_{n\times n} \end{bmatrix}}_{:=\mathbf{F}} \begin{bmatrix} \bar{\boldsymbol{\delta}} \\ \bar{\mathbf{P}}_m \\ \bar{\mathbf{Z}} \end{bmatrix}. \tag{5.11}$$

The eigenvalues of the state transition matrix $\mathbf{F}$ defined in (5.11) will determine the stability of the modified frequency droop controller based microgrid around the given equilibrium point.

Theorem 5.2.6 (**Power sharing**). *Suppose that σ_i is the i^{th} the eigenvalue of the matrix product $\mathbf{ML}_n$ and similarly, μ_i is the i^{th} eigenvalue of the matrix product $\mathbf{L}_c\mathbf{ML}_n$. Consequently, the modified frequency droop control system represented by* (5.11) *possesses $(3n-2)$ eigenvalues that have a negative real part (the remaining are zero eigenvalues) for a choice of k given by:*

$$k < f \min_{>0} \Re\left(\frac{\sigma_i}{\mu_i}\right). \tag{5.12}$$

leading to proportional power sharing within the microgrid.

Proof: We utilize the arguments explored in [8, 119] for our proof. Firstly, in stable steady state, the integral controller ensures that the power shared between inverters meets the prescribed power sharing criterion. Recall that the matrix $\mathbf{L}_c$ is the communication Laplacian with positive eigenvalues along with one zero eigenvalue. Consequently, in steady state we have,

$$0_n = k\mathbf{L}_c\mathbf{M}\mathbf{P}^s_m \iff \mathbf{M}\mathbf{P}^s_m = \nu 1_n \iff m_i P^s_i = m_j P^s_j,$$

where $\nu \in \mathbb{R} \setminus \{0\}$ is a constant for all the inverters $i, j \in n$ and is based on the initial conditions and network aggregate load. To prove the second part of our claim, we operate on the linear state transition matrix $\mathbf{F}$. Consider the characteristic equation of $\mathbf{F}$ given

by,

$$\det(\lambda_{\mathbf{F}}\mathbf{I}_{3n} - \mathbf{F}) = \begin{vmatrix} \lambda_{\mathbf{F}}\mathbf{I}_n & \mathbf{M} & \mathbf{I}_n \\ -f\mathbf{L}_n & (\lambda_{\mathbf{F}} + f)\mathbf{I}_n & 0_{n\times n} \\ 0_{n\times n} & -k\mathbf{L}_c\mathbf{M} & \lambda_{\mathbf{F}}\mathbf{I}_n \end{vmatrix}.$$

Using identities from [132], we have

$$\det(\lambda_{\mathbf{F}}\mathbf{I}_{3n} - \mathbf{F}) = \det(\mathbf{Q}(\lambda_{\mathbf{F}})),$$

where

$$\mathbf{Q}(\lambda_{\mathbf{F}}) = \lambda_{\mathbf{F}}^3 I_n + f\lambda_{\mathbf{F}}^2 I_n + f\lambda_{\mathbf{F}}\mathbf{M}\mathbf{L}_n + fk\mathbf{L}_c\mathbf{M}\mathbf{L}_n. \tag{5.13}$$

To compute the eigenvalues, let $v \in \mathbb{C}^n$ be any vector with $v^*v = 1$. Left multiplying the characteristic polynomial (5.13) by v_i^* and right multiplying by v_i, $\forall i = 1, \ldots, n$, yields,

$$\Phi_i\lambda_{\mathbf{F},i}^3 + \Pi_i\lambda_{\mathbf{F},i}^2 + \Psi_i\lambda_{\mathbf{F},i} + \Sigma_i = 0, \quad i = 1, \ldots, n, \tag{5.14}$$

where $\Phi_i = 1$, $\Pi_i = f$, $\Psi_i = fv_i^*(\mathbf{M}\mathbf{L}_n)v_i$ and $\Sigma_i = fkv_i^*(\mathbf{L}_c\mathbf{M}\mathbf{L}_n)v_i$, $\quad i = 1, \ldots, n$.

- When $v_1 = \psi 1_n$, $\psi \in \mathbb{R} \setminus \{0\}$ we have $v_1^*\mathbf{M}\mathbf{L}_n v_1 = 0$ and $v_1^*\mathbf{L}_c\mathbf{M}\mathbf{L}_n v_1 = 0$, by definition. Consequently (5.14) becomes:

  $$\lambda_{\mathbf{F},1}^2(\Phi_1\lambda_{\mathbf{F},1} + \Pi_1) = 0.$$

  This implies that $\lambda_{\mathbf{F},1_{1,2}} = 0$ are the two zero eigenvalues of the matrix $\mathbf{F}$. The third eigenvalue associated with this eigenvector ($\lambda_{\mathbf{F},1_3} = \dfrac{-\Pi_1}{\Phi_1} = -f < 0$) is always negative, by definition.

- The remaining $(3n-3)$ eigenvalues ($\lambda_{\mathbf{F},i_{1,2,3}}, \quad i = 2, \ldots, n$) will have a negative real part if and only if,

  $$\Phi_i\Sigma_i < \Pi_i\Psi_i, \quad i = 2, \ldots, n. \tag{5.15}$$

We can ensure (5.15) is always satisfied by imposing bounds on k. We know

$$\begin{aligned} \Pi_i \Psi_i &= f^2 v_i^* \mathbf{M} \mathbf{L}_n v_i, \quad i = 2, \ldots, n, \\ &= f^2 \sigma_i, \end{aligned} \tag{5.16}$$

from the theorem statement. Based on properties of matrices $\mathbf{L}_n$, $\mathbf{L}_c$ and $\mathbf{M}$ we observe that only the vector 1_n forms the basis of the kernel of $\mathbf{L}_c \mathbf{M} \mathbf{L}_n$. We remark that this product term has only one zero eigenvalue since $\mathbf{L}_n$ cannot map any non-zero vector to the basis of its kernel owing to orthogonality of kernel and image spaces [22]. Therefore, from the theorem statement we also have

$$\begin{aligned} \Phi_i \Sigma_i &= f k v_i^* \mathbf{L}_c \mathbf{M} \mathbf{L}_n v_i, \quad i = 2, \ldots, n, \\ &= f k \mu_i. \end{aligned} \tag{5.17}$$

Using (5.16) and (5.17), we observe that the choice of k according to (5.12) ensures that (5.15) holds and will consequently result in remaining eigenvalues that only have a negative real part and ensure stability as discussed in Section 2.7. In practice, observe that the matrix $\mathbf{\Gamma}$ is an invertible diagonal matrix with positive entries close to unity and hence positive-definite. The signs of the eigenvalues of $\mathbf{F}$ are not affected by the positive definite tensor product $\mathbf{I}_3 \otimes \mathbf{\Gamma}$, finishing the proof. □

5.2.2 Eliminating redundancy

We have shown in the proof of Theorem 5.2.6 that there are two zero eigenvalues for the linearized closed-loop system (5.11). Next we show that we can factor out the dynamics of the centre manifold (c.f Section 2.7) thus proving exponential stability. For this purpose we define a new state vector, $\mathbf{y}$, by utilizing the translational invariance in phase angle, $\boldsymbol{\delta}$. The elements of $\mathbf{y}$ are given in (5.18). We can also redefine z_1 as shown in (5.19) by imposing zero initial conditions on all the integral control variables, z_i, i.e., $z_i(t_{=0}) = 0$ and based on the fact that vector 1_n is the basis of the kernel of $\mathbf{L}_c$ (by

which $\mathbf{Z}$ is defined) and Assumption 5.2.5.

$$y_\ell = \delta_\ell - \delta_1, \quad \forall \ell = 2, \ldots, n \tag{5.18}$$

$$z_1 = -\frac{1}{\gamma_1} \sum_{\ell=2}^{n} \gamma_\ell z_\ell, \quad \forall \ell = 2, \ldots, n \tag{5.19}$$

The evolution of the new state, y_ℓ can be written as

$$\begin{aligned}\gamma_\ell \dot{y}_\ell &= \gamma_\ell \dot{\delta}_\ell - \gamma_\ell \dot{\delta}_1 \\ &= \omega^* - m_\ell (P_\ell - P_\ell^*) - z_\ell + \frac{\gamma_\ell}{\gamma_1}(m_1(P_1 - P_1^*) - \omega^*) - \frac{\gamma_\ell}{\gamma_1^2} \sum_\ell \gamma_\ell z_\ell\end{aligned}$$

Definition 5.2.7. *Define*

$$\begin{aligned}\mathbf{Z}_{new} &:= col(z_2, \cdots, z_n), \\ \boldsymbol{\gamma}_{new} &:= col(\gamma_2, \cdots, \gamma_n), \\ \boldsymbol{\Gamma}_{new} &:= diag(\boldsymbol{\gamma}_{new}), \\ \mathbf{R}_0 &:= \left[\begin{array}{c:c} 0_{(n-1)\times 1} & \mathbf{I}_{(n-1)} \end{array}\right], \\ \mathbf{V} &:= \left[\begin{array}{c:c} \dfrac{m_1}{\gamma_1}\boldsymbol{\gamma}_{new} & -\mathbf{R}_0 \mathbf{M} \mathbf{R}_0^T \end{array}\right], \\ \mathbf{L}_n \mathbf{R}_0^T &= \frac{\partial \mathbf{P}_a}{\partial \mathbf{y}}_{|\mathbf{y}^s, \mathbf{V}^s}.\end{aligned}$$

We also define $\bar{\mathbf{y}} = \mathbf{y} - \mathbf{y}^s$ *and* $\bar{\mathbf{Z}}_{new} = \mathbf{Z}_{new} - \mathbf{Z}_{new}^s$*, where* $\mathbf{y}^s$ *and* $\mathbf{Z}_{new}^s$ *are the equilibrium vector associated with* $\mathbf{y}$ *and* $\mathbf{Z}_{new}$*, respectively.*

Based on the new definitions, the linearized closed loop system can be given by

$$\mathbf{U}\begin{bmatrix} \dot{\bar{\mathbf{y}}} \\ \dot{\bar{\mathbf{P}}}_m \\ \dot{\bar{\mathbf{Z}}}_{new} \end{bmatrix} = \underbrace{\left[\begin{array}{c:c:c} 0_{(n-1)\times(n-1)} & \mathbf{V} & \dfrac{-\boldsymbol{\gamma}_{new}\boldsymbol{\gamma}'_{new}}{\gamma_1^2} - \mathbf{I}_{(n-1)} \\ \hdashline \mathbf{L}_n \mathbf{R}_0^T & -f\mathbf{I}_n & 0_{n\times(n-1)} \\ \hdashline 0_{(n-1)\times(n-1)} & k\mathbf{R}_0 \mathbf{L}_c \mathbf{M} & 0_{(n-1)\times(n-1)} \end{array}\right]}_{:=\mathbf{F}_{new}} \begin{bmatrix} \bar{\mathbf{y}} \\ \bar{\mathbf{P}}_m \\ \bar{\mathbf{Z}}_{new} \end{bmatrix}$$

where $\mathbf{U} = diag(\boldsymbol{\Gamma}_{new}, \boldsymbol{\Gamma}, \boldsymbol{\Gamma}_{new})$. The matrices $\mathbf{F}$ and $\mathbf{F}_{new}$ represent the same modified frequency droop controlled system, albeit the latter having the redundant variables removed. It can be proved that this system is devoid of the zero eigenvalues by showing

$\mathbf{F}_{new}$ has a non-zero determinant. The determinant of $\mathbf{F}_{new}$ is

$$\det(\mathbf{F}_{new}) = \left| \frac{-\boldsymbol{\gamma}_{new}\boldsymbol{\gamma}'_{new}}{\gamma_1^2} - \mathbf{I}_{(n-1)} \right| \left| \begin{array}{c:c} \mathbf{L}_n\mathbf{R}_0^T & -f\mathbf{I}_n \\ \hdashline 0_{(n-1)\times(n-1)} & k\mathbf{R}_0\mathbf{L}_c\mathbf{M} \end{array} \right|$$

Since k and f are greater than zero by definition, we have:

$$\det(\mathbf{F}_{new}) \propto \left| \frac{-\boldsymbol{\gamma}_{new}\boldsymbol{\gamma}'_{new}}{\gamma_1^2} - \mathbf{I}_{(n-1)} \right| \left| \mathbf{R}_0\mathbf{L}_c\mathbf{M}\mathbf{L}_n\mathbf{R}_0^T \right| \tag{5.20}$$

By induction, we can show that the magnitude of the first term in (5.20) is $1 + \sum_{j=2}^{n} \gamma_j^2/\gamma_1^2$ which is monotonously increasing with n and always greater than one for values of γ considered in this chapter. The last term in (5.20) is obtained using Cauchy Binet's determinant formula [22]. Since the basis of the kernels of $\mathbf{L}_n$ and $\mathbf{L}_c$ cannot be mapped through the matrices $\mathbf{R}_0^T$ and $\mathbf{R}_0$, respectively, we can say that the determinant of this term is never zero. The remaining is a product of non-zero values proving $\det \mathbf{F}_{new} \neq 0$.

5.3 Simulations and discussion

Network 1

We initially present simulation results of a simple network shown in Figure 5.3 under clock drifts. We assumed lossless network for the sake of simplicity. According to our condition (5.12) any value of $0 < k < 5$ will achieve stability and equal power sharing. This is shown in Figure 5.4. Hopf bifurcation behaviour (the eigenvalues have zero real part, i.e. pure imaginary eigenvalues) is shown when $k = 5$ and the system is rendered unstable for a value of $k > 5$. This is shown in Figure 5.5 using the frequency difference, $(\omega_1 - \omega_2)$.

Network 2

Here we present simulation results of a microgrid system consisting of three single phase inverters and three loads (shown in Figure 5.1) which is representative of a typical

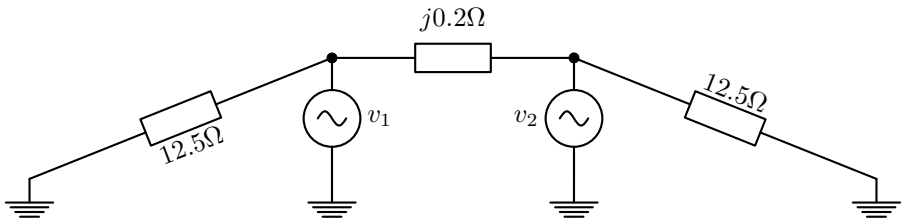

Figure 5.3: Kron reduced two inverter microgrid with parameters $m_i = 10^{-6}$ Hz/W, $V_i = 250V_{rms}$, $P_i^* = 0$W, $\omega^* = 50$Hz, $\gamma_1 = 1$, $\gamma_2 = 0.9998$ and $\mathbf{L}_c = [1\ -1; -1\ 1]$.

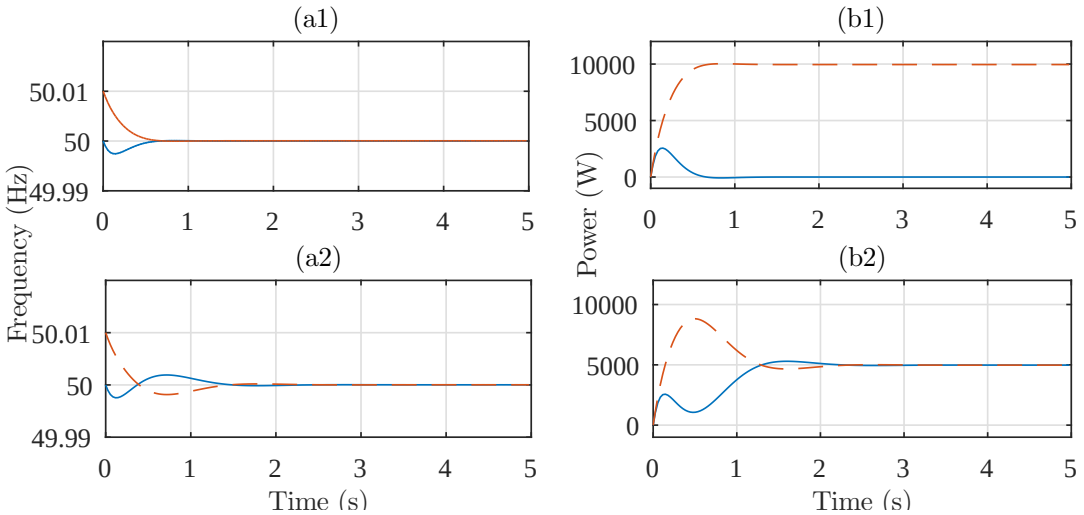

Figure 5.4: (a*) Frequency and (b*) power of inverters under (*1) traditional frequency droop with drifts and (*2) modified frequency droop with drifts and $k = 1$. – Inverter 1, - - Inverter 2.

distribution level islanded microgrid. The parameters of the system under consideration are given in Table 5.1 and are modified from [131]. The simulations are implemented in MATLAB Simpowersystems. Several case studies are simulated and the corresponding results discussed in this section.

It is worth mentioning that typical low voltage microgrids, like the one shown in simulations, are confined to relatively small neighbourhoods and the output impedances may be dominantly resistive. However, it is still reasonable to model the output impedance as inductive by taking advantage of virtual impedance emulation techniques [85] as re-

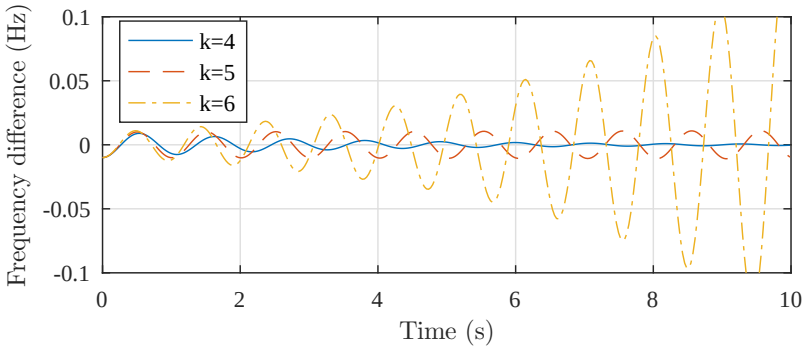

Figure 5.5: Frequency difference, $(\omega_1 - \omega_2)$ between inverters for various values of k.

Table 5.1: Simulation parameters for $(P - \omega)$ droop control based microgrid.

Parameter	**Value**
V_i	$250V_{rms}$
Z_i, i=2,4	0.02 + j0.2 Ω
Z_i, i=1,3,5	0.03 + j0.3 Ω
Z_{iL}, i=1,2,3	12.5 Ω
f	10 Hz
m_i	1×10^{-6} Hz/W
ω^*,P_i^*	50 Hz, 0 W

marked in the assumptions and also at the beginning of this thesis.

Case 1 : Inverters with identical clocks, disproportionate output impedances and no consensus controller

Initially we chose the clocks to be perfectly synchronized. There is no active consensus controller in this case. The corresponding results are shown in Figure 5.6. We can clearly see from the figure that after a small transient the frequency converges to a

constant (which is less than the rated value of 100π rad/s) and the power sharing between sources is accurate and according to the sharing plan. For this reason, the term $\mathbf{L}_c\mathbf{MP}_m$ converges to zero even when the control gain, k is zero. It must be noted that the distribution of line impedance has no effect on the real power sharing properties in inductive frequency droop controlled microgrid. The voltage remained at a constant value throughout, as controlled.

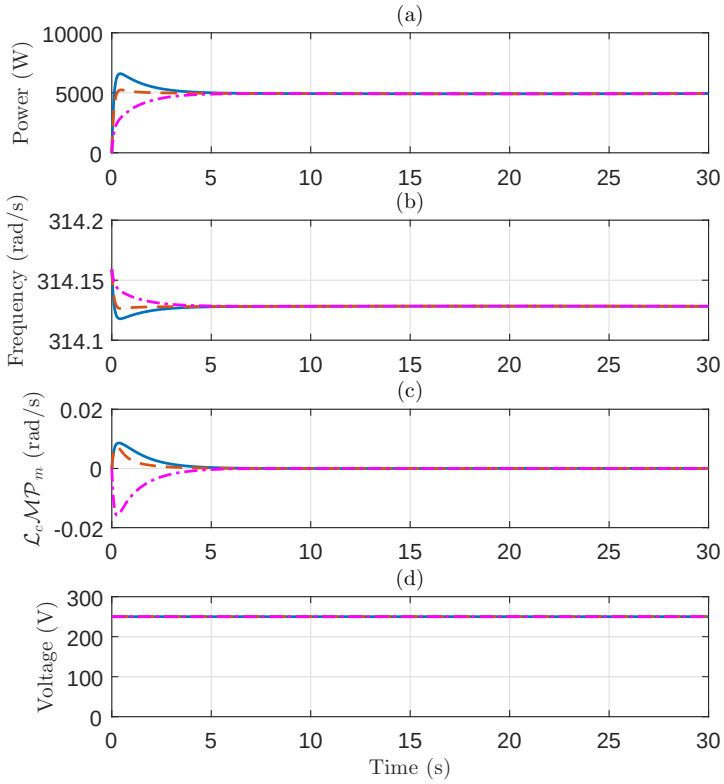

Figure 5.6: Outputs of the system with ideal clocks and $k_i = 0$. (a) Real power, (b) frequency, (c) $\mathbf{L}_c\mathbf{MP}_m$, and (d) Voltage. Inverter at bus 1 is represented by (—), at bus 2 by (- -) and at bus 3 by (-·-).

Case 2 : Inverters with non-identical clocks, disproportionate output impedances and no consensus controller

In the next set of simulations we chose the following clock drifts: $\gamma_1 = 0.9998, \gamma_2 = 0.9996$ and $\gamma_3 = 0.9994$. No integral action was implemented, i.e., $k = 0$. The results corresponding to these simulation parameters are shown in Figure 5.7. The frequencies still converge to a global average as mentioned earlier and the voltage is maintained constant as shown in Case 1. However, the clock drifts have a profound effect on power sharing. Since the inverter at bus 2 is at the average frequency its power output is according to the power sharing plan. However, the power sharing between the inverters 1 and 2 is largely perturbed. The calculation given below validates our discussion on clock drifts (5.3) earlier :
We have,

$$\begin{aligned} P_1 &= \frac{(\gamma_2 - \gamma_1)}{m}\frac{\omega^*}{\gamma_2} + \frac{\gamma_1}{\gamma_2}P_2 \\ &= \frac{(0.9996 - 0.9998)}{2\pi 10^{-6}} \times \frac{100\pi}{0.9996} + \frac{0.9998}{0.9996}5000 \\ &= -5003.0012006 \text{ or } \cong -0.5 \times 10^4 \text{W} \end{aligned}$$

The inverter on bus 1 consumes the excess power generated by its counterpart at bus 3 according to the power sharing criteria. It is clear that the inverter 1 is charging its DC side source. If there is no flexibility or restricted bidirectional power flow as assumed, the system loses its source and this might in turn lead to instability by overloading the remaining sources.

Case 3 : Inverters with non-identical clocks, disproportionate output impedances and active consensus controller

In the following scenario we have chosen the same clock drifts, namely, $\gamma_1 = 0.9998, \gamma_2 = 0.9996$ and $\gamma_3 = 0.9994$. The integral gain control is chosen to be $k = 0.3$, following our condition (5.12). Although there is a perturbation in the power sharing, the integral controller ensures proper power sharing as seen in Figure 5.8 (a). A small transient

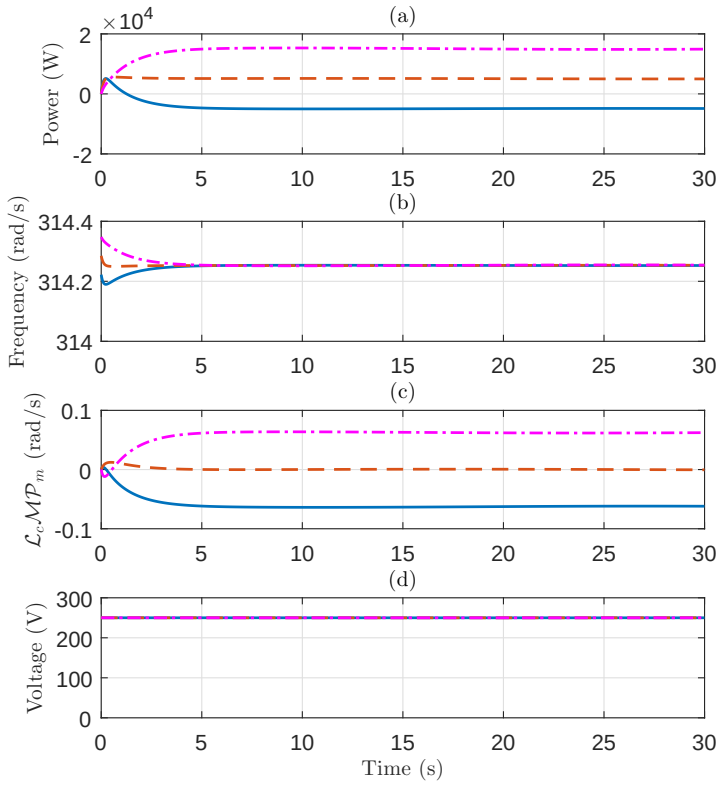

Figure 5.7: Outputs of the system with clock drifts and $k_i = 0$. (a) Real power (b) frequency, (c) $\mathbf{L}_c\mathbf{MP}_m$, and (d) Voltage. Inverter at bus 1 is represented by (—), at bus 2 by (- -) and at bus 3 by (-·-).

change is initiated in the frequencies of inverters by the integral controller modifying the phase angle in such way that the power sharing plan is accurately followed. The integral term reaches zero at around 10 s, depicting the same. As in all the previous cases the voltage remains constant as controlled. Tuning the values of k will increase / decrease the speed of convergence of the powers. Choosing a very large value for k may achieve faster convergence but the stability of the system becomes susceptible.

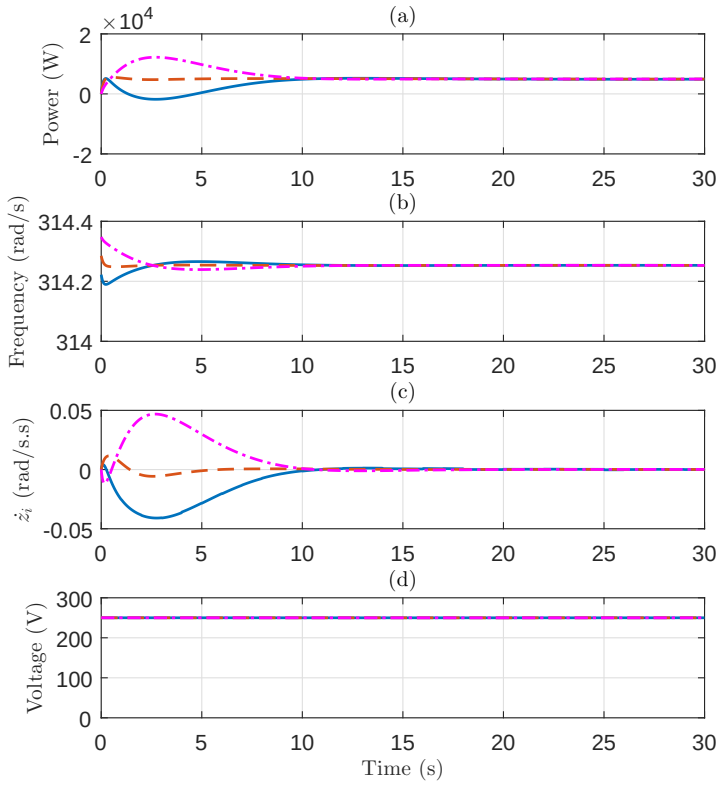

Figure 5.8: Outputs of the system with drifted clocks and $k_i = k = 0.3$. (a) Real power, (b) frequency, (c) $\dot{z}_i$, and (d) Voltage. Inverter at bus 1 is represented by (—), at bus 2 by (- -) and at bus 3 by (-·-).

5.3.1 Reactive power sharing with frequency boost controller

For low voltage microgrids that use reactive power frequency $(Q + \omega)$ boost controllers, we can modify our control law to proportionally share reactive power under the presence of clock drifts as follows:

$$\gamma_i \dot{\delta}_i = \omega^* + n_i(Q_i - Q_i^*) + z_{q,i}$$
$$\gamma_i \dot{Q}_i = -f_{q,i} Q_i + f_{q,i} q_i$$
$$\gamma_i \dot{z}_{q,i} = \ell_i \sum_{j \sim \mathbf{N}_i} (n_i Q_i - n_j Q_j),$$

Table 5.2: Simulation parameters for $(Q+\omega)$ boost control based microgrid.

Parameter	**Value**
V_i	$250V_{rms}$
Z_i, i=2,4	$0.2 + j0.02\ \Omega$ (at ω^*)
Z_i, i=1,3,5	$0.3 + j0.03\ \Omega$ (at ω^*)
Z_{iL}, i=1,2,3	$j12.5\ \Omega$ (at ω^*)
f	10 Hz
n_i	1×10^{-5} Hz/VA
ω^*,Q_i^*	50 Hz, 0 VA

where n_i is the $(Q+\omega)$ boost coefficient, $q_i = B_{ii}V_i^2 - \sum_{k\neq i}|Y_{ik}|V_iV_k\cos(\delta_i - \delta_k + \phi_{ik})$ is the reactive power, Q_i is the filtered reactive power, $f_{q,i}$ is reactive power filter cut-off, $z_{q,i}$ is the integral control variable of the ith inverter and ℓ_i is its integral controller gain. The network set-up and parameters used in this set of simulations are all the same except the resistance and reactance values are interchanged. The integral controller value is chosen to be unity, i.e., $\ell_i = \ell = 1$. The clock drifts are exactly the same as the earlier case. Figures 5.9 (a),(b) represent the response of a microgrid with traditional frequency boost controller and Figures 5.9 (c), (d) represent the response of a modified frequency boost controller. It can be clearly seen that the larger droop coefficient leads to a faster steady state convergence given some frequency deviation is allowed. However the clock drifts still have an impact on reactive power sharing. The modified controller provides accurate power sharing unlike its traditional counterpart. Qualitatively, the analysis of reactive power frequency boost control is carried out in a similar fashion to power frequency droop control.

5.3.2 Comparison with other known works

A few works have considered the power sharing problem in frequency droop microgrids from different perspectives. For example, in [125] the authors discussed a consensus

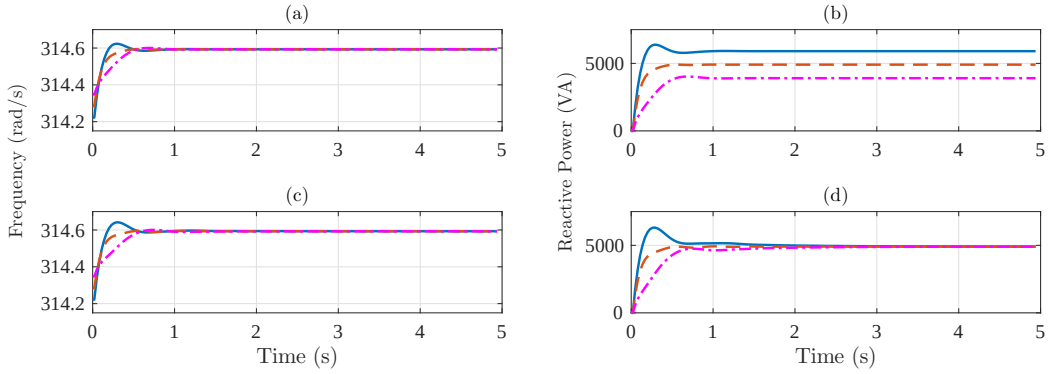

Figure 5.9: Response of a $(Q+\omega)$ boost controlled low voltage resistive microgrid (top) with clock drifts and $\ell_i = \ell = 0$, and (bottom) with clock drifts and $\ell_i = \ell = 1$. (a, c) Frequency, (b, d) reactive power. Inverter at bus 1 is represented by (—), at bus 2 by (- -) and at bus 3 by (-·-).

power sharing problem assuming the presence of accurate clocks and lossless networks. They have used average power sharing correction, where all the converter based generation systems communicate to each other, compute the average and reach to a consensus on the average real or reactive powers using PI control loops. Our technique, on comparison, benefits from the fact that clock affect is made explicit, communication is only nearest neighbour and since we can use our control technique with very small droop coefficients we can simultaneously avoid secondary control. We have also proved stability for lossy microgrid systems that have a high X/R ratio.Some papers used distributed averaging techniques: 1) to correct frequency deviation and provided accurate power sharing, see [134]; and 2) to provide SoC sharing within specified power limits, see [43]; in the absence of clock drifts. However, a recent paper by some co-contributors of [134] has made it explicit that distributed averaging based secondary control techniques may not provide accurate power sharing in the presence of clock drifts, see [74], for which our control technique is especially designed for.

5.4 Summary

We have shown that the power sharing properties of frequency droop controlled inverters are very sensitive to uncertainty in frequencies that arise as a result of clock drifts. We proposed a power sharing controller which based on peer-to-peer communication and improves the stability margin of the system. We presented conditions of stability using Lyapunov's indirect method of stability assessment. We have also shown that our modified droop controller can be used for reactive power sharing in resistive microgrids with minimal changes. Since the structure of the proposed design uses sparse inter-node communications, the modularity and robustness of microgrid design are well preserved.

✧✧✧

6

Modified Angle Droop

UNLIKE frequency droop, angle droop is implemented on a quantity that only has a definition in relative terms, the phase angle. On one hand, clock drifts are crucial is assessing stability and power sharing for angle drop controlled systems however, the disproportion in output impedances can also have a detrimental effect on its power sharing properties. This chapter addresses the angle droop control problem in more detail. The assumptions listed in Section 5.1.1 and models/definitions introduced in Section 3.4 are also applicable to the remainder of this chapter.

6.1 Angle droop and component mismatches

The implementation of angle droop controlled inverter is shown in Figure 6.1. The main aim of the angle droop controller is to provide robust and fair power sharing without imposing a master-slave relationship on the system. Therefore, it is important to understand how power sharing between inverters is achieved using angle droop control.

6.1.1 Two source one load case

From Figure 6.2 and our discussion in Chapter 3, if we assume that the network impedances have a high X/R ratio and the voltage amplitudes are constant, for the (real) power flow

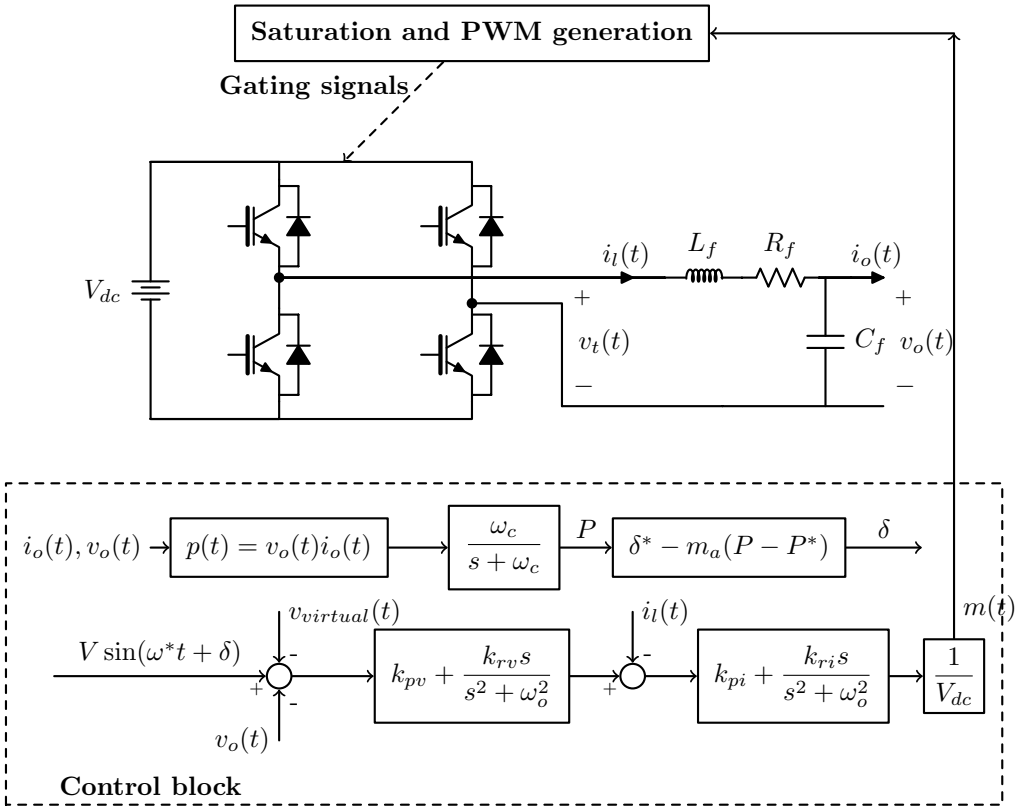

Figure 6.1: Implementation block diagram for a single phase traditional angle droop controlled inverter system.

from the sources to the load

$$P_{i0} \approx V_i V_0 \sin(\delta_i - \delta_0)/X_{i0}.$$

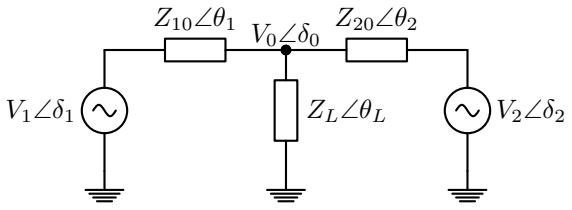

Figure 6.2: Power flow within a system consisting of two voltage sources supplying a common load.

Assuming the difference between the phase angles to be small, we can write:

$$(\delta_i - \delta_0) \cong \chi_{i0} P_{i0} \tag{6.1}$$

In this case, the angle differences between the sources and the load of Figure 6.2 can be given by (6.1) as follows:

$$(\delta_1 - \delta_0) \cong \chi_{10} P_{10}, \tag{6.2}$$

$$(\delta_2 - \delta_0) \cong \chi_{20} P_{20}. \tag{6.3}$$

Assuming that the sources 1 and 2 are operated on angle droop control and also assuming $\delta_i^* = m_i P_i^* = 0$, the angle between the two sources can be represented by :

$$(\delta_1 - \delta_2) \cong m_2 P_{20} - m_1 P_{10}. \tag{6.4}$$

Solving equations (6.2), (6.3) together with (6.4) yields

$$P_{10} \left(\chi_{10} + m_1\right) = P_{20} \left(m_2 + \chi_{20}\right), \tag{6.5}$$

where $\chi_{ij} := X_{ij}/V_i V_j$. It can be seen from (6.5) that only a choice of $m_i \gg \chi_{i0}$ will result in the desired power sharing ratio $m_1 P_{10} \approx m_2 P_{20}$. If $m_i \ll \chi_{i0}$ or if there exists a non-negligible link resistance, then we require a more sophisticated technique to ensure proper power sharing.

6.1.2 Other topologies

The power sharing correction for topologies like those shown in Figures 6.3 and 6.4 is more complex. For the system shown in Figure 6.3 load voltage communication or a central controller based supervision may be used to implement a power sharing correction [92], but such systems are then susceptible to a single point-of-failure. Also this solution is difficult to scale, as any change in the topology requires also a change in the control law. Power sharing between inverters the system shown in Figure 6.4 is:

$$\delta_1 - \delta_2 = \chi_{1a} - \chi_{2a},$$

$$\delta_2 - \delta_3 = \chi_{2b} - \chi_{3b},$$

$$\delta_3 - \delta_4 = \chi_{3c} - \chi_{4c}.$$

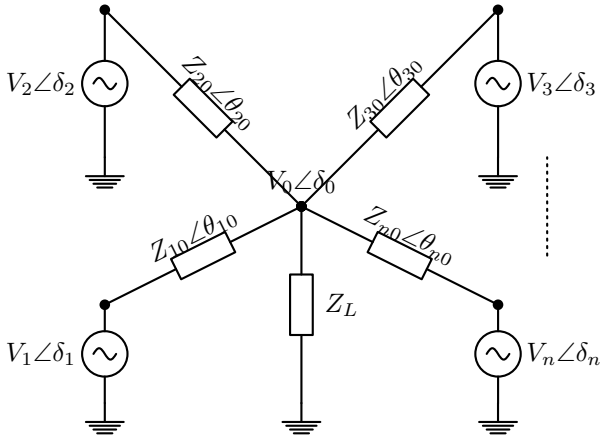

Figure 6.3: Star topology - n angle droop controlled inverter systems supplying a common load Z_L. Each inverter is represented by a phasor $V_i\angle\delta_i$ and is connected to the load ($V_0\angle\delta_0$) through an output impedance $Z_{i0}\angle\theta_{i0}$.

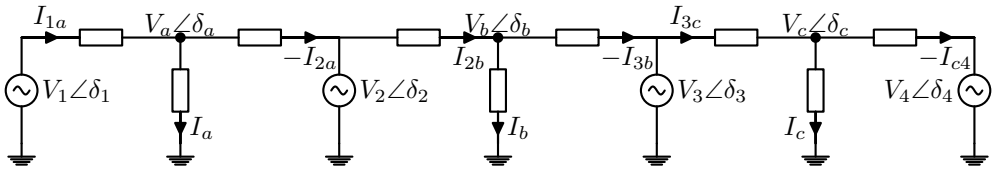

Figure 6.4: An example four inverter three load microgrid.

Given that each source implements angle-droop, we also have

$$\delta_1 - \delta_2 = m_2(P_{2a} + P_{2b}) - m_1 P_{1a},$$
$$\delta_2 - \delta_3 = m_3 P_{3b} - m_2(P_{2a} + P_{2b}),$$
$$\delta_3 - \delta_4 = m_4 P_{4c} - m_3(P_{3b} + P_{3c}).$$

In this case, choosing $\delta_{i,\text{rated}}$ or $m_{i,\text{new}}$ to counteract the power sharing error is prohibitively difficult due to the unavailability of partial power terms. Measuring the partial power terms for $\delta_{i,\text{rated}}$ correction becomes impractical, and the also load voltage feedback method (modifying m_i to $m_{i,\text{new}}$) will not ensure accurate power sharing. A communication based central controller can be used to implement a power sharing correction technique as shown in [94], but such a system is susceptible to a single point-of-failure.

To the best of our knowledge, in the literature no control method using only limited communications can adequately ensure fair power sharing in angle droop controlled systems. Selecting large values for m_i or modifying m_i based on load voltage communication may provide power sharing, but (especially when $X_{ij}/(V_i\,V_j)$ is large) this will erode the stability margin of the microgrid system [92], and hence this is not a practical approach. Also obtaining accurate information on X_{ij} for all branches in a network is difficult.

6.1.3 Effect of clock drift on power distribution

Observe that the implementation of angle droop control requires a common clock signal and the angle measurements are made with respect to a common angular frequency ω^* (50 or 60 Hz for example) [94]. Using the global positioning system (GPS) based time synchronization was presented as a possible solution for time synchronization in [94]. A disadvantage of such design is that the entire network is dependent on an external timing source.

Let us consider how the power sharing between inverters is affected by clock drift. First, define the average frequency in the network as

$$\omega_{avg} = \frac{1}{n}\sum_{i=1}^{n}\omega_i.$$

Over a short period of time, the average frequency can be viewed as the global system frequency, and we rewrite the ith inverter local voltage (3.14) in terms of this average network frequency ω_{avg} as follows,

$$v_i(t) = V_i\cos(\omega_{avg}t + \delta_i'(t)), \tag{6.6}$$

where $\delta_i'(t) = \delta_i + (\omega_i - \omega_{avg})t$ is a time varying phase angle. The short period of time is $\mathcal{O}(1/\epsilon)$ (with ϵ as defined in Section 3.4) and hence it is a reasonably large time interval over which we can consider the stability of the network.

Given any network, we continue our analysis using its Kron reduced form [77]. The active power at the ith inverter, p_i, in the Kron reduced network, using (6.6), is of the form[1]:

$$p_i = G_{ii}V_i^2 + \sum_{k=1,k\neq i}^{n} |Y_{ik}|V_iV_k \sin(\delta_i' - \delta_k' + \phi_{ik}) \tag{6.7}$$

where $Y_{ik} = G_{ik} + jB_{ik}$ is the complex admittance and ϕ_{ik} is the admittance angle between inverters i and k in the Kron reduced network. Refer to Appendix C for more details on Kron reduction method. Recall that the analysis conducted here is with respect to a global reference time t, and a global frequency ω_{avg}.

The sinusoidal terms in p_i are functions of time due to the clock drifts as follows:

$$\begin{aligned}\sin(\delta_i' - \delta_k' + \phi_{ik}) &= \sin((\delta_i + (\omega_i - \omega_{avg})t) \\ &\qquad - (\delta_k + (\omega_k - \omega_{avg})t) + \phi_{ik}), \\ &= \sin(\delta_i - \delta_k + (\omega_i - \omega_k)t + \phi_{ik}).\end{aligned}$$

Since in our setting $(\omega_i - \omega_k) = (\epsilon_i - \epsilon_k)\omega$ is not zero, the power flow p_i (6.7) varies (slowly) with time as a sum of sine functions, each sine function having a small frequency given by the frequency error between two inverters. (Using the data in Table 3.2, observe that the time scale for these power flow variations is in the order of 30 seconds.)

In summary, in order to achieve power sharing, we need a control scheme that can overcome both the line impedance effect and the frequency mismatch effect. To enable such control, and allow the above model over a significant period of time to be valid, we first implement a frequency restoration control to suppress any beating phenomenon caused by frequency differences.

[1]The time argument is neglected for simplicity

6.2 Modified angle droop and stability analysis

Motivated by the robustness and modularity requirements for a microgrid, we make use of inter-node communications only to maintain desired power output and achieve synchronization between inverters.

6.2.1 Frequency control

To facilitate frequency synchronization between inverters and to eliminate any frequency beating phenomena, we propose that each inverter i communicates its measured local frequency ω_i to the neighbouring inverters $j \in \mathbf{N}_i$. This type of control is locally executed. The ith inverter then implements an integral action controller to reduce the frequency drift:

$$\gamma_i \dot{\omega}_i = -\psi_i \sum_{j \in \mathbf{N}_i} (\omega_i - \omega_j), \tag{6.8}$$

where $\psi_i > 0$ is the frequency restoration gain. It can be seen here that the clock drift effect is included using the integrator scaler γ_i.

6.2.2 Power control

In order to facilitate power sharing, we propose that each inverter communicates its output power to all its neighbouring inverters. Inspired by consensus theory [106], we modify the droop equation (3.11) by adding an integral action term $z_i(t)$ as shown in (6.9). The integral action $z_i(t)$ is defined in (6.10).

$$\delta_i = \delta_i^* - m_i \times (P_i - P_i^*) - z_i, \tag{6.9}$$

$$\gamma_i \dot{z}_i = k_i \sum_{j \in \mathbf{N}_i} (m_i P_i - m_j P_j)., \tag{6.10}$$

where k_i is the integral control gain. The integral action serves to enforce power flow sharing, because the equilibrium condition implies power sharing.

6.2.3 Convergence and stability analysis

The modified angle droop control system is a combination of two separate controllers, one to achieve frequency convergence and another to achieve consensus in power sharing. We have the following stability results.

Theorem 6.2.1 (**Frequency Consensus**). *The frequency controller* (6.8) *with individual control gains* $\psi_i > 0$ *achieves frequency consensus irrespective of the remaining system behaviour, provided the communication graph is symmetric and well-connected.*

Proof. First, we rewrite the frequency stabilising controller (6.8) in vector form as

$$\mathbf{\Gamma}\dot{\Omega} = -\Psi\mathbf{L}_c\Omega, \tag{6.11}$$

where $\mathbf{\Gamma} = diag(\gamma_i)$, $\Omega = col(\omega_i)$ and $\Psi = diag(\psi_i)$, and $\mathbf{L}_c$ is the Laplacian matrix associated with the communication structure. Here the communication structure is symmetric and corresponds to a well-connected communication graph, in which case $\mathbf{L}_c$ is positive semi-definite, with a single zero eigenvalue [106]. A steady state $\Omega^s \neq 0$ will be reached exponentially because the state transition matrix $-\mathbf{\Gamma}^{-1}\Psi\mathbf{L}_c$ is negative semi-definite, with a single zero eigenvalue.

The steady state is proportional to the zero-eigenvector of the Laplacian:

$$0_n = -\mathbf{L}_c\Omega^s \iff \Omega^s = \alpha 1_n \iff \omega_i^s = \omega_j^s = \omega_{avg},$$

where 0_n is an n-dimensional vector of all zeros and 1_n is an n-dimensional vector of all 1s. It follows that consensus is reached exponentially fast. □

Remark 6.2.2. *Because* $\mathbf{L}_c$ *is symmetric with* 1_n *as eigenvector associated with its unique zero eigenvalue, it is easily seen that* $\sum_i \frac{\gamma_i}{\psi_i}\omega_i(t)$ *is independent of time. Hence the final averaged frequency, and the consensus of all frequencies, is therefore given by*

$$\omega_{avg} = \lim_{t\to\infty} \omega_i(t) = \frac{\sum_i \frac{\gamma_i}{\psi_i}\omega_i(t)}{\sum_i \frac{\gamma_i}{\psi_i}},\ t \geq 0.$$

It is thus equal to the weighted sum of the original frequencies, weighted according to the ratio of clock drift to the corresponding frequency controller gain.

Given all γ_i are near 1, selecting all $\psi_i = \psi > 0$ is a reasonable choice, which yields

$$\omega_{avg} = \lim_{t\to\infty} \omega_i(t) = \frac{1}{n}\sum_i \omega_i(t)$$

The accuracy of the frequency consensus algorithm depends on the measurement accuracy of the local frequency. Perfectly accurate local frequency measurements will lead to perfect synchronization (6.8). In the presence of clock drift some frequency measurement error cannot be avoided, and the above control law will lead to *almost* frequency stabilisation, with a residual error of the order of the mean measurement error over the network (the larger the network the smaller the residual error). Also, the modified angle droop control, to be proposed in Section 6.2.2 is robust with respect to small inaccuracies in frequency measurement, and hence perfect frequency stabilisation is not required.

Although the power sharing is perturbed by the frequency consensus control action, once frequency consensus is reached, the steady state power distribution (6.7) only depends on the line impedances. As the frequency consensus is guaranteed independent of the power sharing, the power sharing controller can focus on power sharing as if frequency consensus holds.

To model the dynamics of the power controller, assume that the power measurements are obtained as the output of a unity gain, low pass filter, represented by:

$$\gamma_i \dot{P}_i = -f_{p,i} P_i + f_{p,i} p_i, \tag{6.12}$$

where $f_{p,i}$ is the low pass filter cut-off frequency and p_i is the power supplied by (see equation (6.7)) the ith inverter.

Definition 6.2.3. *Define vectors / matrices:*

$$\begin{aligned}
1_n &:= col(1), & \mathbf{P}_a &:= col(p_i), & \mathbf{M} &:= diag(m_i),\\
0_n &:= col(0), & \boldsymbol{\delta} &:= col(\boldsymbol{\delta}_i), & \boldsymbol{\Gamma} &:= diag(\gamma_i),\\
\mathbf{P}_m &:= col(P_i), & \mathbf{V} &:= col(V_i), & \mathbf{K} &:= diag(k_i),\\
\mathbf{P}^* &:= col(P_i^*), & \mathbf{Z} &:= col(z_i), & \mathbf{T} &:= diag(\tau_{p,i}).
\end{aligned}$$

We also introduce a deviation vector associated with every state vector. For example, $\bar{\delta}$ is the deviation vector for the local phase angle vector δ, defined as:

$$\bar{\delta} = \delta - \delta^s, \tag{6.13}$$

where δ^s is the equilibrium vector of phase angles. Similarly deviation vectors are defined for the state vectors $(\bar{\mathbf{P}}_m, \bar{\mathbf{Z}})$ and equilibrium vectors $(\mathbf{P}^s_m, \mathbf{Z}^s)$. The power-angle Jacobian is defined as $\mathbf{L}_n = \dfrac{\partial \mathbf{P}_a}{\partial \delta}|_{\delta^s}$.

Using equations (6.9), (6.10), (6.12) and (6.13) we can obtain the (error) vector dynamics of the closed loop system. The linearized system is given below:

$$(\mathbf{I}_2 \otimes \mathbf{\Gamma}) \begin{bmatrix} \dot{\bar{\mathbf{P}}}_m \\ \dot{\bar{\mathbf{Z}}} \end{bmatrix} = \underbrace{\begin{bmatrix} -f(\mathbf{I}_n + \mathbf{L}_n\mathbf{M}) & -f\mathbf{L}_n \\ k\mathbf{L}_c\mathbf{M} & 0_{n\times n} \end{bmatrix}}_{:=\mathbf{A}} \begin{bmatrix} \bar{\mathbf{P}}_m \\ \bar{\mathbf{Z}} \end{bmatrix} \tag{6.14}$$

For simplicity sake, we assumed equal measurement filter cut-off frequency and equal the integral control gains at all inverters. So we have $\mathbf{T}^{-1} = diag(f_{p,i}) = f\mathbf{I}_n$, and $\mathbf{K} = diag(k_i) = k\mathbf{I}_n$. For properties of matrices $\mathbf{L}_n$ and $\mathbf{L}_c$ see [119] and [106], respectively. The eigenvalues of $\mathbf{A}$ defined in (6.14) are the roots of the equation

$$\det(\lambda_{\mathbf{A}}\mathbf{I}_{2n} - \mathbf{A}) = \det(Q(\lambda_{\mathbf{A}})) \tag{6.15}$$

where $Q(\lambda_{\mathbf{A}}) = \lambda^2_{\mathbf{A}}\mathbf{I}_n + f\lambda_{\mathbf{A}}(\mathbf{I}_n + \mathbf{L}_n\mathbf{M}) + fk\mathbf{L}_n\mathbf{L}_c\mathbf{M}$.

Lemma 6.2.4. *Given the properties of the matrices $\mathbf{L}_n, \mathbf{L}_c$ and $\mathbf{M}$, the matrix product $\mathbf{L}_n\mathbf{L}_c\mathbf{M}$ has a zero eigenvalue and all the remaining eigenvalues have positive real parts. The real parts of the eigenvalues of $\mathbf{I}_n + \mathbf{L}_n\mathbf{M}$ are always positive.*

Proof: The droop coefficient matrix $\mathbf{M}$ is diagonal with strictly positive entries, and hence it is strictly positive definite. The network laplacian $\mathbf{L}_n$ is associated with a strongly connected graph (of the Kron-reduced network) and therefore its non-zero eigenvalues have a strictly positive real part (there exists a zero eigenvalue of geometric multiplicity one) [119]. We also assume that any vector $v \in \mathbb{C}^n$ and $\mathbf{L}_c\mathbf{M}v(\neq 0_n)$ is not in the null space of $\mathbf{L}_n$ which is reasonable since the null space and the image of any

matrix are orthogonal subspaces. The second part of the claim comes from the fact that the zero eigenvalue of $\mathbf{L}_n\mathbf{M}$ disappears on addition with the identity matrix $\mathbf{I}_n$. □

Theorem 6.2.5 (**Power Sharing**). *Considering that the frequency controller* (6.11) *stabilizes the frequency, let* $\mu_i(= a_i + jb_i)$ *be the ith eigenvalue of the matrix* $(\mathbf{I}_n + \mathbf{L}_n\mathbf{M})$ *and* $\rho_i(= x_i + jy_i)$ *be the ith eigenvalue of matrix* $(\mathbf{L}_n\mathbf{L}_c\mathbf{M}), \quad i = 1, 2, \ldots, n$. *We define* $\sigma := \frac{k}{f}$, $U_i := a_i^2 - b_i^2 - 4\sigma x_i$, *and* $W_i := 2a_ib_i - 4\sigma y_i$. *Then, the linearized closed loop system* (6.14) *is stable for appropriate choices of* $f, 0 < k \ll \min(\frac{1}{m_i})$, $0 < m_i \ll 1$ *that satisfy the condition:*

$$\frac{W_i^2}{4} + U_i < 1 \tag{6.16}$$

Proof. First, we prove that power sharing criterion is satisfied. The integral consensus term of (6.10) is a negative feedback term with the matrix $\mathbf{L}_c$ governing its state evolution. Consequently, in steady state, we have:

$$0_n = k\mathbf{L}_c\mathbf{M}\mathbf{P}_m^s \iff \mathbf{M}\mathbf{P}_m^s = \beta 1_n \iff m_iP_i^s = m_jP_j^s,$$

where 0_n is a n-dimensional vector of zeros, 1_n is a n-dimensional vector of ones and β is a constant depending on aggregate inverter loading (load + line loss) and irrespective of line impedance distribution. Secondly, to prove the system stability, we analyze the characteristic polynomial $\det(Q(\lambda_\mathbf{A}))$ defined in (6.15). Recall that from Lemma 6.2.4, the $\Re\{v^*\mathbf{L}_n\mathbf{L}_c\mathbf{M}v\} \geq 0$ and $\Re\{v^*(\mathbf{I}_n + \mathbf{L}_n\mathbf{M})v\} > 0$ for any vector $v \in \mathbb{C}^n$ with $v^*v = 1$.

For any vector v with $v^*v = 1$ we have will then have

$$v^*Q(\lambda_\mathbf{A})v = \lambda_\mathbf{A}^2 + f\lambda_\mathbf{A}v^*(\mathbf{I}_n + \mathbf{L}_n\mathbf{M})v + fkv^*\mathbf{L}_n\mathbf{L}_c\mathbf{M}v.$$

Let v_i be the right eigenvector of $Q(\lambda_\mathbf{A})$, such that $v_i^*Q(\lambda_\mathbf{A})v_i = 0$. That implies

$$\lambda_\mathbf{A}^2 + f\lambda_\mathbf{A}v_i^*(\mathbf{I}_n + \mathbf{L}_n\mathbf{M})v_i + fkv_i^*\mathbf{L}_n\mathbf{L}_c\mathbf{M}v_i = 0. \tag{6.17}$$

With eigenvalue definitions introduced in the statement of theorem (6.2.5) the above equation becomes

$$\lambda_{\mathbf{A},i}^2 + f\lambda_{\mathbf{A},i}\mu_i + fk\rho_i = 0.$$

The eigenvalues of $\mathbf{A}$ are the roots of the above equation for $i = 1, 2, \ldots, n$. From Lemma 6.2.4 we conclude that $\mu_1 = 1$ and $\rho_1 = 0$ can be identified as eigenvalues associated with the second and the last term in (6.17). Moreover, $\varpi \mathbf{M}^{-1} 1_n, \varpi \in \mathbb{R} \setminus \{0\}$ is the eigenvector associated with these eigenvalues.

Therefore, we conclude that the first two eigenvalues of the matrix $\mathbf{A}$ are

$$\lambda_{\mathbf{A},1_{1,2}} = 0, -f.$$

The remaining eigenvalues are obtained by solving

$$\lambda_{\mathbf{A},i}^2 + f\lambda_{\mathbf{A},i}\mu_i + fk\rho_i = 0, \quad i = 2, 3, \ldots, n$$

Since the above equation is quadratic, the solutions can be written as

$$\lambda_{\mathbf{A},i} = \frac{f}{2}\left[-1 \pm \sqrt{\mu_i^2 - \frac{4k\rho_i}{f}}\right].$$

As introduced in the Theorem 6.2.5 statement, we can define

$$\sqrt{U_i + jW_i} = \sqrt{\mu_i^2 - \frac{4k\rho_i}{f}}$$

The roots of $\sqrt{U_i + jW_i}$ take the form $\pm(u_i + jw_i)$ [119]. Here, we need u_i to be less than 1 to ensure that the (non-zero) roots always have a negative real part, which can be achieved by designing an integral control gain k according to (6.16). Since traditional angle droop controller is based on small angle approximations (truncated Taylor series expansion) of the sine function, it is good practice to choose small values of k typically much less than the smallest reciprocal of the droop coefficients, i.e., $k \ll \min(1/m_i)$ to avoid unnecessary oscillations. □

6.3 Simulations and discussion

We present a simulation example to illustrate the performance of the stabilizing controller; a microgrid consisting of three single phase inverters operating in parallel supplying a common load, a system in a star topology as discussed in Section 6.1. The

parameters of the system are given in Table 6.1. They are informed by [131]. It is worth observing here that the main network impedances are inductive. If these impedances were not inductive, the suggested angle droop controller would be inappropriate since a higher X/R ratio is required. We remark that when this is not the case, virtual impedance control at the inverter can be used to enforce this condition. The simulations are implemented in MATLAB SimPowerSystems. Several scenarios with different controllers are simulated.

Table 6.1: Simulation parameters for $(P-\delta)$ droop control based microgrid.

Parameter	**Value**
n	3
$[R_1 \;\; R_2 \;\; R_3]$	[0.02 0.04 0.03] Ω
$[X_1 \;\; X_2 \;\; X_3]$	[0.2 0.4 0.3] Ω (at ω^*)
m_i	$1 \times 10^{-6} deg/W$
V_i^*	240 V_{rms}
ω^*	$2\pi 50\ rad/s$
δ_i^*	0 rad
R_0	16.6 Ω
$\mathbf{L}_c$	$[1\ -1\ 0; -1\ 2\ -1; 0\ -1\ 1]$

Case 1 : Inverters with identical clocks and disproportionate output impedances

The three inverters are operating at the rated frequency, $\omega = \omega^* = 100\pi$rad/s. There are no clock drifts: $\gamma_i = 1$. The evolution of the output power supplied by the inverters in this scenario is given by Figure 6.5(a). It can be clearly seen that the power supplied by each inverter depends on its output impedance as discussed in section 6.2. As is to be expected, the inverter with the largest per-unit output impedance supplies the least power.

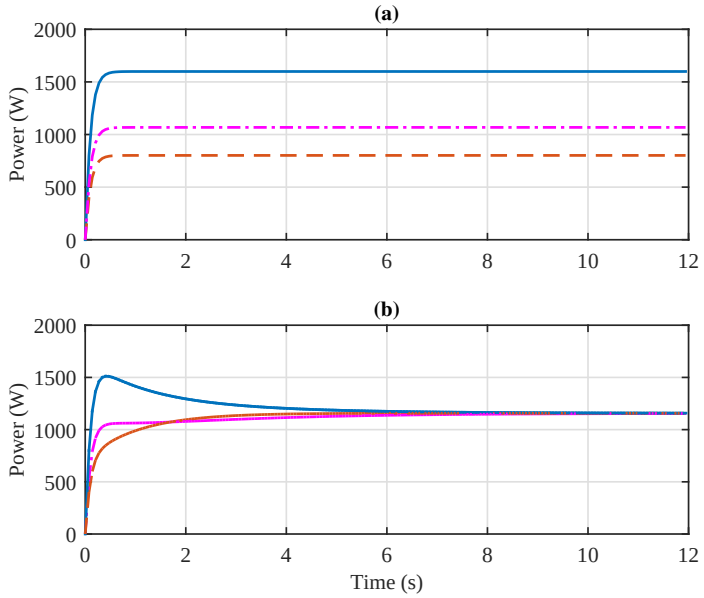

Figure 6.5: Active power sharing between inverters in (a) traditional angle droop (b) proposed angle droop control with inverters operating at ideal frequencies; – Inverter 1, - - Inverter 2, -.- Inverter 3.

Case 2: Inverters with identical clocks, disproportionate output impedances and power consensus controls

In this case, the rated frequency, ω^* at each inverter remains at 50 Hz. Clock drifts are not present. Only the proposed power consensus controllers are now active. Figure 6.5(b) shows changes in the active power output of each inverter over a time period of 12 seconds. The power consensus time constant is about 1s. It is clearly seen that power sharing is restored. The integral controller ensures zero power sharing error in this case, irrespective of the disparate per-unit output impedances.

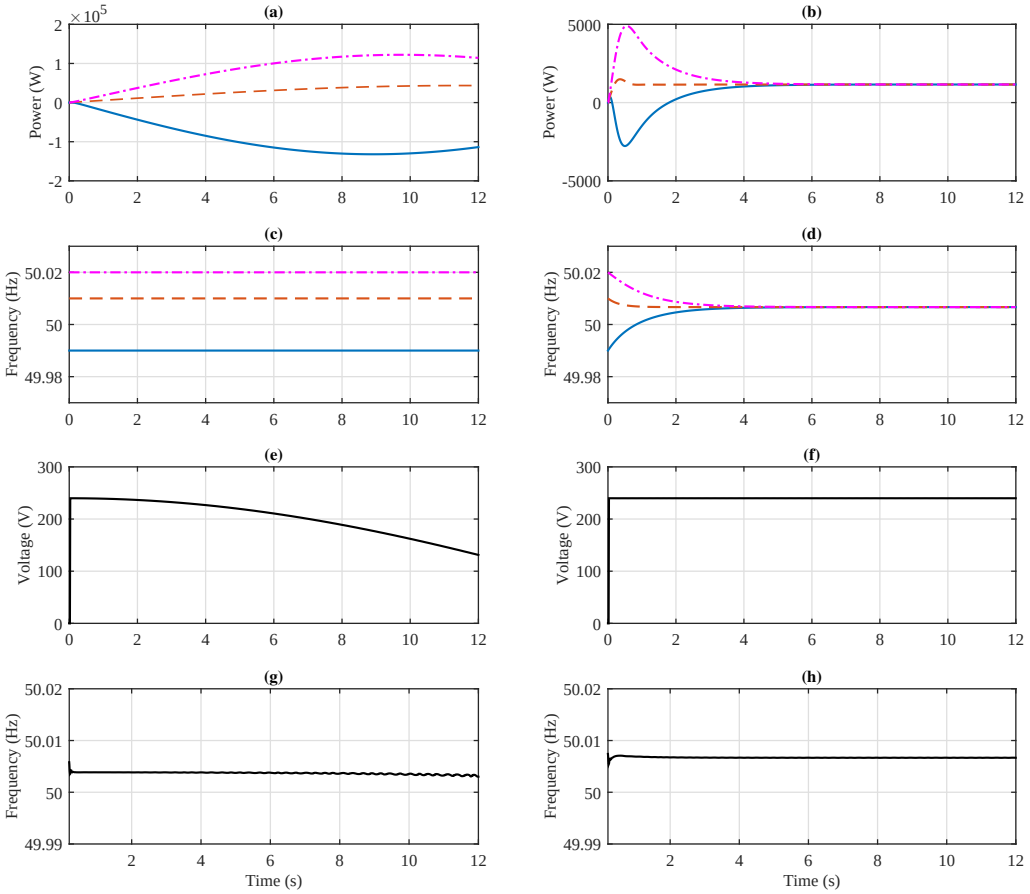

Figure 6.6: (left) The response of the network with frequency drifts and without consensus control; (right) The response of the network with frequency drifts and with proposed consensus control, $\psi_i = \psi = 1$ and $k_i = k = 10^3$. (a,b) Inverter output active power (c,d) inverter output voltage frequency (e,f) rms load voltage (g,h) load frequency; '–' Inverter 1, '- - ' Inverter 2, '-.-' Inverter 3, '–' Load.

Case 3: Inverters with non-identical clocks and disproportionate output impedances

In this case, the rated frequencies of the inverters remain at 50 Hz. Time invariant clock drifts are present. The relevant drift parameters are $\eta_1 = -0.01$ Hz, $\gamma_1 = 1.0002$,

$\eta_2 = 0.01$ Hz, $\gamma_2 = 0.9998$ and $\eta_3 = 0.02$ Hz, $\gamma_3 = 0.9996$.

The output power and the local frequency of each inverter is shown in 6.6(a) and 6.6(c), respectively. When these clock drift are not compensated for, the injected powers start drifting apart. That is the microgrid is unstable. Indeed notice that in this case one of the inverters actually sink power. Four quadrant inverters may be able to cope with this situation, but simple inverters will not allow such large deviations, and their current protection will lead to inverter shut-down, and hence microgrid failure. Moreover, as shown in figure 6.6(e), the voltage stability of the microgrid has also been compromised. Clearly, there is no stable network frequency (shown in Figure 6.6(g)) in the microgrid.

Case 4: Inverters with non-identical clocks, disproportionate output impedances and consensus controls

While the parameters are the same as in the previous case, in this scenario both the frequency and power consensus controls are active and chosen according to the criteria provided. In spite of the clock drift, it is clearly shown in Figure 6.6(b) that power sharing is achieved. During the transient phase, the power sharing error is still significant; further work is required to avoid large transient deviations in power sharing, and to respect the operational envelope of the inverters. Once the frequency consensus control delivers a consensus frequency, as shown in Figure 6.6(d) the power sharing is quickly restored (the time constant was chosen rather large to illustrate the effect of the frequency consensus control). We also observed that the power sharing controller alone can counteract small frequency differences in terms of stability of output power.

6.3.1 Comparison with other known works

Comparing modified angle droop with some known accurate power sharing techniques, for example [43, 124, 125], highlights the differences in control application to achieve a similar objective. All the papers mentioned above applied distributed averaging techniques using a dedicated communication channel. However, unlike either of them, the

angle droop is applied directly to control the phase angle of converter based generation systems to achieve power sharing. Methods like those used in [42] where one pulse per second (1PPS) based GPS clock correction can avoid the frequency control loop but the power sharing controller is still required to achieve accurate power sharing under the effect of disproportionate impedances.

6.4 Summary

We have shown that the angle droop controller is very sensitive to clock drifts. Assuming the frequency drifts are constant over a short transient period, we introduced a combination of stabilizing controllers that ensure the desired operation in an angle droop controlled microgrid. The proposed framework is based on local peer-to-peer communication to achieve first a consensus in the system frequency and then to restore the desired power sharing between the inverters. Simulation results are presented to illustrate the control ideas.

✧✧✧

Part V

CONCLUSION

7

Conclusion and future work

7.1 Conclusion

RENEWABLE energy microgrids based on power electronics are set to revolutionize the electricity industry in the very near future. We have addressed some important research challenges that support this evolution in two parts:

1. **Sizing and operating storage systems in master-slave microgrids**- We have used linear models of a radial master-slave microgrid network and incorporated the battery operation and sizing variables as decision variables in a suitable optimization algorithm. By solving this optimization as an MILP, we have addressed an implicit design issue of battery size availability. The result of the optimization problem estimates the size, position and temporal operation profiles of batteries which can satisfy all the network constraints and reduce the total cost of microgrid operation at the same time. Applicability of the battery charging and discharging decisions obtained from optimization is reliant on accuracy of forecast information in demand and generation. To cope with the uncertainty that arises as a result of prediction errors, we have used a Monte-Carlo simulation type analysis to find the solution that satisfies the constraint set.

2. **Controlling parallel converter based generation** - Given microgrids are en-

ergy and power limited, power/energy sharing is the main aspect analyzed in our work. It has been shown that practical implementation variables like impedance distribution and clock mismatches have an impact on the system stability and power sharing between droop controlled converters in a microgrid. We proposed methods that can achieve stability and desired power sharing behavior in the presence of such mismatches. Our design is consistent with the microgrid definitions of being scalable and modular. The robustness of multi-master microgrids is not affected by our modifications thereby allowing plug-n-play operation of microgrid sources. We have developed conditions for stability in terms of network parameters using Lyapunov's indirect method. Although network information is required for finding the absolute bounds on stability, we indicate that we can stabilize the microgrid with approximate network information.

7.2 Future research

- **Battery sizing in non-unity power factor networks-** In Chapter 4, the model used in the optimization problem is easily extendible to AC networks that have a power factor close to unity. However, for networks that have a power factor different from unity the model does not completely capture all the dynamics within the network. This requires further research.

- **Modelling microgrids and communication-** Microgrid modelling carried out in this thesis has considered only constant impedance loads as is common in the present literature. However, some works [136], [87] used constant power loads in their microgrid models. Both these methods have their own advantage / drawbacks and these have been pointed out in [18]. Developing on this, an approach that can integrate all load types into the model would be ideal for the microgrid research. In future research it would be desirable to consider a greater variety of loads. Moreover, here, as in most part of the literature we did not discuss microgrid

operations under fault conditions, for safety and regulatory compliance, fault conditions and fault response in the microgrid has to be analyzed, and the supervisory control has to be designed such that the microgrid remains safe under fault conditions in the microgrid. Moreover, communications generally introduce a delay in the dynamical system modelling. It will be important to see how communication delays impact the stability of microgrids under clock drifts. For example, a reasonable method would be to model the microgrid as a system of delayed differential equations (DDEs) as shown in [31].

- **Frequency restoration through secondary control-** An important functionality of microgrids is to operate when connected to the grid, which means transition to grid-connected mode requires a grid synchronization control as discussed in Chapter 3. There is a huge subset of microgrid literature that discusses this aspect, however in the presence of clock mismatches, some local techniques or distributed averaging controller [136] might not work as well as they do in networks without clock mismatches [75]. The approach we have used in our modified droop controllers is readily extendible to grid synchronization controls with very simple modifications.

- **Dynamics of voltage controllers-** In this thesis, we have not considered voltage mismatches and any controllers that regulate the voltage amplitude based on feedback. As remarked in [162], although voltage mismatches are not as critical as clock mismatches they would still have an impact on reactive power sharing and (indirectly) stability. Therefore, further research should address voltage regulation.

✧✧✧

Part VI

APPENDIX

Appendix A

Stationary and synchronous frames

The inverter control systems are implemented in either $\alpha\beta$ frame or dq frame to transform the three-phase variables. These transformations simplify the control design by converting the three-phase system into two subsystems and also preserve the coupling between the three phase quantities. Consider the balanced three phase system,

$$\begin{aligned} f_a(t) &= \hat{f}cos(wt + \theta_0) \\ f_b(t) &= \hat{f}cos(wt + \theta_0 - \frac{2\pi}{3}) \\ f_c(t) &= \hat{f}cos(wt + \theta_0 - \frac{4\pi}{3}) \end{aligned}$$

The space phasor form of this system is defined as

$$\vec{f}(t) = \frac{2}{3}\left[e^{j0}f_a(t) + e^{j\frac{2\pi}{3}}f_b(t) + e^{j\frac{4\pi}{3}}f_c(t)\right] = \hat{f}e^{j(wt+\theta_0)} \tag{A.2}$$

A.1 Stationary reference frame

The $\alpha\beta$ representation of A.2 is given by

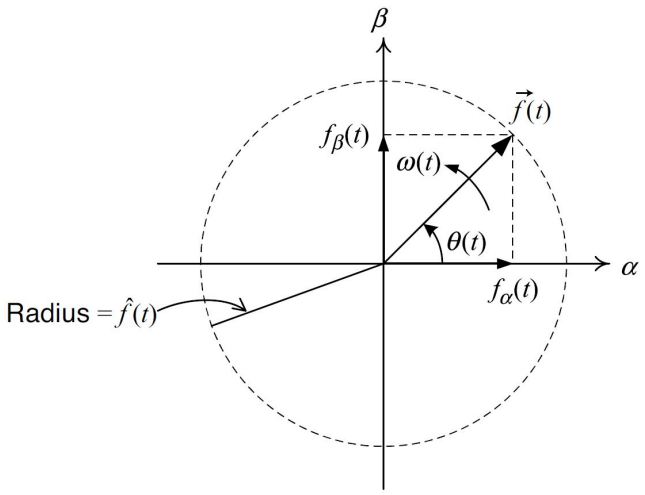

Figure A.1: Space phasor representation in $\alpha\beta$ frame.

$$\vec{f}(t) = f_\alpha(t) + j f_\beta(t) \tag{A.3}$$

Computing the real and imaginary parts of equations A.2 and A.3 we get

$$\begin{bmatrix} f_\alpha(t) \\ f_\beta(t) \end{bmatrix} = \frac{2}{3} \begin{bmatrix} 1 & -\frac{1}{2} & -\frac{1}{2} \\ 0 & \frac{\sqrt{3}}{2} & -\frac{\sqrt{3}}{2} \end{bmatrix} \begin{bmatrix} f_a(t) \\ f_b(t) \\ f_c(t) \end{bmatrix}$$

Figure A.1 shows that the $\alpha\beta$ frame projections of a space phasor [158]. It can be seen that f_α and f_β are sinusoidal functions of amplitude $\hat{f}$ and angular frequency ω. Instantaneous power in $\alpha\beta$ frame is give by

$$P = \frac{3}{2}\left[v_\alpha(t) i_\alpha(t) + v_\beta(t) i_\beta(t)\right]$$
$$Q = \frac{3}{2}\left[-v_\alpha(t) i_\beta(t) + v_\beta(t) i_\alpha(t)\right]$$

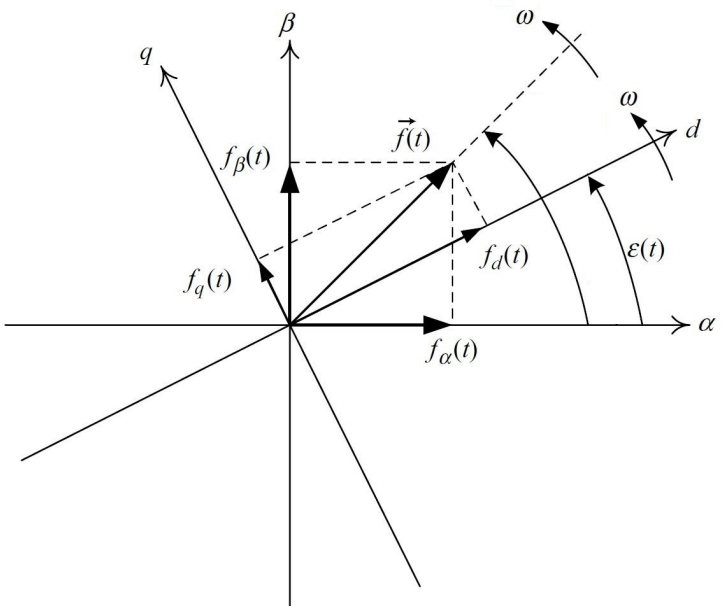

Figure A.2: Space phasor representation in $\alpha\beta$ frame and dq frame .

A.2 Synchronous reference frame

The dq representation of A.2 is given by

$$f_d + jf_q = [f_\alpha(t) + jf_\beta(t)]\, e^{-j\varepsilon(t)}$$

The transformation from $\alpha\beta$ frame to dq frame is given by

$$\begin{bmatrix} f_d(t) \\ f_q(t) \end{bmatrix} = \begin{bmatrix} \cos\varepsilon(t) & \sin\varepsilon(t) \\ -\sin\varepsilon(t) & \cos\varepsilon(t) \end{bmatrix} \begin{bmatrix} f_\alpha \\ f_\beta \end{bmatrix}$$

and abc frame to dq frame is give by

$$\begin{bmatrix} f_d(t) \\ f_q(t) \end{bmatrix} = \frac{2}{3} \begin{bmatrix} \cos\varepsilon(t) & \cos\left[\varepsilon(t) - \frac{2\pi}{3}\right] & \cos\left[\varepsilon(t) - \frac{4\pi}{3}\right] \\ \sin\varepsilon(t) & \sin\left[\varepsilon(t) - \frac{2\pi}{3}\right] & \sin\left[\varepsilon(t) - \frac{4\pi}{3}\right] \end{bmatrix} \begin{bmatrix} f_a(t) \\ f_b(t) \\ f_c(t) \end{bmatrix}$$

Figure A.2 represents the space phasor in $\alpha\beta$ and dq frames [158]. For $\varepsilon(t) = \omega t + \theta_0$, the time varying ac quantities f_α and f_β are transformed into time-independent dc

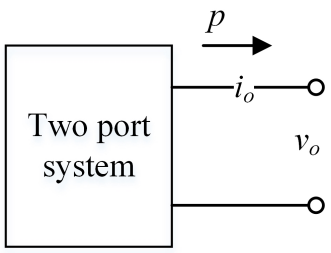

Figure A.3: Power flow in a two-port network

quantities f_d and f_q. Instantaneous power in dq frame is give by

$$P = \frac{3}{2}\left[v_d(t)i_d(t) + v_q(t)i_q(t)\right]$$
$$Q = \frac{3}{2}\left[-v_d(t)i_q(t) + v_q(t)i_d(t)\right]$$

A.3 Power calculation methods

A.3.1 Low-pass filter method

A two-port system working with sinusoidal signals is shown in Figure A.3. Output power of such a system can be measured instantaneously using:

$$p(t) = v_o(t)i_o(t).$$

This term, $p(t)$ will have double frequency oscillating term and also has a non-zero mean for non-zero current, $i(t)$. It is passed through a low pass filter of a time constant, say τ_p to obtain the average power, P_m. This is represented by:

$$\tau_p \frac{d}{dt} P_m(t) = -P_m(t) + p(t).$$

A.3.2 Synchronous integrator method

In this method, the power is measured using average integrator for each cycle [131]:

$$P_m = \frac{1}{T}\int_0^T v_o(t)i_o(t)dt,$$

where T is the period of the sinusoidal voltage, $v_o(t)$. Refer to [158] for more information on transformation frames and power calculation methods.

Appendix B

Simulation model of an inverter

Following the design procedure introduced in Chapter 2, here we implement the single phase inverter in a simulation platform. As shown in Figure 2.19, the dual loop voltage controller has parameter which are given in Table B.1. Figure B.1 shows a simulation block diagram which is implemented in MATLAB. In the simulation, the inverter designed using parameters in Table B.1 is driving a resistive load $R_o = 16.6\Omega$ through a line impedance $L_o = 1.8$mH. The output voltage is shown in Figure B.2 (top). As one can observe, the sinusoidal reference waveform is tracked accurately within a few cycles. The output current is shown in Figure B.2 (bottom). The harmonic content (THD) in voltage output is in the order of 2% and that in current output is in the order of 4%.

Table B.1: Parameters used in implementation of a single phase DC AC inverter.

Parameter	V_{dc}	f_{sw}	L_f	C_f	V_i	k_{pi}	k_{pv}	k_{ri}	k_{rv}	ω_0
Value	380V	10kHz	1.8mH	25μF	250Vrms	0.7	0.35	100	400	50Hz

The implementation code in C within the *control block* in Figure B.1 is as follows:

```
#include <Stdlib.h>
#include <String.h>
#include <math.h>
#define pi         3.14159265358979323846264338327 95
```

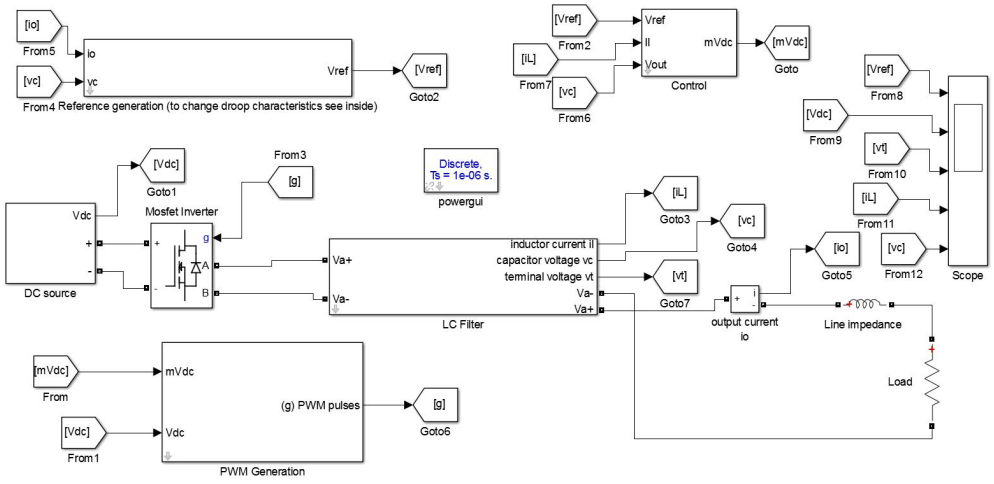

Figure B.1: Implementation of a single phase inverter in MATLAB SimPowerSystems.

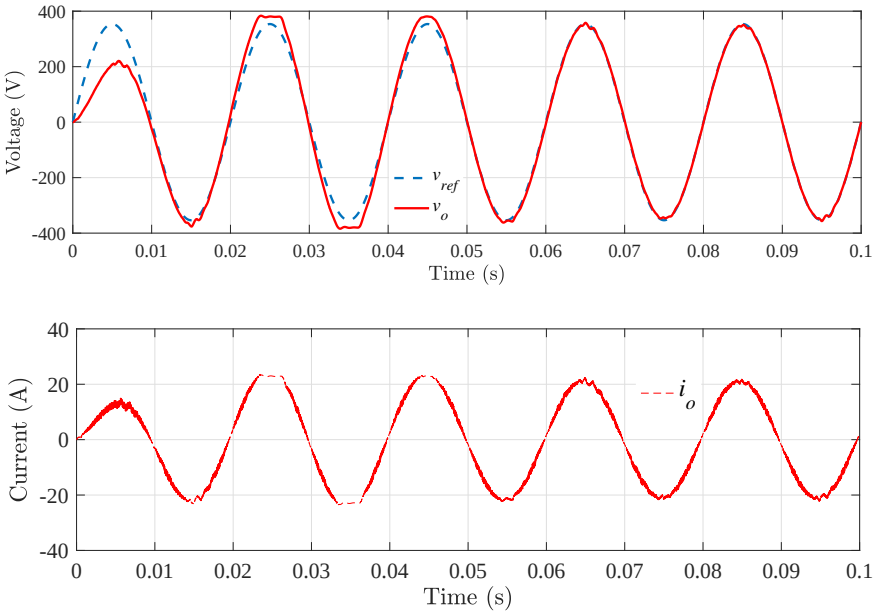

Figure B.2: (top) Output voltage vs reference voltage, and (bottom) Output current of the single phase inverter.

```
#define sqrt2      1.41421356237309504880168872420969
double V = 0.0; // peak voltage
double delta = 0.0; // phase angle
double f = 0.0; // frequency
double vout = 0.0; // output voltage
double iout = 0.0; // output current
double vref = 0.0; // reference voltage
double verr = 0.0; // error voltage
double ierr = 0.0; // error current
double iref = 0.0; // reference current
double kpv = 0.35; // propotional gain voltage
double krv = 400; // resonant gain voltage
double uv = 0.0; // voltage controller
double xv = 0.0;
double y1v = 0.0;
double yv = 0.0;
double w = 2*pi*50; // resonant frequency
double kpi = 0.7; // propotional gain current
double kri = 100; // resonant gain current
double ui = 0.0;// current controller
double xi = 0.0;
double y1i = 0.0;
double yi = 0.0;
double fnom = 50.0;
void SimulationStep(
double t, double delt, double *in, double *out,
int *pnError, char * szErrorMsg,
void ** reserved_UserData, int reserved_ThreadIndex, void * reserved_AppPtr)
{
//reading values
V = (double)(in[0]);
vout = (double)(in[1]);
iout = (double)(in[2]);
```

```
vdc = (double)(in[3]);
//Reference generation
delta += fnom*delt;
vref = V*sin(2*pi*delta);
verr = vref -vout;
// Voltage PR Controller
uv = verr*kpv + xv + yv;
xv += verr*krv*delt;
y1v += (verr*kpv - uv)*w*w*delt;
yv += y1v*delt;
iref = uv;
ierr = iref -iout;
// Current PR Controller
ui = ierr*kpi + xi + yi;
xi += ierr*kri*delt;
y1i += (ierr*kpi - ui)*w*w*delt;
yi += y1i*delt;
m = ui;
out[0] = m/vdc; // to PWM generation block
}
```

For droop controlled inverters, there are modifications that had to be done to the *reference generation* block in Figure B.1. This part of the C code only is given here:

```
p = vout*iout; // power calculation
P += -(P-p)*fc*delt; // low pass filter
f = fnom - mi*(P); // droop controller with zero nominal power
//generating reference waveform
delta += f*delt;
vref = V*sin(2*pi*delta);
```

Output power and frequency of a frequency droop controller inverter with droop coefficient $m = 10^{-5}$ Hz/W and power measured using the low pass filter methd (c.f. Section

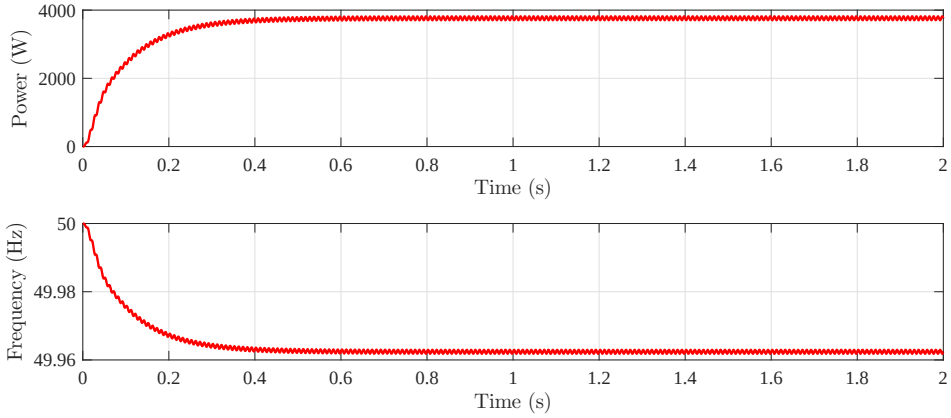

Figure B.3: (top) Output power, and (bottom) output frequency of a single phase frequency droop controlled inverter.

A.3.1) with $f_p = 5$Hz is shown in Figure B.3 (top) and Figure B.3 (bottom), respectively.

Appendix C

Kron reduction and power flow in an electrical network

Analysis of a system with constant impedance loads is simplified by using a Kron-reduced network form. The variations in frequency will present some difficulties in the formulation of Kron-reduced networks. Therefore, we assume that the frequency differences between systems vanish with time and are very close to the nominal. We formulate the network impedance in terms of nominal frequency. In the following section, we briefly present the network reduction process [77].

Let the network have n source buses [numbered 1 to n] and m constant impedance load buses [numbered $(n+1)$ to $(n+m)$]. The connection between buses is via line impedances $\hat{Y}_{ij} = \hat{G}_{ij} + j\hat{B}_{ij}, \quad i,j = 1,2,\ldots\ (n+m)$. Observe that in the absence of a common frequency, the power flow model partially breaks down due to the dependence of the term $\hat{B}_{ij}$ on the frequency. This has not been discussed in literature (to the best of our knowledge). Neglecting this fact, the absolute value of admittance is $|\hat{Y}_{ik}| = \sqrt{\hat{G}_{ik}^2 + \hat{B}_{ik}^2}$ and the admittance angle is $\hat{\phi}_{ik} = \arctan(\frac{\hat{B}_{ik}}{\hat{G}_{ik}})$. The admittance matrix representation of the given network will be of the form:

$$I = \hat{Y}V$$

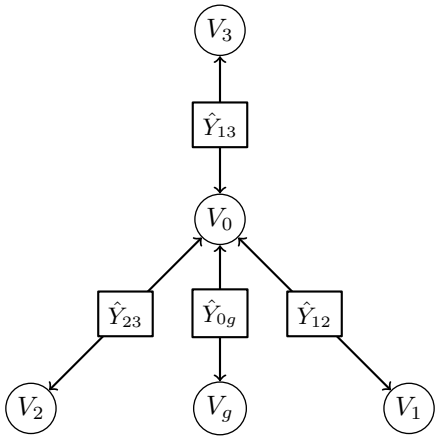

Figure C.1: A star connected network with voltage sources V_1, V_2 and V_3 (all measured with respect to ground V_g) supplying a constant impedance load $\hat{Y}_{0g}$.

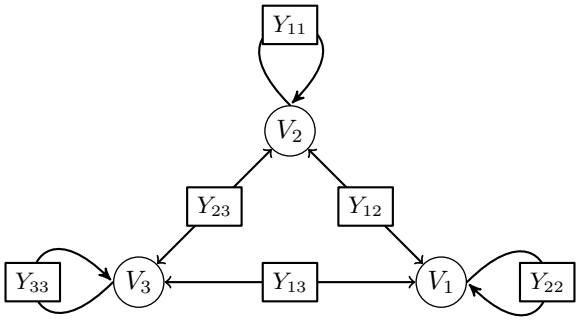

Figure C.2: Kron reduced network equivalent of Figure C.1.

Using Kron reduction the load nodes can be eliminated by replacing $\hat{Y}_{ij}$ by Y_{ij} as follows:

$$Y_{ij} = \hat{Y}_{ij} - \frac{\hat{Y}_{ik}\hat{Y}_{kj}}{\hat{Y}_{kk}}, \qquad i, j = 1, 2, \ldots, n \text{ and } j \neq k$$

where the absolute values of impedance is $|Y_{ik}| = \sqrt{G_{ik}^2 + B_{ik}^2}$ and the impedance angle is $\phi_{ik} = \arctan(\frac{B_{ik}}{G_{ik}})$. The reduced system is discounted of all the load nodes and is of the form:

$$I = YV$$

An example of Kron reduction is shown in Figures C.1 and C.2. The Kron reduced network in Figure C.2 is discounted of the single load node as shown. The active power flowing from the ith source in a Kron reduced network (see [77] for details) can subsequently be given as:

$$p_i = G_{ii}V_i^2 + \sum_{k \neq i} |Y_{ik}|V_iV_k \sin(\delta_i - \delta_k + \phi_{ik}),$$

where $(\delta_i - \delta_k)$ is the difference between the voltage phase angles of inverters i and k at a common frequency. More details on Kron reduction can be found in [36].

Part VII

BIBLIOGRAPHY

Bibliography

[1] ABB, "Energy Efficiency in the Power Grid," https://www.nema.org/Products/Documents/TDEnergyEff.pdf, 2007, [Online; last accessed 28-January-2016].

[2] A. M. A. K. Abeygunawardana and G. Ledwich, "Estimating benefits of energy storage for aggregate storage applications in electricity distribution networks in queensland," in *IEEE Power Energy Society General Meeting, 2013*, July 2013, pp. 1–5.

[3] V. Agelidis, P. Ziogas, and G. Joos, ""Dead-band" PWM switching patterns," *IEEE Transactions on Power Electronics*, vol. 11, no. 4, pp. 522–531, Jul 1996.

[4] B. Aksanli and T. Rosing, "Optimal battery configuration in a residential home with time-of-use pricing," in *IEEE International Conference on Smart Grid Communications (SmartGridComm), 2013*, Oct 2013, pp. 157–162.

[5] H. Alharbi and K. Bhattacharya, "Optimal sizing of battery energy storage systems for microgrids," in *IEEE Electrical Power and Energy Conference (EPEC), 2014*, Nov 2014, pp. 275–280.

[6] I. Alsaidan, A. Khodaei, and W. Gao, "Distributed energy storage sizing for microgrid applications," in *EEE/PES Transmission and Distribution Conference and Exposition (T D), 2016*, May 2016, pp. 1–5.

[7] M. Andreasson, H. Sandberg, D. Dimarogonas, and K. Johansson, "Distributed integral action: Stability analysis and frequency control of power systems," in

IEEE 51st Annual Conference on Decision and Control (CDC), 2012, Dec 2012, pp. 2077–2083.

[8] M. Andreasson, D. V. Dimarogonas, H. Sandberg, and K. H. Johansson, "Distributed PI-control with applications to power systems frequency control," in *American Control Conference, 2014*. IEEE, 2014, pp. 3183–3188.

[9] P. Asmus, A. Lauderbaugh, and M. Lawrence, "Market Data: Microgrids - Executive Summary by Navigant Research," http://www.navigantresearch.com/wp-assets/uploads/2013/03/MD-MICRO-13-Executive-Summary.pdf, 2013, [Online; accessed 30-August-2013].

[10] ——, "Microgrid Deployment Tracker 2Q13: Commercial/Industrial, Community/Utility, Institutional/Campus, Military, and Remote Microgrids: Operating, Planned, and Proposed Projects - Executive Summary by Navigant Research," http://www.navigantresearch.com/wp-assets/uploads/2013/05/TR-MGDT-2Q13-Executive-Summary.pdf, 2013, [Online; accessed 30-August-2013].

[11] P. Asmus and C. Wheelock, "Market Data: Distributed Energy Systems for Campus, Military, Remote, Community, and Commercial and Industrial Power Applications: Market Analysis and Forecasts - Executive Summary by Pike Research," https://www.navigantresearch.com/wordpress/wp-content/uploads/2012/01/MICRO-12-Executive-Summary.pdf, 2012, [Online; accessed 30-August-2013].

[12] R. Atia and N. Yamada, "Sizing and analysis of renewable energy and battery systems in residential microgrids," *IEEE Transactions on Smart Grid*, vol. 7, no. 3, pp. 1204–1213, May 2016.

[13] Australian Energy Market Operator, "Ancillary services," http://www.aemo.com.au/Electricity/Market-Operations/Ancillary-Services, 2011.

[14] ——, "2014 electricity statement of opportunities," https://www.aemo.com.au/-/media/Files/PDF/2014-Electricity-Statement-of-Opportunities.ashx, June 2015.

[15] Australian Essential Services Commission, "Electricity distribution code," May 2012.

[16] Australian Government Department of Industry, Innovation and Science, "Sample household electricity time of use data," https://data.gov.au/dataset/sample-household-electricity-time-of-use-data, July 2014.

[17] T. S. Basso and R. DeBlasio, "IEEE 1547 Series of Standards: Interconnection Issues," *IEEE Transactions on Power Electronics*, vol. 19, no. 5, pp. 1159–1162, 2004.

[18] A. Bergen and D. Hill, "A structure preserving model for power system stability analysis," *IEEE Transactions on Power Apparatus and Systems*, vol. PAS-100, no. 1, pp. 25–35, Jan 1981.

[19] A. Bidram, A. Davoudi, F. Lewis, and Z. Qu, "Secondary control of microgrids based on distributed cooperative control of multi-agent systems," *IET Generation, Transmission Distribution*, vol. 7, no. 8, pp. 822–831, 2013.

[20] U. Borup, F. Blaabjerg, and P. Enjeti, "Sharing of nonlinear load in parallel-connected three-phase converters," *IEEE Transactions on Industry Applications*, vol. 37, no. 6, pp. 1817–1823, Nov 2001.

[21] A. E. Boubakri, "Analysis of the performance of Droop Controlled Inverters in Mini-grids," http://spectrum.library.concordia.ca/977111/1/El-Boubakri_MASc_S2013.pdf, 2013, [Online; last accessed 30-August-2013].

[22] J. Broida and S. Williamson, *A Comprehensive Introduction to Linear Algebra*, ser. Advanced Book Program. Addison-Wesley, 1989. [Online]. Available: https://books.google.com.au/books?id=eyMlAQAAIAAJ

[23] T. Caldognetto and P. Tenti, "Microgrids Operation Based on Master-Slave Cooperative Control," *IEEE Journal of Emerging and Selected Topics in Power Electronics*, vol. 2, no. 4, pp. 1081–1088, Dec 2014.

[24] California Energy Commission, "Integration of Distributed Energy Resources - The CERTS MicroGrid Concept - Consultation Report," http://bnrg.eecs.berkeley.edu/~randy/Courses/CS294.F09/MicroGrid.pdf, 2003, [Online; last accessed 28-January-2016].

[25] Centre for Alternative Technology UK, "Turned On! The UK's First Microgrid Goes Online," http://blog.cat.org.uk/2009/09/02/turned-on-the-uk%E2%80%99s-first-island-micro-grid-goes-online/, 2009, [Online; accessed 18-September-2013].

[26] M. C. Chandorkar, D. M. Divan, and R. Adapa, "Control of parallel connected inverters in standalone ac supply systems," *IEEE Transactions on Industry Applications*, vol. 29, no. 1, pp. 136–143, Jan 1993.

[27] S. X. Chen, H. B. Gooi, and M. Q. Wang, "Sizing of energy storage for microgrids," *IEEE Transactions on Smart Grid*, vol. 3, no. 1, pp. 142–151, March 2012.

[28] S. Chowdhury, S. Chowdhury, C. F. Ten, and P. Crossley, "Islanding protection of distribution systems with distributed generators: A comprehensive survey report," in *IEEE Power and Energy Society General Meeting - Conversion and Delivery of Electrical Energy in the 21st Century, 2008*, 2008, pp. 1–8.

[29] S.-K. Chung, "A phase tracking system for three phase utility interface inverters," *IEEE Transactions on Power Electronics*, vol. 15, no. 3, pp. 431–438, 2000.

[30] M. Ciobotaru, R. Teodorescu, and F. Blaabjerg, "A new single-phase PLL structure based on second order generalized integrator," in *37th IEEE Power Electronics Specialists Conference, 2006. PESC '06*, 2006, pp. 1–6.

[31] E. A. A. Coelho, D. Wu, J. M. Guerrero, J. C. Vasquez, T. Dragicevic, C. Stefanovic, and P. Popovski, "Small-signal analysis of the microgrid secondary control considering a communication time delay," *IEEE Transactions on Industrial Electronics*, vol. 63, no. 10, pp. 6257–6269, Oct 2016.

[32] K. De Brabandere, B. Bolsens, J. Van den Keybus, A. Woyte, J. Driesen, and R. Belmans, "A voltage and frequency droop control method for parallel inverters," *IEEE Transactions on Power Electronics*, vol. 22, no. 4, pp. 1107–1115, 2007.

[33] J. de Hoog, T. Alpcan, M. Brazil, D. Thomas, and I. Mareels, "Optimal Charging of Electric Vehicles Taking Distribution Network Constraints Into Account," *IEEE Transactions on Power Systems*, vol. PP, no. 99, pp. 1–11, 2014.

[34] J. Deign, "Microgrids with 50 percent solar do not need storage," http://www.greentechmedia.com/articles/read/microgrids-with-50-percent-solar-do-not-need-storage?utm_source=feedburner&utm_medium=feed&utm_campaign=Feed%3A+greentechmedia%2Fnews+%28Greentech+Media%3A+News%29, 2015.

[35] S. Dhople, B. Johnson, and A. Hamadeh, "Virtual oscillator control for voltage source inverters," in *51st Annual Allerton Conference on Communication, Control, and Computing (Allerton), 2013*, Oct 2013, pp. 1359–1363.

[36] F. Dorfler and F. Bullo, "Kron Reduction of Graphs With Applications to Electrical Networks," *IEEE Transactions on Circuits and Systems I: Regular Papers*, vol. 60, no. 1, pp. 150–163, Jan 2013.

[37] Emmerson Network Power, "Chloride CP-70i 01 DC/AC inverter datasheet," http://www.emersonnetworkpower.com/documentation/en-us/products/industrialpower/documents/cp-70i/chloride%20cp-70i%2001%20dc-ac%20inverter_dsuk_rev3-062013.pdf, 2014, [Online; last accessed 14-June-2016].

[38] T. Ersal, C. Ahn, I. Hiskens, H. Peng, A. Stefanopoulou, and J. Stein, "On the effect of dc source voltage on inverter-based frequency and voltage regulation in

a military microgrid," in *American Control Conference (ACC), 2012*, June 2012, pp. 2965–2971.

[39] T. Ganu, D. Rahayu, D. Seetharam, R. Kunnath, A. Kumar, V. Arya, S. Husain, and S. Kalyanaraman, "Socketwatch: An autonomous appliance monitoring system," *IEEE International Conference on Pervasive Computing and Communications (PerCom), 2014*, pp. 38–43, March 2014.

[40] A. Ghosh and A. Joshi, "A new approach to load balancing and power factor correction in power distribution system," *IEEE Transactions on Power Delivery*, vol. 15, no. 1, pp. 417–422, 2000.

[41] A. Ghosh, "Power system analysis," Online Lecture - NPTEL, 2008.

[42] M. S. Golsorkhi, M. Savaghebi, D. D. C. Lu, J. M. Guerrero, and J. C. Vasquez, "A gps-based control framework for accurate current sharing and power quality improvement in microgrids," *IEEE Transactions on Power Electronics*, vol. 32, no. 7, pp. 5675–5687, July 2017.

[43] M. S. Golsorkhi, Q. Shafiee, D. Lu, and J. M. Guerrero, "A distributed control framework for integrated photovoltaic-battery based islanded microgrids," *IEEE Transactions on Smart Grid*, vol. PP, no. 99, pp. 1–1, 2016.

[44] Grid Integration Group - Lawrence Berkeley National Laboratory, "Microgrid Research at Berkeley Lab," http://der.lbl.gov/sites/der.lbl.gov/files/microgrid_research_at_lbl_20130426b.pdf, 2013, [Online; accessed 30-September-2013].

[45] J. Guerrero, L. Garcia de Vicuna, J. Matas, M. Castilla, and J. Miret, "A wireless controller to enhance dynamic performance of parallel inverters in distributed generation systems," *IEEE Transactions on Power Electronics*, vol. 19, no. 5, pp. 1205–1213, 2004.

[46] J. Guerrero, J. Matas, L. de Vicua, M. Castilla, and J. Miret, "Wireless-control strategy for parallel operation of distributed-generation inverters," *IEEE Transactions on Industrial Electronics*, vol. 53, no. 5, pp. 1461–1470, 2006.

[47] J. Guerrero, J. Vasquez, J. Matas, M. Castilla, and L. de Vicuna, "Control strategy for flexible microgrid based on parallel line-interactive ups systems," *IEEE Transactions on Industrial Electronics*, vol. 56, no. 3, pp. 726–736, March 2009.

[48] J. Guerrero, J. Vasquez, J. Matas, L. de Vicua, and M. Castilla, "Hierarchical control of droop-controlled ac and dc microgrids 2014;a general approach toward standardization," *IEEE Transactions on Industrial Electronics*, vol. 58, no. 1, pp. 158–172, 2011.

[49] ——, "Hierarchical control of droop-controlled ac and dc microgrids x2014;a general approach toward standardization," *IEEE Transactions on Industrial Electronics*, vol. 58, no. 1, pp. 158–172, Jan 2011.

[50] M. Gulin, "Control of a dc microgrid," https://www.fer.unizg.hr/_download/repository/KDI_Marko_Gulin.pdf, 2014, last accessed: 03-06-2016.

[51] L. Guo, Y. Feng, X. Li, C. Wang, and Y. Li, "Stability analysis of a DC microgrid with master-slave control structure," in *IEEE Energy Conversion Congress and Exposition (ECCE), 2014*, Sept 2014, pp. 5682–5689.

[52] M. Hassan and M. Abido, "Optimal design of microgrids in autonomous and grid-connected modes using particle swarm optimization," *IEEE Transactions on Power Electronics*, vol. 26, no. 3, pp. 755–769, March 2011.

[53] S. Heier, *Grid Integration of Wind Energy: Onshore and Offshore Conversion Systems*. Wiley, March 2014. [Online]. Available: https://books.google.com.au/books?id=d0FsAwAAQBAJ

[54] D. G. Holmes, T. A. Lipo, B. P. McGrath, and W. Y. Kong, "Optimized design of stationary frame three phase ac current regulators," *IEEE Transactions on Power Electronics*, vol. 24, no. 11, pp. 2417–2426, Nov 2009.

[55] D. Holmes and T. Lipo, *Pulse Width Modulation for Power Converters: Principles and Practice*, ser. IEEE Press Series on Power Engineering. John Wiley & Sons, 2003. [Online]. Available: http://books.google.com.au/books?id=8LGi1AjSfpcC

[56] P.-H. Huang, W. Xiao, and M. S. E. Moursi, "A practical load sharing control strategy for DC microgrids and DC supplied houses," in *IECON 2013 - 39th Annual Conference of the IEEE Industrial Electronics Society*, Nov 2013, pp. 7124–7128.

[57] I. Ibraheem, P. Kumar, and D. Kothari, "Recent philosophies of automatic generation control strategies in power systems," *IEEE Transactions on Power Systems*, vol. 20, no. 1, pp. 346–357, 2005.

[58] International Energy Agency, "World Energy Outlook 2013," http://www.worldenergyoutlook.org/, 2013, [Online; last accessed 23-March-2014].

[59] T. Iwade, S. Komiyama, Y. Tanimura, M. Yamanaka, M. Sakane, and K. Hirachi, "A novel small-scale ups using a parallel redundant operation system," in *The 25th International Telecommunications Energy Conference, 2003. INTELEC '03*, Oct 2003, pp. 480–484.

[60] Jacob Ostergaard, John Eli Nielsen, "THE BORNHOLM POWER SYSTEM - An overview ," https://localrenew.soe.ucsc.edu/sites/default/files/denmark_the_bornholm_power_system_an_overview%20%281%29.pdf, 2010, [Online; accessed 21-September-2013].

[61] Jeff St. John , "1.2 Trillion Metric Tons of CO2 in Line Losses ," http://www.greentechmedia.com/articles/read/1.2-Trillion-Metric-Tons-of-CO2-in-Line-Losses, 2012, [Online; last accessed 28-January-2016].

[62] Z. Jiang and R. Dougal, "Hierarchical microgrid paradigm for integration of distributed energy resources," in *IEEE Power and Energy Society (PES) General Meeting (GM) - Conversion and Delivery of Electrical Energy in the 21st Century, 2008*, July 2008, pp. 1–8.

[63] B. Johnson, S. Dhople, J. Cale, A. Hamadeh, and P. Krein, "Oscillator-based inverter control for islanded three-phase microgrids," *IEEE Journal of Photovoltaics*, vol. 4, no. 1, pp. 387–395, Jan 2014.

[64] B. Johnson, S. Dhople, A. Hamadeh, and P. Krein, "Synchronization of nonlinear oscillators in an lti electrical power network," *IEEE Transactions on Circuits and Systems I: Regular Papers*, vol. 61, no. 3, pp. 834–844, March 2014.

[65] B. Johnson, "Control, analysis, and design of distributed inverter systems," Ph.D. dissertation, University of Illinois at Urbana-Champaign, 2013.

[66] S. B. Karmacharya and L. J. de Vries, "Addressing the supply-demand gap in india's electricity market: long and short-term policy options," in *Second International Conference on Infrastructure Systems and Services: Developing 21st Century Infrastructure Networks, (INFRA), 2009*, Dec 2009, pp. 1–6.

[67] F. Katiraei, R. Iravani, N. Hatziargyriou, and A. Dimeas, "Microgrids management," *IEEE Power and Energy Magazine*, vol. 6, no. 3, pp. 54–65, May 2008.

[68] M. Kazmierkowski and L. Malesani, "Current control techniques for three-phase voltage-source pwm converters: a survey," *IEEE Transactions on Industrial Electronics*, vol. 45, no. 5, pp. 691–703, 1998.

[69] H. Khalil, *Nonlinear Systems*. Prentice Hall, 2002. [Online]. Available: http://books.google.com.au/books?id=t_d1QgAACAAJ

[70] H. J. Khasawneh, A. Mondal, M. S. Illindala, B. L. Schenkman, and D. R. Borneo, "Evaluation and sizing of energy storage systems for microgrids," in *IEEE/IAS*

51st Industrial Commercial Power Systems Technical Conference (ICPS) 2015, May 2015, pp. 1–8.

[71] H. Khorramdel, J. Aghaei, B. Khorramdel, and P. Siano, "Optimal battery sizing in microgrids using probabilistic unit commitment," *IEEE Transactions on Industrial Informatics*, vol. 12, no. 2, pp. 834–843, April 2016.

[72] D. S. Kirschen, "Demand-side view of electricity markets," *IEEE Transactions on Power Systems*, vol. 18, no. 2, pp. 520–527, May 2003.

[73] G. Klempner and I. Kerszenbaum, *Operation and maintenance of large turbo generators. [electronic resource].* New York : IEEE Press, c2004., 2004. [Online]. Available: https://ezp.lib.unimelb.edu.au/login?url=https://search-ebscohost-com.ezp.lib.unimelb.edu.au/login.aspx?direct=true&db=cat00006a&AN=melb.b4054412&site=eds-live&scope=site

[74] A. Krishna, C. A. Hans, J. Schiffer, J. Raisch, and T. Kral, "Steady state evaluation of distributed secondary frequency control strategies for microgrids in the presence of clock drifts," in *2017 25th Mediterranean Conference on Control and Automation (MED)*, July 2017, pp. 508–515.

[75] ——, "Steady state evaluation of distributed secondary frequency control strategies for microgrids in the presence of clock drifts," 2017.

[76] B. Kroposki, R. Lasseter, T. Ise, S. Morozumi, S. Papatlianassiou, and N. Hatziargyriou, "Making microgrids work," *Power and Energy Magazine, IEEE*, vol. 6, no. 3, pp. 40–53, 2008.

[77] P. Kundur, N. Balu, and M. Lauby, *Power System Stability and Control*, ser. EPRI Power System Engineering Series. McGraw-Hill, 1994.

[78] H. Laaksonen and K. Kauhaniemi, "Smart protection concept for lv microgrid." *International Review of Electrical Engineering*, vol. 5, no. 2, 2010.

[79] ——, "Synchronized re-connection of island operated lv microgrid back to utility grid," in *IEEE PES Innovative Smart Grid Technologies Conference Europe (ISGT Europe), 2010*, Oct 2010, pp. 1–8.

[80] H. Laaksonen, P. Saari, and R. Komulainen, "Voltage and frequency control of inverter based weak LV network microgrid," in *International Conference on Future Power Systems, 2005*, 2005, pp. 6 pp.–6.

[81] R. H. Lasseter, "Microgrids," in *IEEE Power Engineering Society Winter Meeting, 2002*, vol. 1, 2002, pp. 305–308 vol.1.

[82] R. Lasseter, A. Akhil, C. Marnay, J. Stevens, J. Dagle, R. Guttromson, A. S. Meliopoulous, R. Yinger, and J. Eto, "The CERTS MicroGrid Concept," http://www.energy.ca.gov/research/notices/2002-05-02_WORKSHOP_SUPP.PDF, 2002, [Online; accessed 24-February-2016].

[83] C. Li, S. K. Chaudhary, J. C. Vasquez, and J. M. Guerrero, "Power flow analysis algorithm for islanded lv microgrids including distributed generator units with droop control and virtual impedance loop," in *IEEE Applied Power Electronics Conference and Exposition - APEC 2014*, March 2014, pp. 3181–3185.

[84] N. Li, L. Chen, and S. H. Low, "Optimal demand response based on utility maximization in power networks," in *IEEE Power and Energy Society General Meeting, 2011*, July 2011, pp. 1–8.

[85] Y. W. Li and C.-N. Kao, "An accurate power control strategy for power-electronics-interfaced distributed generation units operating in a low-voltage multibus microgrid," *IEEE Transactions on Power Electronics*, vol. 24, no. 12, pp. 2977–2988, Dec 2009.

[86] P. C. Loh and F. Blaabjerg, "Autonomous control of distributed storages in microgrids," in *IEEE 8th International Conference on Power Electronics and ECCE Asia (ICPE ECCE), 2011*, May 2011, pp. 536–542.

[87] L.-Y. Lu and C.-C. Chu, "Consensus-based droop control synthesis for multiple dics in isolated micro-grids," *IEEE Transactions on Power Systems*, vol. 30, no. 5, pp. 2243–2256, Sept 2015.

[88] X. Lu, K. Sun, J. M. Guerrero, J. C. Vasquez, L. Huang, and R. Teodorescu, "SoC-based droop method for distributed energy storage in DC microgrid applications," in *IEEE International Symposium on Industrial Electronics (ISIE), 2012*, May 2012, pp. 1640–1645.

[89] X. Lu, K. Sun, J. Guerrero, J. Vasquez, L. Huang, and R. Teodorescu, "Soc-based droop method for distributed energy storage in dc microgrid applications," in *IEEE International Symposium on Industrial Electronics (ISIE), 2012*, 2012, pp. 1640–1645.

[90] Magnum Dimensions, "The MSH-RE Series Inverter / Charger," http://www.magnum-dimensions.com/sites/default/files/manuals/spec/MSH-RE_series_datasheet_revB_%2364-0498_web.pdf, 2014, [Online; last accessed 14-June-2016].

[91] R. Majumder, B. Chaudhuri, A. Ghosh, R. Majumder, G. Ledwich, and F. Zare, "Improvement of stability and load sharing in an autonomous microgrid using supplementary droop control loop," in *IEEE Power and Energy Society (PES) General Meeting (GM), 2010*, July 2010, pp. 1–1.

[92] R. Majumder, A. Ghosh, G. Ledwich, and F. Zare, "Angle droop versus frequency droop in a voltage source converter based autonomous microgrid," in *IEEE Power Energy Society (PES) General Meeting (GM), 2009. PES '09*, July 2009, pp. 1–8.

[93] ——, "Operation and control of hybrid microgrid with angle droop controller," in *IEEE Region 10 Conference TENCON 2010*, Nov 2010, pp. 509–515.

[94] R. Majumder, G. Ledwich, A. Ghosh, S. Chakrabarti, and F. Zare, "Droop control of converter-interfaced microsources in rural distributed generation," *IEEE Transactions on Power Delivery*, vol. 25, no. 4, pp. 2768–2778, Oct 2010.

[95] I. Mareels, J. de Hoog, D. Thomas, M. Brazil, T. Alpcan, D. Jayasuriya, V. Muenzel, L. Xia, and R. R. Kolluri, "On making energy demand and network constraints compatible in the last mile of the power grid," *Annual Reviews in Control*, vol. 38, no. 2, pp. 243 – 258, 2014. [Online]. Available: http://www.sciencedirect.com/science/article/pii/S1367578814000418

[96] N. Mohan, T. Undeland, and W. Robbins, *Power Electronics: Converters, Applications, and Design*, ser. Power Electronics: Converters, Applications, and Design. Wiley, 2002, no. v. 2. [Online]. Available: http://books.google.com.au/bookmonashs?id=llK6QgAACAAJ

[97] T. Morstyn, B. Hredzak, V. G. Agelidis, and G. Demetriades, "Cooperative control of DC microgrid storage for energy balancing and equal power sharing," in *Australasian Universities Power Engineering Conference (AUPEC), 2014*, Sept 2014, pp. 1–6.

[98] T. Morstyn, B. Hredzak, and V. Agelidis, "Communication delay robustness for multi-agent state of charge balancing between distributed ac microgrid storage systems," in *IEEE Conference on Control Applications (CCA), 2015*, Sept 2015, pp. 181–186.

[99] ——, "Distributed cooperative control of microgrid storage," *IEEE Transactions on Power Systems*, vol. 30, no. 5, pp. 2780–2789, Sept 2015.

[100] V. Muenzel, I. Mareels, J. de Hoog, A. Vishwanath, S. Kalyanaraman, and A. Gort, "Pv generation and demand mismatch: Evaluating the potential of residential storage," in *IEEE Power Energy Society (PES) Innovative Smart Grid Technologies Conference (ISGT), 2015*, Feb 2015, pp. 1–5.

[101] R. Murray, Z. Li, S. Sastry, and S. Sastry, *A Mathematical Introduction to Robotic Manipulation*. Taylor & Francis, 1994. [Online]. Available: https://books.google.com.au/books?id=D_PqGKRo7oIC

[102] N. Miller, Z. Ye , "Report on Distributed Generation Penetration Study," http://www.nrel.gov/docs/fy03osti/34715.pdf, 2003, [Online; accessed 30-September-2013].

[103] V. Nasirian, Q. Shafiee, J. Guerrero, F. Lewis, and A. Davoudi, "Droop-free distributed control for ac microgrids," *IEEE Transactions on Power Electronics*, vol. 31, no. 2, pp. 1600–1617, Feb 2016.

[104] National Electrical Manufacturers Association, "Powering Microgrids for the 21st-Century Electrical System," "http://www.nema.org/Standards/Pages/Powering-Microgrids-for-the-21st-Century-Electrical-System.aspx, 2016.

[105] E. Nekouei, T. Alpcan, and M. Brandao, "Controlling multiple batteries on a radial line," *2014 Australian Universities Power Engineering Conference AUPEC*, September 2014.

[106] R. Olfati-Saber, J. Fax, and R. Murray, "Consensus and cooperation in networked multi-agent systems," *Proceedings of the IEEE*, vol. 95, no. 1, pp. 215–233, Jan 2007.

[107] N. Orme, "Electric motor theory," "http://neilorme.com/Electric%20Motor%20Theory.shtml, 2012.

[108] P. Palensky and D. Dietrich, "Demand side management: Demand response, intelligent energy systems, and smart loads," *IEEE Transactions on Industrial Informatics*, vol. 7, no. 3, pp. 381–388, Aug 2011.

[109] S. G. Parker, B. P. McGrath, and D. G. Holmes, "Regions of active damping control for LCL filters," in *IEEE Energy Conversion Congress and Exposition (ECCE), 2012*, Sept 2012, pp. 53–60.

[110] P. Pillay and M. Manyage, "Definitions of voltage unbalance," "http://users.encs.concordia.ca/~pillay/16.pdf, 2001.

[111] N. Pogaku, M. Prodanovic, and T. Green, "Modeling, analysis and testing of autonomous operation of an inverter-based microgrid," *IEEE Transactions on Power Electronics*, vol. 22, no. 2, pp. 613–625, 2007.

[112] Power Stream, "Rugged, heavy duty and industrial grade 3-phase pure sine wave DC/AC inverters," http://www.powerstream.com/inverter-3-phase-24vdc-208vac-6000w.htm, 2016, [Online; last accessed 14-June-2016].

[113] Q.Zhong and T.Hornik, *Control of Power Inverters in Renewable Energy and Smart Grid Integration*, ser. Power Electronics: Converters, Applications, and Design. IEEE-Wiley Press, 2013. [Online]. Available: http://au.wiley.com/WileyCDA/WileyTitle/productCd-0470667095.html

[114] Renewable Energy Policy Network for the 21st Century, "Renewable 2013 Global Status Report," http://www.ren21.net/portals/0/documents/resources/gsr/2013/gsr2013_lowres.pdf, 2013, [Online; last accessed 23-March-2014].

[115] M. Ross, R. Hidalgo, C. Abbey, and G. Jos, "Analysis of Energy Storage sizing and technologies," in *IEEE Electric Power and Energy Conference (EPEC), 2010*, Aug 2010, pp. 1–6.

[116] C. Sao and P. Lehn, "Autonomous load sharing of voltage source converters," *IEEE Transactions on Power Delivery*, vol. 20, no. 2, pp. 1009–1016, April 2005.

[117] M. Savaghebi, A. Jalilian, J. Vasquez, and J. Guerrero, "Autonomous voltage unbalance compensation in an islanded droop-controlled microgrid," *IEEE Transactions on Industrial Electronics*, vol. 60, no. 4, pp. 1390–1402, 2013.

[118] J. Schiffer, A. Anta, T. D. Trung, J. Raisch, and T. Sezi, "On power sharing and stability in autonomous inverter-based microgrids," in *IEEE 51st Annual Conference on Decision and Control (CDC), 2012*, Dec 2012, pp. 1105–1110.

[119] J. Schiffer, D. Goldin, J. Raisch, and T. Sezi, "Synchronization of droop-controlled microgrids with distributed rotational and electronic generation," in *52nd IEEE Conference on Decision and Control*, Dec 2013, pp. 2334–2339.

[120] J. Schiffer, R. Ortega, C. A. Hans, and J. Raisch, "Droop-controlled inverter-based microgrids are robust to clock drifts," in *American Control Conference (ACC), 2015*, July 2015, pp. 2341–2346.

[121] J. Schiffer, T. Seel, J. Raisch, and T. Sezi, "A consensus-based distributed voltage control for reactive power sharing in microgrids," in *European Control Conference (ECC), 2014*, June 2014, pp. 1299–1305.

[122] J. Schiffer, R. Ortega, A. Astolfi, J. Raisch, and T. Sezi, "Conditions for stability of droop-controlled inverter-based microgrids," *Automatica*, vol. 50, no. 10, pp. 2457 – 2469, 2014. [Online]. Available: http://www.sciencedirect.com/science/article/pii/S0005109814003100

[123] Schneider Electric, "Conext XW inverter/charger product manual," http://solar.schneider-electric.com/wp-content/uploads/2014/08/Conext-XW-Owners-Guide-NA-975-0240-01-01_Rev-E_ENG.pdf, 2014, [Online; accessed 8-November-2014].

[124] Q. Shafiee, T. Dragicevic, F. Andrade, J. C. Vasquez, and J. M. Guerrero, "Distributed consensus-based control of multiple dc-microgrids clusters," in *IECON 2014 - 40th Annual Conference of the IEEE Industrial Electronics Society*, Oct 2014, pp. 2056–2062.

[125] Q. Shafiee, J. M. Guerrero, and J. C. Vasquez, "Distributed secondary control for islanded microgrids : A novel approach," *IEEE Transactions on Power Electronics*, vol. 29, no. 2, pp. 1018–1031, Feb 2014.

[126] Q. Shafiee, J. Vasquez, and J. Guerrero, "Distributed secondary control for islanded microgrids - a networked control systems approach," in *38th Annual Conference on IEEE Industrial Electronics Society IECON, 2012*, 2012, pp. 5637–5642.

[127] V. Shah and J. Booream-Phelps, "Deutsche Bank Markets Research - Solar," https://www.db.com/cr/en/docs/solar_report_full_length.pdf, 2015, [Online; last accessed 28-January-2016].

[128] B. Shoeiby, R. Davoodnezhad, D. Holmes, and B. McGrath, "A new current control droop strategy for VSI-based islanded microgrids," in *International Power Electronics Conference (IPEC-Hiroshima 2014 - ECCE-ASIA), 2014*, May 2014, pp. 1482–1489.

[129] ——, "A resonant current regulator based microgrid control strategy with smooth transition between islanded and grid-connected modes," in *IEEE 5th International Symposium on Power Electronics for Distributed Generation Systems (PEDG), 2014*, June 2014, pp. 1–8.

[130] ——, "Voltage-frequency control of an islanded microgrid using the intrinsic droop characteristics of resonant current regulators," in *IEEE Energy Conversion Congress and Exposition (ECCE), 2014*, Sept 2014, pp. 68–75.

[131] B. Shoeiby, D. Holmes, B. P. McGrath, and R. Davoodnezhad, "Dynamics of droop-controlled microgrids with unequal droop response times," in *Australasian Universities Power Engineering Conference (AUPEC), 2013*. IEEE, 2013, pp. 1–6.

[132] J. R. Silvester, "Determinants of Block Matrices," http://www.ee.iisc.ac.in/new/people/faculty/prasantg/downloads/blocks.pdf, 2014, [Online; accessed 30-June-2016].

[133] J. W. Simpson-Porco, Q. Shafiee, F. Drfler, J. C. Vasquez, J. M. Guerrero, and F. Bullo, "Secondary frequency and voltage control of islanded microgrids via distributed averaging," *IEEE Transactions on Industrial Electronics*, vol. 62, no. 11, pp. 7025–7038, Nov 2015.

[134] ——, "Secondary frequency and voltage control of islanded microgrids via distributed averaging," *IEEE Transactions on Industrial Electronics*, vol. 62, no. 11, pp. 7025–7038, Nov 2015.

[135] J. W. Simpson-Porco, F. Dörfler, and F. Bullo, "Droop-controlled inverters are kuramoto oscillators," *IFAC Proceedings Volumes*, vol. 45, no. 26, pp. 264–269, 2012.

[136] J. W. Simpson-Porco, F. Drfler, and F. Bullo, "Synchronization and power sharing for droop-controlled inverters in islanded microgrids," *Automatica*, vol. 49, no. 9, pp. 2603 – 2611, 2013. [Online]. Available: http://www.sciencedirect.com/science/article/pii/S0005109813002884"

[137] J. Simpson-Porco, F. Dorfler, F. Bullo, Q. Shafiee, and J. Guerrero, "Stability, power sharing, amp; distributed secondary control in droop-controlled microgrids," in *IEEE International Conference on Smart Grid Communications (SmartGridComm), 2013*, Oct 2013, pp. 672–677.

[138] M. Sinha, F. Dorfler, B. Johnson, and S. Dhople, "Virtual oscillator control subsumes droop control," in *American Control Conference (ACC), 2015*, July 2015, pp. 2353–2358.

[139] SolarEdge Technologies Inc., "Communication solaredge inverters," http://www.solaredge.com/products/communication, 2016, accessed: 2016-09-26.

[140] I. Standards, "IEEE Series of Standards for Interconnection of distributed sources into the Electrical Power System ," *IEEE Standards*, 2011.

[141] X. Tan, Q. Li, and H. Wang, "Advances and trends of energy storage technology in microgrid." *International Journal of Electrical Power and Energy SystemsNTERNATIONAL JOURNAL OF ELECTRICAL POWER AND ENERGY SYSTEMS*, vol. 44, no. 1, pp. 179 – 191, 2013. [Online]. Available: https://ezp.lib.unimelb.edu.au/login?url=https://search.ebscohost.com/login.aspx?direct=true&db=edswsc&AN=000311864800020&site=eds-live

[142] R. Teodorescu, F. Blaabjerg, M. Liserre, and P. Loh, "Proportional-resonant controllers and filters for grid-connected voltage-source converters," *IEE Proceedings Electric Power Applications*, vol. 153, no. 5, pp. 750–762, 2006.

[143] C. C. Thompson, K. Oikonomou, A. H. Etemadi, and V. J. Sorger, "Optimization of Data Center Battery Storage Investments for Microgrid Cost Savings, Emissions Reduction, and Reliability Enhancement," *IEEE Transactions on Industry Applications*, vol. PP, no. 99, pp. 1–1, 2016.

[144] A. Tuladhar, H. Jin, T. Unger, and K. Mauch, "Control of parallel inverters in distributed ac power systems with consideration of line impedance effect," *IEEE Transactions on Industry Applications*, vol. 36, no. 1, pp. 131–138, Jan 2000.

[145] T. Vandoorn, B. Meersman, J. D. M. De Kooning, and L. Vandevelde, "Analogy between conventional grid control and islanded microgrid control based on a global dc-link voltage droop," *IEEE Transactions on Power Delivery*, vol. 27, no. 3, pp. 1405–1414, July 2012.

[146] T. Vandoorn, B. Meersman, J. De Kooning, and L. Vandevelde, "Transition from islanded to grid-connected mode of microgrids with voltage-based droop control," *IEEE Transactions on Power Systems*, vol. 28, no. 3, pp. 2545–2553, Aug 2013.

[147] T. Vandoorn, B. Meersman, L. Degroote, B. Renders, and L. Vandevelde, "A control strategy for islanded microgrids with dc-link voltage control," *IEEE Transactions on Power Delivery*, vol. 26, no. 2, pp. 703–713, 2011.

[148] T. Vandoorn, B. Renders, B. Meersman, L. Degroote, and L. Vandevelde, "Reactive power sharing in an islanded microgrid," in *45th International Universities Power Engineering Conference (UPEC), 2010*, Aug 2010, pp. 1–6.

[149] J. Vasquez, J. Guerrero, A. Luna, P. Rodriguez, and R. Teodorescu, "Adaptive droop control applied to voltage-source inverters operating in grid-connected and islanded modes," *IEEE Transactions on Industrial Electronics*, vol. 56, no. 10, pp. 4088–4096, Oct 2009.

[150] J. Vasquez, J. Guerrero, M. Savaghebi, J. Eloy-Garcia, and R. Teodorescu, "Modeling, analysis, and design of stationary-reference-frame droop-controlled parallel three-phase voltage source inverters," *IEEE Transactions on Industrial Electronics*, vol. 60, no. 4, pp. 1271–1280, 2013.

[151] V. Verma and G. Talpur, "Decentralized master-slave operation of microgrid using current controlled distributed generation sources," in *IEEE International Conference on Power Electronics, Drives and Energy Systems (PEDES), 2012*, Dec 2012, pp. 1–6.

[152] Virginia Polytechnic Institute and State University, "Distributed generation," http://www.dg.history.vt.edu/ch1/introduction.html, 2007.

[153] C. Wang, X. Li, L. Guo, and Y. Li, "A seamless operation mode transition control strategy for a microgrid based on master-slave control," *Science China Technological Sciences*, vol. 55, no. 6, pp. 1644–1654, 2012. [Online]. Available: http://dx.doi.org/10.1007/s11431-012-4811-z

[154] B. M. Weedy, B. J. Cory, N. Jenkins, J. Ekanayake, and G. Strbac, *Electric Power Systems*. John Wiley & Sons, 2012.

[155] G. Weiss, Q.-C. Zhong, T. Green, and J. Liang, "H infin; repetitive control of dc-ac converters in microgrids," *IEEE Transactions on Power Electronics*, vol. 19, no. 1, pp. 219–230, Jan 2004.

[156] J. Xiao, L. Bai, F. Li, H. Liang, and C. Wang, "Sizing of Energy Storage and Diesel Generators in an Isolated Microgrid Using Discrete Fourier Transform (DFT)," *IEEE Transactions on Sustainable Energy*, vol. 5, no. 3, pp. 907–916, July 2014.

[157] Q. Yaser, T. Kerdphol, and Y. Mitani, "Different optimization schemes for community based energy storage systems," in *4th International Conference on Electric Power and Energy Conversion Systems (EPECS) 2015*, Nov 2015, pp. 1–5.

[158] A. Yazdani and R. Iravani, *Voltage-Sourced Converters in Power Systems*. John Wiley & Sons, 2010.

[159] Yueqing Sandi Electric Co., Ltd, "Solar Sine Wave Inverter," https://www.evworks.com.au/assets/files/Manual%20of%20SDP-10KW%20inverter.pdf, 2008, [Online; last accessed 14-June-2016].

[160] N. Zareen and Mustafa, "Worldwide technological revolutions and its challenges under smart grid paradigm: A comprehensive study," *International Journal of Scientific & Engineering Research*, vol. 3, no. 11, pp. 1–6, 2012.

[161] Q. Zhong and Y. Zeng, "Control of inverters via a virtual capacitor to achieve capacitive output impedance," *IEEE Transactions on Power Electronics*, vol. PP, no. 99, pp. 1–1, 2013.

[162] Q.-C. Zhong, "Robust droop controller for accurate proportional load sharing among inverters operated in parallel," *IEEE Transactions on Industrial Electronics*, vol. 60, no. 4, pp. 1281–1290, 2013.

[163] Q.-C. Zhong, P.-L. Nguyen, Z. Ma, and W. Sheng, "Self-synchronized synchronverters: Inverters without a dedicated synchronization unit," *IEEE Transactions on Power Electronics*, vol. 29, no. 2, pp. 617–630, 2014.

[164] Q.-C. Zhong and G. Weiss, "Synchronverters: Inverters that mimic synchronous generators," *IEEE Transactions on Industrial Electronics*, vol. 58, no. 4, pp. 1259–1267, April 2011.

[165] Q.-C. Zhong and Y. Zeng, "Can the output impedance of an inverter be designed capacitive?" in *37th Annual Conference on IEEE Industrial Electronics Society IECON, 2011*, Nov 2011, pp. 1220–1225.

[166] Y. Zhu, F. Zhuo, and L. Xiong, "Communication platform for energy management system in a master-slave control structure microgrid," in *7th International Power*

Electronics and Motion Control Conference (IPEMC), 2012, vol. 1, June 2012, pp. 141–145.

[167] D. Zmood and D. Holmes, "Stationary frame current regulation of pwm inverters with zero steady-state error," *IEEE Transactions on Power Electronics*, vol. 18, no. 3, pp. 814–822, 2003.

University Library

A gateway to Melbourne's research publications

Minerva Access is the Institutional Repository of The University of Melbourne

Author/s:
Kolluri, Ramachandra Rao

Title:
Operating converter interfaced microgrids

Date:
2016

Persistent Link:
http://hdl.handle.net/11343/191670

File Description:
Thesis

Terms and Conditions:
Terms and Conditions: Copyright in works deposited in Minerva Access is retained by the copyright owner. The work may not be altered without permission from the copyright owner. Readers may only download, print and save electronic copies of whole works for their own personal non-commercial use. Any use that exceeds these limits requires permission from the copyright owner. Attribution is essential when quoting or paraphrasing from these works.